Cavity-Enhanced Absorption Spectroscopy with a Deep UV-LED

Danica Glenda Pinto

Submitted for the degree of Doctor of Philosophy

Heriot-Watt University

School of Engineering and Physical Sciences

August 2019

ABSTRACT

The motivation for this project work was to build a portable analyser based on a UV-LED to carry out in situ measurements of trace gas species under ambient conditions applied to atmospheric monitoring and breath analysis. Acetone has gained vital importance as a volatile organic compound (VOC) which is found as a pollutant in the atmosphere. Acetone also serves as a biomarker for metabolic processes particularly in people on a ketogenic diet or patients suffering from diabetic ketoacidosis (DKA), a life-threatening condition that can be experienced by Type 1 Diabetic patients. The project work mainly consisted of two parts: design of a portable set-up and as a proof of principle that a UV-LED based acetone detector is feasible instead of the most commonly used laser-based detector. Acetone absorption measurements were carried out in nitrogen background using a 300 nm LED employing the technique of Incoherent Broadband Cavity-Enhanced Absorption Spectroscopy (IBBCEAS).

The design of the portable set-up is based on a cage-system to achieve portability, robustness, mechanical stability, insensitivity to temperature and pressure variations, and cost-effectiveness. The designed portable set-up has potential applications as a detector providing in situ real-time detection of trace gas species in atmospheric chemistry and in medical diagnostics as a breath acetone analyser.

An incoherent light source such as an LED requires a different approach to light collimation and guiding compared to a laser. In the UV range this poses additional challenges due to a lack of off-the-shelf optical components for this purpose. In this project, a stable optical cavity was successfully set-up to carry out acetone absorption measurements in nitrogen background using CEAS. A noise-equivalent absorption coefficient of $4.1 \pm 0.3 \times 10^{-6}$ $cm^{-1}Hz^{-1/2}$ (corresponding to ~2 ppmv of acetone) was achieved with the CEAS set-up.

ACKNOWLEDGEMENTS

Pursuing this PhD has been a truly life-changing experience for me and this would not have been possible without the guidance and support from many people. I would like to thank Heriot-Watt University for granting me the James Watt Scholarship to pursue this PhD. I am sincerely grateful to my supervisor Dr Hendrik Nahler for offering me this opportunity. I would like to thank all my colleagues from the big laser laboratory, especially Tom, Dave, Paul and Aisling for the support and help I received. I am grateful to my uncles, aunts, cousins and friends who have backed me in one way or the other through their moral support, especially Jasleen and Sid. I would like to specially thank my friend Chiara for being there for me morally and being the best lab mate one could ever ask for. I would like to say a heartfelt thank you to my parents and my in-laws for believing in me and encouraging me to follow my dreams. I would like to thank my brother Graiden for being my go-to person for technical help. Nobody has been more important to me in the pursuit of this PhD than my dear husband Dee, thank you for always being by my side during my ups and downs all this time.

Research Thesis Submission

Please note this form should be bound into the submitted thesis.

Name:	Danica Glenda Pinto		
School:	School of Engineering and Physical Sciences - ICS		
Version: *(i.e. First, Resubmission, Final)*	Final	Degree Sought:	PhD

Declaration

In accordance with the appropriate regulations I hereby submit my thesis and I declare that:

1. The thesis embodies the results of my own work and has been composed by myself
2. Where appropriate, I have made acknowledgement of the work of others
3. The thesis is the correct version for submission and is the same version as any electronic versions submitted*.
4. My thesis for the award referred to, deposited in the Heriot-Watt University Library, should be made available for loan or photocopying and be available via the Institutional Repository, subject to such conditions as the Librarian may require
5. I understand that as a student of the University I am required to abide by the Regulations of the University and to conform to its discipline.
6. I confirm that the thesis has been verified against plagiarism via an approved plagiarism detection application e.g. Turnitin.

ONLY for submissions including published works

Please note you are only required to complete the Inclusion of Published Works Form (page 2) if your thesis contains published works)

7. Where the thesis contains published outputs under Regulation 6 (9.1.2) or Regulation 43 (9) these are accompanied by a critical review which accurately describes my contribution to the research and, for multi-author outputs, a signed declaration indicating the contribution of each author (complete)
8. Inclusion of published outputs under Regulation 6 (9.1.2) or Regulation 43 (9) shall not constitute plagiarism.

* *Please note that it is the responsibility of the candidate to ensure that the correct version of the thesis is submitted.*

Signature of Candidate:		Date:	20/01/2020

Submission

Submitted By *(name in capitals):*	
Signature of Individual Submitting:	
Date Submitted:	

For Completion in the Student Service Centre (SSC)

Limited Access	Requested	Yes		No		Approved	Yes		No	
E-thesis Submitted (mandatory for final theses)										
Received in the SSC by *(name in capitals):*						Date:				

Inclusion of Published Works

Please note you are only required to complete the Inclusion of Published Works Form if your thesis contains published works under Regulation 6 (9.1.2)

Declaration

This thesis contains one or more multi-author published works. In accordance with Regulation 6 (9.1.2) I hereby declare that the contributions of each author to these publications is as follows:

Citation details	N/A
Author 1	
Author 2	
Signature:	
Date:	

Citation details	
Author 1	
Author 2	
Signature:	
Date:	

Citation details	
Author 1	
Author 2	
Signature:	
Date:	

TABLE OF CONTENTS

Chapter 1 - Introduction

1.1 Aim

The main aim of this project is to establish as a proof of principle that a stable optical cavity for Cavity-Enhanced Absorption Spectroscopy (CEAS) measurements can be set-up employing a 300 nm light emitting diode (LED), a broadband light source instead of the most commonly used monochromatic light source such as a laser. In addition to establishing the proof of principle, the project also aims to design a portable set-up to carry out in situ measurements of trace gas species in the atmosphere using their electronic transitions and for breath analysis, with acetone as a model system.

1.2 Acetone Photoexcitation

The importance of acetone (the molecule of interest) as a volatile organic compound (VOC) in the atmosphere and its role as a biomarker in exhaled human breath especially in the case of detecting diabetic ketoacidosis (DKA), a severe condition experienced by Type 1 diabetic patients is discussed in the following sections of this chapter. To better understand the photochemistry of the acetone molecule, this chapter discusses the photoexcitation and consequently the fates of the electronically excited acetone molecule.

Acetone (also known as 2-propanone**,** dimethyl ketone, propan-2-one and beta-ketopropane), with its chemical formula $(CH_3)_2CO$, is the simplest and smallest ketone. It is a fruity smelling, volatile, colourless and flammable liquid at normal conditions. Acetone is readily miscible in water, ether, and ethanol and it also serves as an important solvent. The structure of acetone is shown in Figure 1. One of the potential applications of the portable set-up is as an acetone breath analyser and as a set-up to carry out field measurements for the detection of atmospheric trace gas species. This has provided the motivation for carrying out acetone absorption measurements in this project.

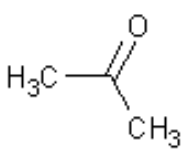

Figure 1 Structure of an acetone molecule.

The energies required to bring about electronic transitions in a molecule are of the order of a few electronvolts (eV) and thus the photons emitted or absorbed during such transitions correspond to the UV and visible regions of the electromagnetic spectrum [1]. The absorption of UV/Visible light by an organic molecule results in the formation of an electronically excited molecule which involves the excitation of an electron from its initial Highest Occupied Molecular Orbital (HOMO) to its Lowest Unoccupied Molecular Orbital (LUMO) [2] as shown in Figure 2.

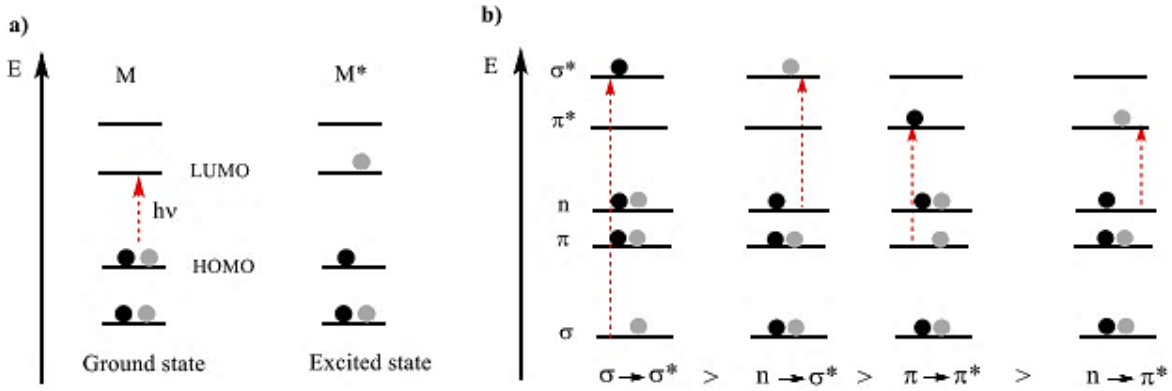

Figure 2 (a) An absorption transition occurring between HOMO and LUMO levels in an organic molecule. (b) Energy level diagram displaying the various types of electronic transitions that can occur in an organic molecule starting from the more energetic $\sigma \rightarrow \sigma^*$ transition to the less energetic $n \rightarrow \pi^*$ transition [3]. σ and π are bonding molecular orbitals, n is the non-bonding molecular orbital containing the lone-pair of electrons and σ^* and π^* are anti-bonding molecular orbitals of the molecule.

The acetone molecule is a carbonyl compound i.e., with the functional group C=O. This segment of the molecule that is responsible for the electronic transition is called a chromophore. In acetone the HOMO-LUMO transition corresponds to the $n \rightarrow \pi^*$ transition (shown in Figure 3) of the chromophore carbonyl group whose photo-reactivity has been known since the early 1900s [4, 5].

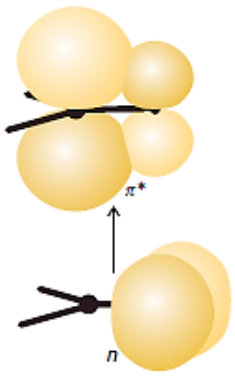

Figure 3 In carbonyl compounds such as acetone, the carbonyl (C=O) group acts as a chromophore mainly due to the excitation of an electron from the non-bonding (*n*) oxygen lone-pair to an antibonding π^* orbital [1].

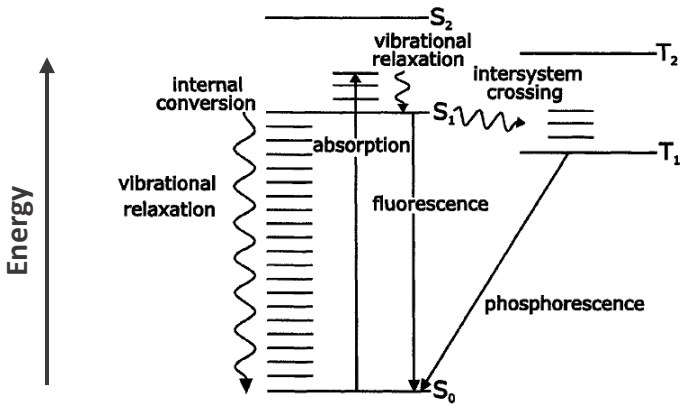

Figure 4 Jablonski diagram showing various photo-processes: radiative (fluorescence and phosphorescence) and non-radiative (vibrational relaxation, internal conversion, intersystem crossing and bimolecular quenching) pathways that can occur in an acetone molecule [6]. Photodissociation is not shown.

An acetone molecule in its ground electronic state (S_0) can absorb UV radiation to undergo an electronic transition to its first excited electronic state (S_1). The electronic absorption process follows selection rules [1]. The excited molecule can undergo several radiative and non-radiative processes to remove excess energy and return to its ground state. These processes except photodissociation are summarised in the Jablonski diagram shown in Figure 4. The electronic transitions in a molecule occur on a timescale of ~10^{-15}s, which is accompanied with rapid re-distribution of electron density of the molecule. According to the Franck-Condon principle, an electronic transition is much faster than the nuclei can respond to

the changed electron distribution, because the nuclei are so much more massive than the electrons. In accordance to this principle, the nuclear framework of the molecule remains constant during the excitation process and the most probable electronic transition takes place vertically upwards (indicated by vertical arrows in Figure 5) between the two electronic states. Therefore, the molecule undergoes excitation to a vibrational level of the excited state whose wavefunction has maximum overlap with that of the vibrational level of its ground electronic state. Transitions to other vibrational levels of the excited state also take place but with lower intensity and this results in a broad absorption spectrum of the molecule [1].

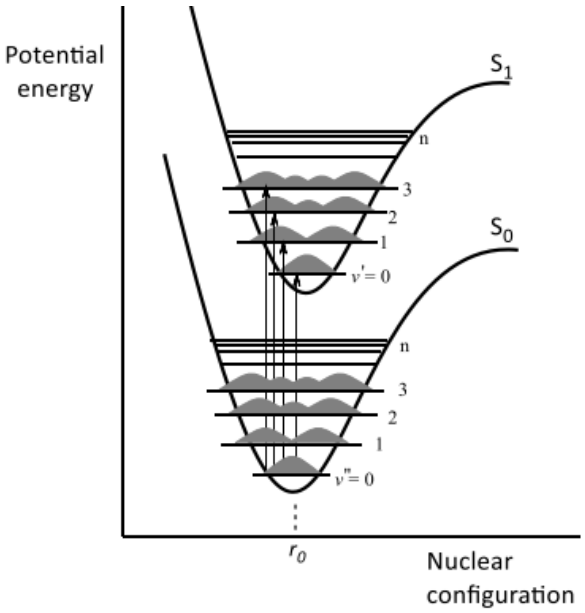

Figure 5 Potential energy surface diagram for the ground (S_0) and the first excited (S_1) electronic state of a molecule. The vibrational levels are shown as squares of the wavefunctions (harmonic) for the two electronic states. The vertical arrows indicate transitions in accordance to the Franck-Condon principle [3].

1.2.1 Acetone Absorption Cross-section

In this project, absorption measurements of acetone are carried out in the wavelength range 292 – 302 nm. The absorption process in acetone can be understood by considering its molecular orbitals as shown in Figure 6. This figure illustrates that transitions from the non-bonding molecular orbital (n) to the empty π^* orbital require less energy than the transition from its bonding π orbital. Thus, in acetone the carbonyl group (C=O) is responsible for the absorbance of UV radiation occurring around 300 nm which corresponds to the transitions between non-bonding orbitals (n) to anti-bonding orbitals (π^*). The transition $n \rightarrow \pi^*$

corresponds to an absorption maximum at ~275 nm while the transition $\pi \rightarrow \pi^*$ corresponds to an absorption maximum at about 190 nm [7]. In carbonyl groups, the $\pi \rightarrow \pi^*$ transition is stronger than the $n \rightarrow \pi^*$ and this can be explained considering the molecular orbitals of the carbonyl group. This difference in the intensity of absorption is due to their orbital overlap. The Figure 3 and Figure 6, illustrate that the non-bonding molecular orbital is at right angles to the π^* (anti-bonding) molecular orbital.

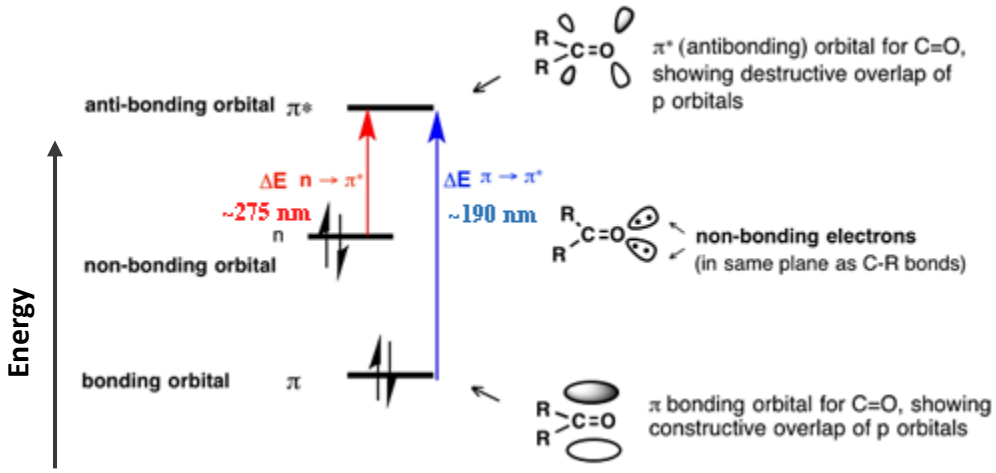

Figure 6 Simplified molecular orbital diagram of acetone [7]. The transitions $n \rightarrow \pi^*$ and $\pi \rightarrow \pi^*$ that occur upon interaction with light of wavelengths ~275 nm and ~190 nm respectively are indicated. The orbitals are also displayed to indicate that the non-bonding orbital (n) is oriented at right angles to that of the bonding (π) and anti-bonding (π^*) molecular orbitals.

According to the spin selection rule that governs electronic transitions in a molecule, a transition is spin-allowed if there is no change in the spin of the electron during the transition ($\Delta S = 0$). The poor spatial overlap of the n and π^* orbitals of the carbonyl group result in a weak $n \rightarrow \pi^*$ transition ($S_0 \rightarrow S_1$, spin-allowed), that is sometimes called 'orbital-forbidden' transition. The intensity of an electronic transition is proportional to the square of the transition dipole moment and for an allowed transition, the transition dipole moment is non-zero [1]. If the wavefunctions of the ground and excited states have different symmetry, the resulting integral determining the transition moment is zero and the corresponding transition becomes 'symmetry forbidden'. This selection rule is applicable to the $S_0 \rightarrow S_1$ transition in ketones. A partial violation of the Born-Oppenheimer approximation brings about the absorption of light by these molecules in contrast to the selection rules. The intra-molecular vibrations couple with the electronic system that consequently distort the electronic wavefunctions, thus,

breaking the perfect symmetry and leading to non-zero contributions to the integral. These resulting transitions are called 'vibrationally allowed' transitions [8]. Therefore, resulting in a less intense $n \rightarrow \pi^*$ transition. In this project, the light source is centred around 300 nm, and the transition involved in acetone is a $n \rightarrow \pi^*$ transition. Acetone absorption cross-sections in the wavelength range 215 – 349 nm are shown in Figure 7.

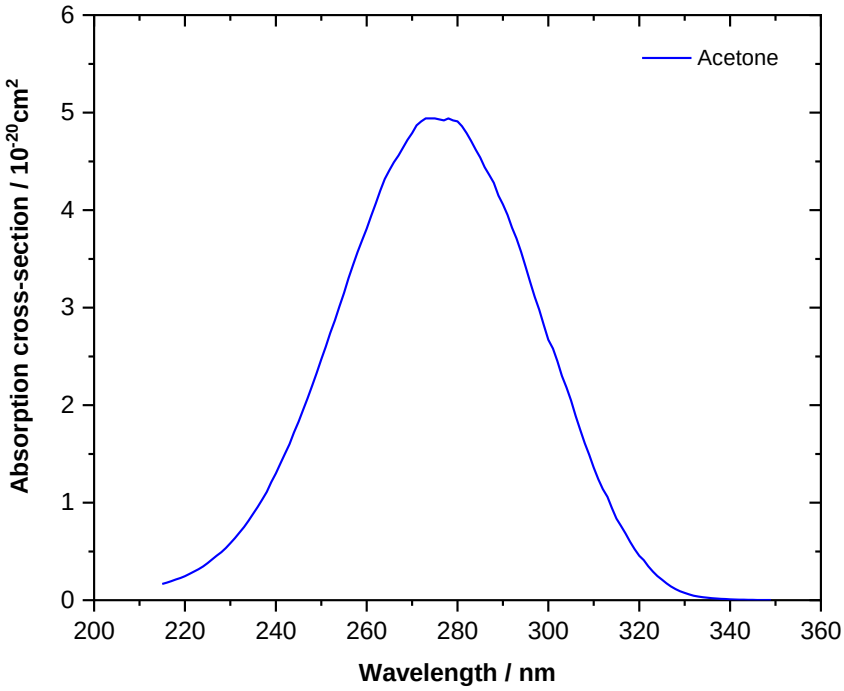

Figure 7 Acetone absorption cross-section in the wavelength range 215 – 349 nm measured at 298 K (JPL 2010 recommendation) [9].

1.3 Fates of Electronically Excited Acetone Molecule

The de-excitation pathways of acetone are summarised in this section. An electronically excited acetone molecule can undergo de-excitation either radiatively or non-radiatively or via photodissociation. The radiative processes can be classified into fluorescence and phosphorescence depending on the spin multiplicity of the excited state. Fluorescence involves the spontaneous emission of a photon as it decays from an excited state to the ground state with the same spin multiplicity ($S_1 \rightarrow S_0$). As the spin multiplicity is unchanged, this transition is spin-allowed and occurs on a timescale of ~10^{-9}s. Similar to the absorption process, fluorescence also obeys the Franck-Condon principle, thus the resulting fluorescence spectrum will be a resembling mirror image of the absorption spectrum of the molecule [1]. The process of phosphorescence on the other hand involves transition from the triplet excited

state to the singlet ground state ($T_1 \rightarrow S_0$). This transition is spin-forbidden in accordance to the spin selection rules. However, in heavy molecules this transition is not totally forbidden due to spin-orbit coupling which is also responsible for the transition from the first excited singlet electronic state to the first triplet electronic state of the molecule (via intersystem crossing). Therefore, this transition occurs on a timescale of the order of $10^{-4} – 10^{-1}$s [10]. In the case of acetone, collisional quenching of phosphorescence resulting in non-radiative decay to the S_0 state can occur due to collisions with molecular oxygen [8].

The non-radiative decay pathways in acetone molecule include vibrational relaxation, internal conversion and intersystem crossing. Vibrational relaxation involves the transition from a higher to a lower vibrational level of the same electronic state of the molecule with the emission of vibrational energy. When radiationless de-excitation occurs between two electronic states of the same multiplicity it is termed as an internal conversion. This process occurs on a timescale of $10^{-14} – 10^{-11}$s [10]. In the case of acetone, it has been shown that fluorescence emission has higher probability than internal conversion [8]. When a transition occurs between two isoenergetic vibrational levels of the excited electronic states of different spin multiplicities ($S_1 \rightarrow T_1$), it is termed as an intersystem crossing. As this is a spin-forbidden transition that is weakly allowed due to spin-orbit coupling, it occurs on a timescale of $10^{-8} – 10^{-3}$s [10].

Another decay pathway seen in acetone is photodissociation, which involves the scission of the C-C bond with the absorption of UV-radiation [11]. The photodissociation in acetone occurs when the molecule is excited to the first electronically excited state overcoming the dissociation barrier located either on the first excited singlet or triplet excited state of the molecule [12]. Acetyl and methyl radicals are produced as a result of acetone photodissociation [11, 13] .

1.4 Nitrogen Rayleigh Scattering

The IBBCEAS technique employed in this project involves the determination of effective mirror reflectivities by Rayleigh scattering measurements of nitrogen as discussed in section 2.4. When light is incident on a molecule, it can either absorb the light and undergo any of the de-excitation pathways as shown in Figure 4 or it can scatter the light. One such scattering phenomenon is Rayleigh scattering process which is named after the British physicist Lord Rayleigh (John W Strutt). This process is described as the elastic scattering of

light by particles that are much smaller than the wavelength of the incident light [14, 15]. In the case of a spherical particle, the Rayleigh scattering cross-section σ_R is proportional to $1/\lambda^4$. Considering the components of the medium as spherical particles that are smaller than the wavelength of incident light, Rayleigh proposed the formula as follows [15],

$$\sigma_R = \frac{32\,\pi^3}{3\lambda^4 N^2}(n(\lambda)-1)^2 \qquad (1)$$

where σ_R is dependent on the wavelength λ of incident radiation, the molecular density (N) and n the refractive index of the medium. Considering the correction factors for the local field of the particles (which arises due to the localised field acting in the vicinity of a particle essentially not being the same as the macroscopic field) and the King correction factor for the non-spherical geometry of the particles, σ_R in Equation 1 is written as:

$$\sigma_R = \frac{24\,\pi^3}{\lambda^4 N^2}\left(\frac{n(\lambda)^2-1}{n(\lambda)^2+2}\right)^2 F_k(\lambda) \qquad (2)$$

which includes the local field correction factor $(3/(n^2+2))$ that mostly holds true for gases and $F_k(\lambda)$ the dimensionless King correction factor [16 – 18]. It was observed that σ_R of non-spherical gas molecules do not precisely obey the $1/\lambda^4$ relationship as the correction factors are also dependent on λ and hence σ_R was better described as being dependent on $1/\lambda^{4+\varepsilon}$, where ε is a dimensionless parameter [19].

In this project, nitrogen Rayleigh scattering is used to determine the effective reflectivity of the optical cavity for absorption measurements of acetone using the CEAS technique. The Rayleigh scattering cross-sections σ_R in the wavelength range 292 – 302 nm for nitrogen was determined using the formula [19]:

$$\sigma_R = \frac{\sigma}{\lambda^{4+\varepsilon}} \qquad (3)$$

where, the parameter $\varepsilon = 0.534 \pm 0.003$ is dimensionless and the parameter $\sigma = 18.0 \pm 0.6 \times 10^{-47}$ cm^2 [20].

1.5 Acetone in the Atmosphere

Acetone is an important atmospheric trace gas that is omnipresent in the troposphere (the lower most zone of the Earth's atmosphere extending up to about 10 km from the Earth's surface) and is one of the abundant oxygenated volatile organic compounds (OVOCs) at concentrations ranging 0.2 – 3 ppbv (parts per billion by volume) [21– 23].

The main sources of acetone include direct anthropogenic and biogenic emissions (produced from terrestrial vegetation, biomass burning and grasslands). Minor sources mainly comprise of secondary production arising from atmospheric oxidation of biogenic precursors (mainly isoprene) and low-number anthropogenic isoalkanes (C_3 to C_5) mostly coming from automobile fuel evaporation and natural gas exploitation [23].

In addition to dry deposition to ocean and land surfaces the major sinks for acetone in the atmosphere are reactions with hydroxyl (OH) radicals and dissociation in the presence of UV-light in the atmosphere [24, 25]. Photodissociation of acetone results in the production of hydrogen oxide HO_x (= OH, HO_2) radicals along with relatively stable trace gases such as peroxyacetylnitrate (PAN), acetic acid and peracetic acid in the atmosphere [26]. The formation of PAN involves removal of nitrogen oxides (NO_x = NO, NO_2) from the atmosphere. HO_x and NO_x have a vital role in atmospheric trace gas and aerosol processes as well as in ozone formation. Thus, acetone has a potential indirect impact on trace gas species mostly in the upper tropospheric region where other HO_x sources are relatively small and where PAN is thermally stable [22]. These recent discoveries of atmospheric acetone have encouraged further investigations into determining and understanding its origins, sinks, and impact on tropospheric chemistry.

1.6 Acetone in Breath - as a Biomarker (in DKA)

The experimental set-up designed in this project has potential application as a breath analyser, particularly for breath acetone measurements for the diagnosis of diabetic ketoacidosis (DKA) that is generally experienced by Type 1 diabetic patients. To understand this better, a brief look into normal metabolism and metabolism in diabetic ketoacidosis will be needed. In the human body, carbohydrates are broken down to glucose which is taken up by the body's cells to produce energy. It is important to maintain constant glucose levels in the blood and it must be carefully controlled in order to be a healthy individual. When glucose

levels exceed normal levels, pancreas releases insulin which stimulates glucose uptake from the blood into the cells triggering the process of glycolysis. During this process, glucose is converted to glycogen which is stored in liver and muscle cells for later utilisation by the body. After a few hours of food consumption, glucose levels in the blood decreases and this activates the pancreas to release glucagon [27]. This hormone sends a signal to the liver and muscle cells to commence the process of conversion of stored glycogen back into glucose [28]. Correspondingly, under normal circumstances, Acetyl coenzyme A (acetyl-CoA) is produced by beta-oxidation of fatty acids. In ample availability of glucose, there will be sufficient amounts of oxaloacetate to undergo reaction with acetyl-CoA, which means acetyl-CoA can easily partake in the Krebs cycle, also known as the citric acid cycle as shown in Figure 8. The Krebs cycle involves a series of chemical reactions to release stored energy into adenosine triphosphate (ATP).

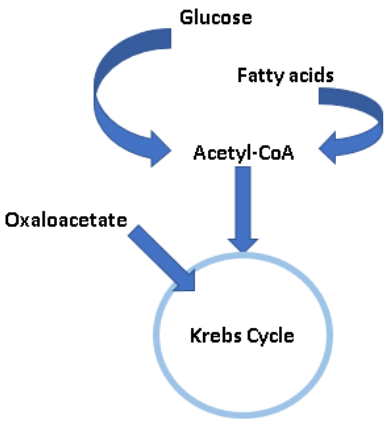

Figure 8 Process of acetyl-CoA entering the Krebs cycle (citric acid cycle). Acetyl-CoA which is formed from the metabolism of glucose and fatty acids enters the Krebs cycle by condensing with oxaloacetate.

But, when glucose levels are low (e.g. during fasting or low levels of insulin in diabetes), more oxaloacetate gets diverted away from taking part in the Krebs cycle. This results in diversion of acetyl-CoA towards ketogenesis (production of ketones) [29] as displayed in Figure 9.

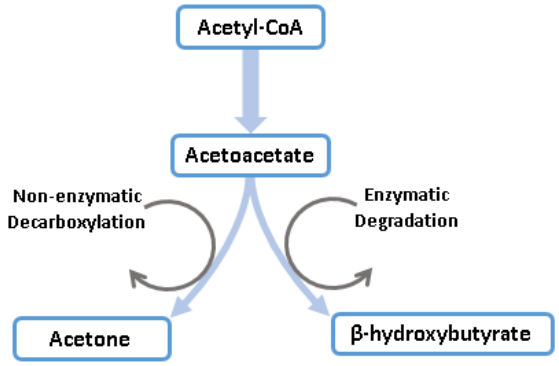

Figure 9 A simplified overview of the various steps involved in the process of ketogenesis.

The increased amounts of fatty acids entering the bloodstream results in increased β-oxidation of fatty acids, which in turn leads to increase in supply of acetyl-CoA into the process. This process is called lipolysis which is normally repressed by insulin [30]. This process usually occurs during starvation phases as starvation ketosis. Starvation leads to decreased insulin levels [31] and increased lipolysis; which in turn results in increased supply of free fatty acids to the liver, thus triggering ketogenesis. Based on glucose levels in the body, acetyl-CoA can be redirected to produce acetoacetate. Acetoacetate can then undergo enzymatic degradation producing β-hydroxybutyrate or non-enzymatic spontaneous decarboxylation to produce acetone (see Figure 9) [29, 32, 33]. These ketone bodies produced during this metabolic process are released into the blood, urine and breath. Due to its small size, acetone easily diffuses into the air spaces of the lungs and hence emerges in respired breath.

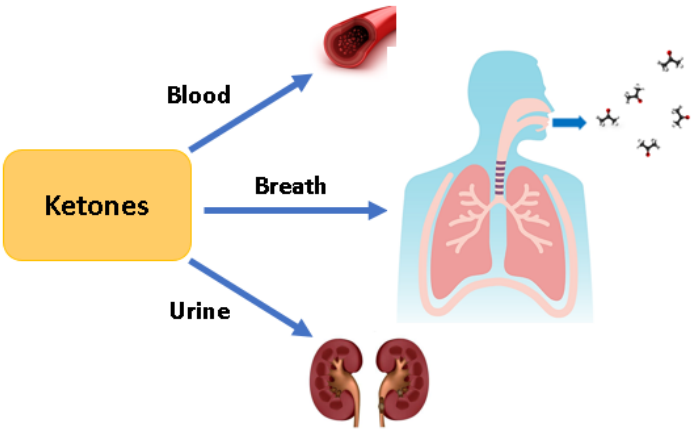

Figure 10 Ketone distribution in human body and acetone in exhaled breath.

1.7 Diabetic Ketoacidosis (DKA)

Diabetes mellitus (DM), which is generally known as diabetes, is a metabolic disorder that affects about 8 % of the world's population [34]. It is a chronic illness that is mostly described by an increase in blood sugar levels and intensive lipolysis [35]. Type 1 and Type 2 diabetes are the two main categories of diabetes.

Type 1 diabetes is a metabolic disorder when the body fails to produce insulin. It is an auto-immune disease where the immune system of the body attacks the β-cells in the pancreas that produce insulin. It can have an effect on people of any age but it is most commonly seen in children and young adults. People experiencing this condition need to regularly inject insulin to control their blood glucose levels. This is a life-threatening condition and lack of access to insulin can lead to death.

Type 2 diabetes is a condition which is predominantly characterised by resistance to insulin and relative insulin deficiency in the body. The majority of diabetic patients fall under this diabetic category. It is mostly caused by obesity and physical inactivity [36].

In cases of disorders where the pancreas fails to produce insulin (as in the case of Type 1 diabetic condition) or when the body cells become insulin-resistant (as in Type 2 diabetes), more and more free fatty acids get through the blood circulation, leading to enhanced ketogenesis. The excess build-up of ketones in the body results in a low pH in blood and tissues [29]. Hence this is referred to as diabetic ketoacidosis (DKA), a life-threatening condition [37].

Most commonly, monitoring of blood ketones (β-hydroxybutyrate) is carried out to check the condition of DKA patients [38]. But the drawback with these monitoring techniques is that they are often an inconvenience to the patients as they are generally invasive in nature. Also, these techniques are time-consuming and lead to under-treating or over-treating of the condition. These drawbacks can be overcome by using real-time techniques to monitor the breath acetone of the patients. Hence, a portable device such as the one currently designed in this project has potential applications as breath acetone analyser for real-time monitoring of the DKA condition.

1.8 Breath analysis

As mentioned previously, one of the potential applications of the new set-up designed in this project is as a breath acetone analyser. This section provides a brief introduction to breath analysis, breath sampling, and acetone breath analysis.

The clinical value of diagnosing a disease from the 'aroma' of exhaled human breath can be drawn back to the times of Greek physicians. Since the time (around 400 BC) Hippocrates, the great Greek doctor, described *fetor oris* and *fetor hepaticus* (in his article on breath aroma and disease), various studies have been carried out to link endogenous metabolites in respired breath and disease. Exhaled human breath comprises carbon dioxide, water vapour, oxygen, nitrogen and trace amounts (parts per million to parts per trillion by volume) of several hundred endogenous volatile organic metabolites. The studies carried out by Pauling et al. which revealed the presence of 250 volatile organic compounds (VOCs) in an average breath sample led to the birth of modern age breath analysis [39]. Some of these VOCs are found to be biomarkers that can provide significant information about certain metabolic disorders and physiological conditions in the human body. For instance, nitric oxide is considered as a biomarker for airway inflammation; ethane and propane are potential biomarkers for oxidative degradation of lipids (that causes cell damage). In addition to this, breath analysis could also be used to detect various exhaled volatile species that are exogenous in origin due to inhalation of polluted air or exposure to toxic compounds [40].

In comparison to direct measurements of the metabolites in blood samples, breath analysis has great prospects as a non-invasive, intrinsically safe and cost-effective approach for disease diagnosis, preventive medication, real-time analysis, response to treatment and metabolic status monitoring. It can also be utilised on people of all age groups and various conditions ranging from infants to critically ill patients without posing any risks to the patients [41, 42]. However, despite some progress, breath presents an analytical challenge since it is transient, humid and since the VOCs are present in trace amounts it requires sensitive instrumentation. In addition to this, breath is a non-homogeneous sample. The initial part of respired breath that comes from the upper airways is the 'dead space air' which does not partake in the gas exchange process. Following this is the 'alveolar air' that results from the gas-exchange that occurs when blood passes the alveolar-capillary interface in the lungs. This

portion of the exhaled air contains highest quantities of volatile metabolites and hence serves as the principal target of analyses.

1.8.1 Breath Sampling

Breath sampling should be quick and easy such that it is suitable for serial monitoring of patients. Breath analysis measurements could be done in either of the two ways: on-line and off-line:

- On-line measurements involve real-time analysis of breath during exhalation.
- Off-line measurements involve collection of breath samples in a suitable bag, sorbent trap or canisters which get analysed later (this requires pre-concentration of breath samples).

The off-line approach has a few drawbacks such as:

- Breath sample lacks reproducibility
- Risks of sample contamination during the storage phase
- Delayed feedback (this can be overcome via on-line approach)

In addition to these challenges, off-line approaches necessitate integration over a complete exhalation or entail further efforts to isolate exhaled dead space air; while with swift on-line approach it is possible to obtain direct access to data regarding concentrations during successive exhalation phases [40].

1.8.2 Acetone Breath Analysis

In 1798, an English physician John Rollo [43] described a smell of decaying apple in respired breath of a diabetic patient, but it was only sixty years later that Petters identified and attributed the odour to acetone [44]. Acetone research gained momentum in the 1980s on various aspects of acetone metabolism in the human body and numerous communications have been published since then [32]. As discussed in section 1.6, acetone which is one of the by-products of fat metabolism normally occurs in exhaled breath during fasting or starving, extreme exercise, ketogenic diet and certain metabolic disorders such as Type 1 diabetes (leading to DKA). These scenarios lead to elevated levels of ketones in blood and exhaled breath [29].

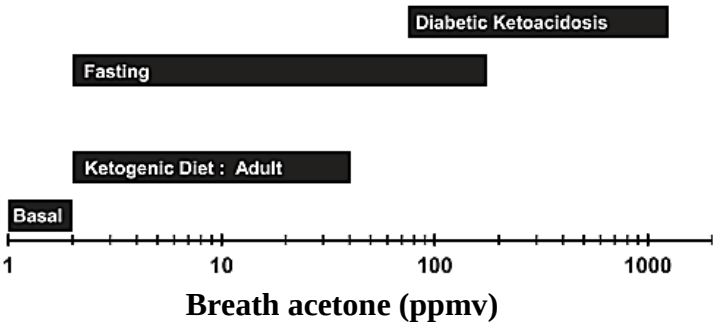

Figure 11 Spectrum for breath acetone displaying range of breath acetone concentrations for different physiological conditions and ketosis ranges [33].

Basal levels of about 1 to 2 ppmv (parts per million by volume) of breath acetone is observed in the case of normal ketosis metabolism. While at the other end of the spectrum, higher levels of about 75 to 1,250 ppmv breath acetone is linked with the DKA condition. Healthy individuals following high-fat, low-carbohydrate diets, calorie restriction diets and fasting have their breath acetone levels between these two extremes as shown in Figure 11 [33].

Various techniques have been developed and adopted for the detection of breath acetone. In 1971, Trotter et al. carried out the first quantitative analysis of breath acetone employing the technique of gas chromatography (GC) in conjunction with flame ionization detectors (FIDs) [45]. Later in 1995, Pleil and Lindstrom used GC in combination with mass spectrometry (MS) to analyse breath acetone with concentrations of 500 – 1000 ppbv [46]. Since then GC-MS has become a standard analytical technique for quantitative analysis of breath metabolites. Even though this technique can provide sensitive analysis of breath, the device is expensive, bulky and immobile (that is they cannot be moved from one room to another on a trolley in a hospital environment). They require trained personnel to operate them and have a time-consuming response. As a result, there is a preference for on-line real-time analysis. Variants of mass spectrometry are being developed as techniques for real-time on-line monitoring of breath acetone, for instance proton-transfer reaction mass spectrometry (PTR-MS) [47] and selected ion flow tube mass spectrometry (SIFT-MS) [48]. Nowadays, ion mobility spectrometry is being used in conjunction with MS for breath acetone analysis [49].

Laser spectroscopic techniques have been gaining widespread applications in quantitative gas analysis due to their ability for selective and sensitive detection of trace compounds in specific wavelength ranges. Techniques like external cavity quantum cascade lasers [50], cavity ring-down laser absorption spectroscopy [51] and diode-laser based cavity enhanced spectroscopy [52] have been used for breath acetone analysis. In addition to these techniques, sensors are also being developed for acetone detection like the portable acetone sensor made of Si-doped epsilon-tungsten trioxide (WO_3) nanostructured film [53]. But these techniques are usually an inconvenience to patients and require pre-concentration of the sample as the metabolites in exhaled breath are lower than the detection limit of most analytical techniques. Recently in 2018, Jing Li et al. demonstrated an acetone analyser based on a UV-light emitting diode near 285 nm in a compact multi-pass cell [54]. However, in this study the samples were collected in Tedlar sampling bags and analysed later. Our research group in collaboration with Durham University is working on building a spectroscopic device for real time on-line monitoring of breath acetone, particularly in the case of DKA. The device will be portable, environmentally robust and cost-effective as it will utilise a UV- LED instead of an expensive laser as an excitation light source.

Chapter 2 - Experimental Technique

The new set-up uses an Incoherent Broadband (IBB) light source such as an LED in place of a coherent monochromatic light source such as a laser which is generally used in most absorption spectroscopy techniques such as Cavity Ring-down Spectroscopy (CRDS). The new set-up employs the technique of IBB Cavity-Enhanced Absorption Spectroscopy (IBBCEAS) to determine acetone concentrations in the background of nitrogen. This chapter provides a brief introduction on absorption spectroscopy, CRDS and IBBCEAS for better comprehension of the experimental approach used in this project.

2.1 Absorption Spectroscopy

Spectroscopy has gained fundamental importance in basic and applied sciences for the study of atomic and molecular systems. The processes of absorption, emission and scattering of electromagnetic radiation have helped gain vital information on the structure and dynamics of molecules and to extensively determine the composition and structure of the Earth's atmosphere [55, 56]. Fundamentally, absorption spectroscopy relies on wavelength dependent absorption of light by molecules. Based on the energy of photons absorbed, absorption spectroscopy can be categorised into ultraviolet (UV), visible which involve electronic transitions in atoms or molecules; infrared (IR) absorption spectroscopy that involve vibrational transitions and microwave spectroscopy that involve rotational transitions of molecules. Absorption spectroscopy techniques can also be broadly grouped into direct and indirect absorption spectroscopy depending on the detection of the phenomenon in the technique. In this thesis only gas phase techniques have been discussed as those in solids and liquids are beyond the scope of this thesis.

Direct absorption spectroscopy is a technique for in situ detection of a species in a sample based on the absorption of light at a given wavelength. Conventional absorption techniques involve the measurement of the amount of light transmitted through the sample. According to the Beer-Lambert law, the absorbance A is proportional to the concentration of the absorbing species c (in moles litre^{-1}) and the sample (or absorption path) length l (in cm).

$$A = \log_{10}\left(\frac{I_0}{I}\right) = \varepsilon c l \qquad (4)$$

where, I_0 and I, are incident and transmitted intensities through the sample respectively, and ε is the molar absorption coefficient (in litre mole^{-1}cm^{-1}) [6]. However, in molecular spectroscopy the quantities are expressed in terms of 'per particle' (no unit) and not 'per mole', and the cross-section and concentration terms are combined to define an absorption coefficient α. Hence, the Beer-Lambert's law equation can be written as:

$$I = I_0 exp(-\alpha l) \qquad (5)$$

where, $\alpha = \sigma\rho$, and σ and ρ are absorption cross-section (in m^2 or cm^2) and ρ is the particle density (in m^{-3} or cm^{-3}). When light passes through the sample, the transmitted light intensity decays exponentially with absorption pathlength. Thus, by measuring the intensities I_0, I and sample length l, α can be determined directly. But in this conventional approach the target species is probed only once and hence, it is a single-pass technique. Although this technique yields quantitative absolute concentrations of atoms and molecules in the gas phase, direct absorption spectroscopic methods suffer from low sensitivities as they measure light attenuation in a large background signal [40]. High sensitivity can be achieved by increasing the absorption pathlengths. The quest to increase the sensitivity with pathlength led to the development and use of multi-pass cells such as the Herriott cell [57] and White cell [58]. In the case of atmospheric chemistry and gas phase samples most of the trace components occur in small concentrations. Hence, long pathlengths are crucial to most spectroscopic analytical techniques for atmospheric studies of trace gas species such as in Differential Optical Absorption Spectroscopy (DOAS). DOAS instruments employ a continuous broadband light source such as a xenon (Xe)-arc lamp and a long pathlength optical set-up to measure narrow band absorption structures in the UV and visible spectral regions [59, 56].

Another way of overcoming the issue of low sensitivity is by employing indirect absorption spectroscopic techniques such as photoacoustic spectroscopy [60], Laser Induced Fluorescence (LIF) [61, 62] or Resonance Enhanced Multi-Photon Ionization (REMPI) [63]. Photoacoustic spectroscopy is based on the detection of pressure changes induced by the absorption of light. Whereas in LIF, fluorescence induced by the absorption of light is recorded. In REMPI, ions created by the absorption of light are recorded by ion time-of-light. The key advantage of these techniques over direct absorption techniques is the detection of these signals over low background signals offering high sensitivities. But, a drawback of these

techniques is that they are not self-calibrating and require difficult calibration procedures to make the techniques absolute [40].

Applications involving the analysis of molecules with small geometrical cross-sections, necessitate that the same sample volume be probed repeatedly. Even though multi-pass approaches could be used in such cases, these conventional approaches require that the light beam travels along distinct paths on each pass. This led to the development of Cavity Ring-Down Spectroscopy (CRDS) by O'Keefe and Deacon in 1988 to overcome this drawback and achieve an almost unbounded effective sample length [64], which is discussed in the following section.

2.2 Cavity Ring-Down Spectroscopy (CRDS)

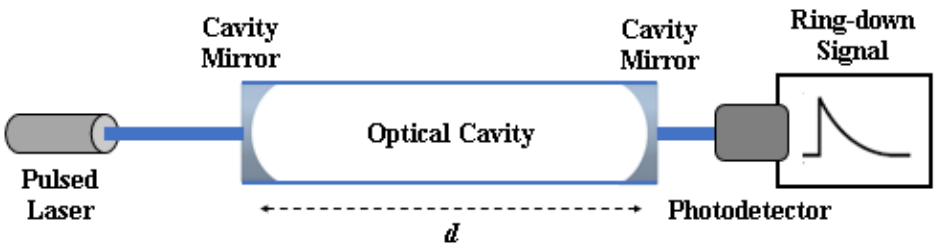

Figure 12 Schematic diagram of a typical Cavity Ring-Down Spectroscopy experimental set-up.

CRDS was first employed by O'Keefe and Deacon (in 1988) to study the vibrational overtones of gaseous molecular oxygen [64]. The key principle of operation of CRDS is not based on the measurement of the intensity of light but rather on the rate of absorption of a sample located within a closed optical cavity. A conventional CRDS set-up as shown in Figure 12 consists of a stable optical cavity (an optical resonator) which is created using a pair of identical, highly reflective (R > 99.9 %), dielectric coated plano-concave mirrors separated by a distance d and with a radius of curvature R_c. The criterion for a stable optical cavity is: $0 \leq (1 - d/R_1)\ (1 - d/R_2) \leq 1$, where R_1 and R_2 are the radii of curvature of the cavity mirrors [40]. A pulsed laser beam is aligned along the axis of the optical cavity. The cavity mirrors are aligned in such a way that the incident light is trapped and is bouncing between the same spots on the mirrors within the cavity. Every time a laser pulse strikes the mirror, a small amount of its intensity leaks out of the cavity and the laser pulse intensity decays in a single exponential manner. This exponential decay of light can be detected using a suitably sensitive light detector such as a photo multiplier tube (PMT) placed after the rear cavity mirror.

As already stated, CRDS is not concerned with measuring the light intensity that exits the optical cavity, rather it is the lifetime of the decay that is analysed, and this decay is termed as the ring-down time (RDT). In the presence of an absorbing medium within the cavity, the concurrence of cavity transmission losses along with absorption loss due to the Beer-Lambert's law result in a single exponential decay but with a shorter ring-down time. The photodetector placed behind the rear cavity mirror records the decaying intensity of light that is transmitted through the mirror.

Overall, CRDS has two main advantages:

- Multiple passes through the sample increase the effective pathlength which consequently gives rise to increase in sensitivity. As a result enabling detection of samples with concentrations as low as ppbv and pptv (parts per trillion by volume) [40, 65, 66].
- Since the measured ring-down time is independent of the absolute intensity of the light injected into the cavity, the technique is largely insensitive to noise due to shot-to-shot intensity fluctuations of the light source [67].

2.2.1 Ring-Down Time and Absorption Coefficient

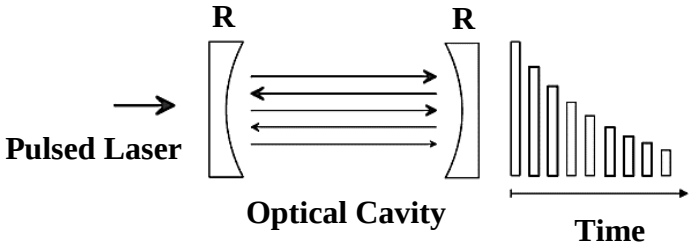

Figure 13 Illustration of the description the 'photon bullet model' of the pulsed CRD technique [40].

The intensity of light detected after the first pass through the optical cavity can be given by the Beer-Lambert law as (from Equation 5) [40],

$$I_0 = I_{laser} T^2 \exp(-\alpha d) \qquad (6)$$

where, α is the absorption coefficient, $I_{laser}$is the intensity of light coupled into the optical cavity of length d (here the sample pathlength l is considered the same as the cavity length d) and T is the transmission of the cavity mirrors. After one round trip, the intensity of light is

given as, $I_1 = I_0 R^2 \exp(-2\alpha d)$, where R is the reflectivity of the cavity mirrors. Therefore, after n round trips, the intensity of light at the detector will be,

$$I_n = I_0 R^{2n} \exp(-2n\alpha d) \quad (7)$$

The number of round trips $n = \frac{ct}{2d}$, where, c is the speed of light and t is the time over which light has travelled within the optical cavity. Substituting $R^{2n} = \exp(2n \ln R)$ in Equation 7, and using the approximation $\ln R \approx R - 1$, which holds true for high reflectivity mirrors, the time dependent light intensity $I(t)$ is given by,

$$I(t) = I_0 \exp\left(-\frac{ct(1 - R + \alpha d)}{d}\right) \quad (8)$$

Defining the ring-down time (RDT) of the cavity as the time for intensity of the signal to decay to $1/e \approx 0.37$ of its original value:

$$\tau = \frac{d}{c(1 - R + \alpha d)} \quad (9)$$

Therefore, Equation 8 becomes,

$$I(t) = I_0 \exp\left(-\frac{t}{\tau}\right) \quad (10)$$

When the duration of the laser pulse width is shorter than the round trip time ($t_r = 2d/c$), the RDT signal on the detector appears as a series of peaks as shown in Figure 13. And when the pulse width is of the order of the round trip time of the pulse in the cavity or longer, the RDT signal on the detector appears as a smooth exponential [40]. By determining the RDT in the presence and in the absence (τ_0) of the absorbing species, its absorption coefficient can be calculated as,

$$\alpha = \frac{1}{c}\left(\frac{1}{\tau} - \frac{1}{\tau_0}\right) \quad (11)$$

2.2.2 Variants of CRDS

There are many variants of CRDS apart from the conventional CRDS that uses nanosecond scale laser pulses. One such variant is Continuous-Wave (CW) CRDS where the light source is used in continuous emission mode rather than pulsed mode. In 1997 Romanini et al. [68, 69] and Paldus et al. [70] employed CW laser light source in conjunction with fast optical switching to carry out high-sensitivity measurements. One of the advantages

of CW laser sources (such as diode lasers) is their compact size and low energy consumption in comparison to pulsed laser sources making them a good candidate of light source for integration into portable devices. Despite this the CW-CRDS approach adds complexity to the experimental set-up and has limited availability of diode lasers especially in the UV spectral region. A good summary of CW-CRDS can be found in the review by Brown [71].

Other variants of CRDS include Broadband (BB) CRDS which adopts an approach different from that of the conventional CRDS approach in the sense that the conventional CRDS approach employs a narrowband monochromatic light source while BB-CRDS uses a light source of broader emission spectrum. As a result, light exiting the optical cavity consists of a mixture of different wavelengths with distinct ring-down times. This cavity output which is broadband in nature can be resolved as a function of wavelength, or as a function of time over a selected spectral range, or as a simultaneous function of both wavelength and time as shown in Table 1 [40].

When conventional CRDS is used in investigations of absorption spectra of species it requires the determination of the time constant at each wavelength of interest by collection of many laser pulses which can be time consuming. The two-dimensional broadband cavity ring-down spectroscopic techniques in Table 1 use spectrally broadband pulsed light source providing wavelength and time resolved photograph of a single ring-down event where the output signals are simultaneously analysed at varying wavelengths. These techniques find applications in time-dependent environmental monitoring and in observing the dynamics of chemical reactions [72]. This approach has the major advantage of the conventional CRDS technique in terms of being independent of intensity fluctuations in the output of the light source [73]. Despite these advantages, these techniques are complex due to the distinct nature of their detectors [40]. The BB-CRDS techniques were employed in the detection of broadband absorbers such as NO_3 radical [73, 74], NO_2 [72], other species such as molecular oxygen and water vapour [73] and other trace gas species such as I_2 and OIO for atmospheric studies [75].

Wavelength resolved, time integrated methods 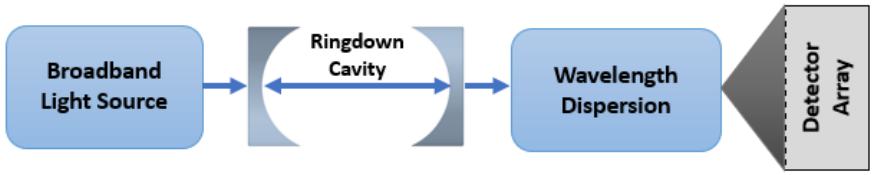	• Incoherent broadband cavity-enhanced absorption spectroscopy using xenon arc-lamp [76 – 78] • Incoherent broadband cavity-enhanced absorption spectroscopy using an LED [79, 80] • Multiplex integrated cavity output spectroscopy [81] • Broadband mode-locked enhanced absorption spectroscopy [82] • Fourier transform (incoherent) cavity-enhanced absorption spectroscopy [83]
Time resolved, wavelength selective methods 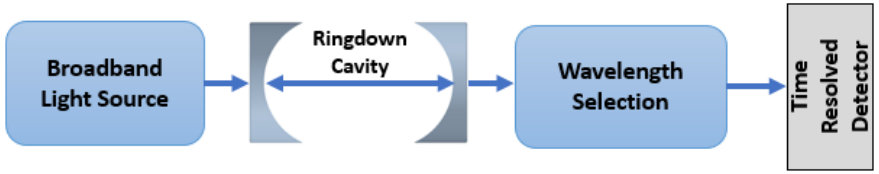	• Pulse-stacked cavity ring-down spectroscopy [84] • Cavity ring-down spectroscopy of thin films in the mid-IR [85] • Fourier transform cavity ring-down spectroscopy [86] • Fourier transform phase-shift cavity ring-down spectroscopy [87] • Cavity attenuated phase-shift spectroscopy [88, 89]
Wavelength & time resolved two dimensional methods 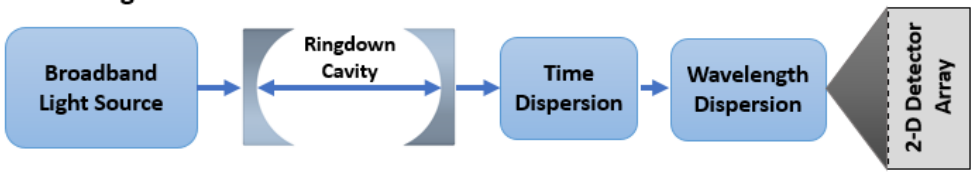	• Broadband ring-down spectral photography [90, 91] • Frequency comb broadband cavity ring-down spectroscopy [92] • Broadband cavity ring-down spectroscopy [73] • Cavity ring-down spectrography [72]

Table 1 Variants of Broadband Cavity Ring-Down Spectroscopy [40, 93]. The reader is pointed to the cited references for more information on the spectroscopic techniques mentioned in this table.

The one-dimensional broadband cavity ring-down techniques involve detection of time-dependent signals over a narrow range of wavelengths or the detection of wavelength resolved time-integrated signals. In Fourier transform (FT) spectrometer by Engeln and Meijer [86], the output of a broadband dye laser was coupled into a CRDS cavity and the light exiting the optical cavity was coupled into a FT spectrometer that was utilised to choose a wavelength range from the cavity output. The ring-down transients (wavelength integrated) for different subgroups of wavelengths exiting the cavity were recorded at well-defined arm length differences of the interferometer. Hamers et al. [87] extended this methodology using phase shift (PS)-CRDS technique with a continuous incoherent broadband light source (intensity modulated output from Xe-arc lamp). In this FT-PSCRDS technique, the wavelength selection was carried out before coupling light into the optical cavity. The absorption coefficient of the sample is determined from the phase shift of the intensity modulated light, which occurs as a result of the time delay introduced by the optical cavity. Ruth et al. [83] combined the techniques of incoherent broadband cavity-enhanced absorption spectroscopy (IBBCEAS) and FT-PSCRDS using an incoherent broadband light source (Xe-arc lamp) to carry out FT-IBBCEAS. In FT-IBBCEAS the wavelength selection was carried out with a high-resolution Michelson interferometer at the exit end of the cavity. Since in this technique the sample volumes can be kept small, the technique enabled the measurements of weak absorbers or trace gas species in a variety of different environments and samples that are often inaccessible via conventional broadband absorption spectroscopic techniques. A drawback of FT spectrometry in comparison to conventional IBBCEAS is that the measurement times are significantly longer. Additionally, in comparison to IBBCEAS, intensity fluctuations from the light source introduce noise in the resulting spectra measured using the FT approach [83]. Therefore, FT methods require highly stable light sources to minimise the noise due to intensity fluctuations. Kebabian et al. [88] employed a modulated incoherent broadband light source (a 430 nm LED) for the detection of NO_2 using cavity attenuated phase shift (CAPS) spectrometer. The presence of a sample within the cavity adds towards the change in the magnitude of the detected phase angle of the modulated light which aids in the detection of the gas species. The amount of trace gas species within the cavity can be obtained from the phase shift measured by this technique.

In cavity-enhanced absorption spectroscopy (CEAS), light that enters the optical cavity continuously replenishes photons that are lost within the cavity as a result of absorption by the

medium or due to transmission or absorption losses occurring at the cavity mirrors. As a result, the intensity of light reaches a steady-state within the cavity. Using a CW narrowband laser, Engeln et al. [94] showed that at steady-state the intensity of light transmitted through the optical cavity is directly proportional to the ring-down time of the cavity. Similarly, in the case of a broadband light source, each wavelength attains its own steady-state intensity which depends on the intensity of the light source and the various loss processes experienced by these photons within the cavity which in turn are related to their ring-down times. Thus, in BBCEAS the cavity output is a time integrated spectrum of the steady-state intensities transmitted by the cavity which is then resolved in wavelength using a suitable spectrometer or charge-coupled device (CCD) detector [40]. The cavity-enhanced approach for pulsed excitation of the optical cavity, termed as Integrated Cavity Output Spectroscopy (ICOS), was introduced by O'Keefe [95], who demonstrated that the integrated absorption signal provides a quantitative total attenuation measurement with sensitivity comparable to that achieved with CRDS. Thus, CEAS is an experimentally simpler variant of CRDS that can provide the necessary absorption information without the need to measure the ring-down transient as the resulting signal is proportional to the RDT of the cavity [94]. The BBCEAS systems are less expensive to set-up in comparison to CRDS systems as BBCEAS do not require expensive pulsed laser sources or the need to employ fast detectors to measure the ring-down transients. IBBCEAS techniques employing CW light sources such as xenon-arc lamps and LEDs are discussed in the following sections of this chapter. Another category of BBCEAS exists, those which employ broadband pulsed lasers rather than CW light sources [81, 82]. The application of high-energy light sources in these techniques yielded high intensity light signals exiting the cavity and therefore high signals at the detectors. As a result, these techniques required shorter integration times in comparison to the BBCEAS techniques that employed incoherent light sources.

2.3 Cavity-Enhanced Absorption Spectroscopy

In comparison to CRDS technique which is time-dependent, Cavity-Enhanced Absorption Spectroscopy (CEAS) is an intensity-dependent technique which involves the measurement of time-integrated intensity of light exiting the optical cavity. While experimental simplicity can be achieved with CEAS in comparison to CRDS, it has two drawbacks. Firstly, in CEAS it is not possible to determine the absolute absorption coefficient of the sample directly, while CRDS yields an absolute measurement. Therefore, CEAS requires calibration with a sample of known absorption coefficient or the mirror reflectivities

must be known in order to obtain the absolute absorption coefficient of the sample. In the case of CRDS, an empty cavity measurement can be carried out to determine the mirror reflectivities. Secondly, as CEAS involves the measurement of intensity of light rather than the rate of decay of light within the cavity, the signal-to-noise ratio that can be achieved with CEAS is dependent on the stability of the excitation light source [93].

In the last few decades, CRDS and its related techniques have undergone rapid development. Since the late 1980s, the concept of using incoherent broadband light source instead of a monochromatic coherent light source (such as a laser) has been considered inappropriate mostly due to lower brightness of these incoherent light sources and also their low coupling efficiencies to high finesse optical cavities [96]. Despite these adverse features, many advantages of using an incoherent broadband light source for CEAS encouraged significant number of applications of this technique. In the case of most broadband CEAS techniques, wavelength selection is done after the cavity, which eliminates the requirement for scanning the wavelength. This in turn, presents the option of multiplexed light detection. Despite the low coupling efficiency of incoherent broadband light into high finesse optical cavities at any given time, for a given cavity length and certain radius of curvature of mirror and its size, the light will contain frequencies that will correspond to the modes of the cavity. Consequently, a certain amount of light will always couple into the optical cavity [93]. In atmospheric studies which demand simultaneous detection and monitoring of several species or those with broad absorption features necessitate techniques covering broad spectral regions instead of requiring high spectral resolution [76]. Nonetheless, in broadband CEAS the detection scheme that is employed determines the spectral resolution of the technique.

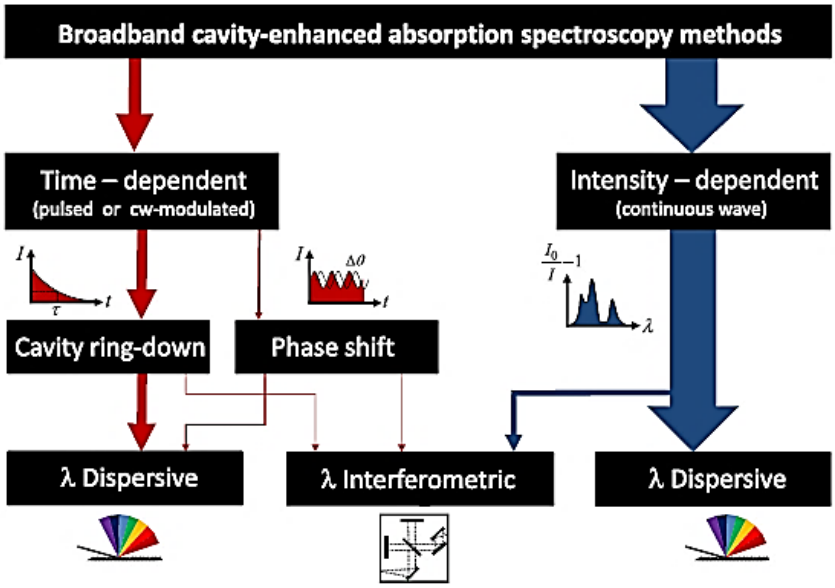

Figure 14 An overview of classifications of Broadband CEAS approaches and detection schemes. The thickness of the arrows represent the relative number of incidences of the kind of approach in the literature [93].

Figure 14 above shows an overall classification of broadband CEAS techniques. Experimental BB CEAS methods can be generally classified into two types [93]:

a) Time domain methods that are based on the measurement of photon storage time within the optical cavity (also described as CRDS). In this approach, pulsed (or cw-modulated) light is employed as an excitation light source.
b) Intensity domain methods that generally involve the measurement of broadband light intensity transmitted through the optical cavity (also termed as CEAS methods). This approach commonly employs continuous wave light sources.

2.4 Incoherent Broadband Cavity-Enhanced Absorption Spectroscopy

In 2003, Fiedler et al. demonstrated a new highly sensitive method of Incoherent Broadband Cavity-Enhanced Absorption Spectroscopy (IBBCEAS) for absorption measurements of gaseous samples using a white-light source (short-arc Xe-Lamp). Since this method eliminates the use of a (diode-) laser it can be considered as an amalgam of a CEAS technique [94] and a conventional absorption technique whereby a high sensitivity is maintained [76]. Generally, in IBBCEAS the wavelength selection of light is carried out after it exits the optical cavity either by interferometric or dispersive approach. Similar to other

CEAS techniques, in IBBCEAS the transmitted intensities are measured in the presence and absence of the absorber. As already mentioned, CEAS does not provide absolute absorption coefficient of the sample and hence involves a calibration step of determining the effective reflectivity of the cavity.

Rayleigh (elastic) scattering losses of calibration gases can be used to determine the effective reflectivity by measuring the ratio of transmitted intensities when the cavity is filled with He or N_2 or zero air at different pressures or He/N_2 mixture. As the Rayleigh scattering cross-sections of these gases are known, the effective mirror reflectivity can be determined as,

$$R(\lambda) = 1 - \left(\frac{\left(\frac{I_{N_2}}{I_{He}}\right) \alpha_r^{N_2} - \alpha_r^{He}}{1 - \left(\frac{I_{N_2}}{I_{He}}\right)} \right) d \qquad (12)$$

where $\alpha_r^{N_2}$ and α_r^{He} are the extinction coefficients for Rayleigh scattering of N_2 and He respectively. Chen and Venables used the same principle using N_2 and CO_2 [97]. The benefit of this approach is that Rayleigh scattering extinction coefficients vary uniformly with wavelength over the entire spectrum in a well-defined manner, thus enabling reflectivity measurements throughout the UV and visible spectral regions.

With IBBCEAS it is possible to record a broad spectral range for the detection of many species at once. However, a drawback is that the spectral resolution of IBBCEAS is inherently lower compared to CEAS and other diode-based-laser techniques. In comparison to multi-pass DOAS systems, the IBBCEAS techniques are superior in terms of high spatial resolution and high sensitivity. DOAS set-ups involve large sample volumes, which as a result limit the sensitivity of the set-up due to inherently low light intensities along with significant amounts of scattered light. As a result, DOAS set-ups require longer integration times, they have low spatial resolution and are commonly not portable. The advantages of IBBCEAS are the simplicity of the experimental set-ups, they are straightforward to setup and economical to operate [76].

2.4.1 Determination of Absorption Coefficient

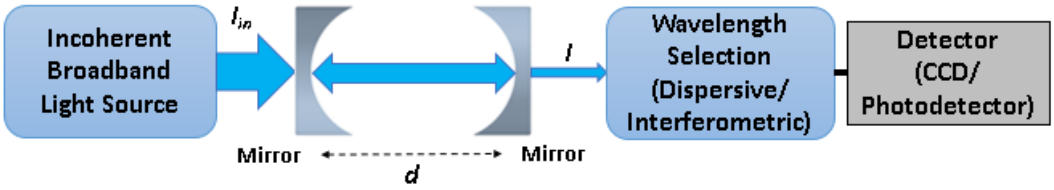

Figure 15 Basic schematic diagram of a typical experimental set-up employed in IBBCEAS.

An optical cavity is formed by two highly reflective plano-concave spherical mirrors ($M_1$and M_2) with reflectivities $R_1$and R_2 (effective reflectivity, $R(\lambda) = (R_1R_2)^{1/2}$) separated by a distance d. Consider incoherent light of intensity I_{in} being injected into the cavity (see Figure 15). Let $L(\lambda)$ be the light loss due to absorption, scattering and diffraction, and I be the intensity of the light transmitted through the cavity [93].

$$I = I_{in}(1-R)^2(1-L)\sum_{n=0}^{\infty}(1-L)^{2n} \qquad (13)$$

Equation 13 can also be written as,

$$I = I_{in}\frac{(1-R)^2\,(1-L)}{1-R^2\,(1-L)^2} \qquad (14)$$

For a resonator with no sample losses ($L = 0$) Equation 14 becomes,

$$I_0 = I_{in}\frac{1-R}{1+R} \qquad (15)$$

Considering the attenuation of light per pass occur due to absorption as described by the Beer-Lambert law,($(1-L(\lambda) = \exp(-\alpha(\lambda)\,d)$), the absorption coefficient $\alpha(\lambda)$ of the absorbing sample can be given as:

$$\alpha(\lambda) = \frac{1}{d}\left|\ln\left[\frac{1}{2R^2(\lambda)}\left(\sqrt{4R^2(\lambda)+\left(\frac{I_0(\lambda)}{I(\lambda)}(R^2(\lambda)-1)\right)^2}+\frac{I_0(\lambda)}{I(\lambda)}(R^2(\lambda)-1)\right)\right]\right| \qquad (16)$$

regardless of the magnitude of loss per pass, αd. For smaller losses *($L \rightarrow 0$)* and higher values of mirror reflectivities *($R \rightarrow 1$),* the absorption coefficient $\alpha(\lambda)$ can be approximated as [93]:

$$\alpha(\lambda) = \frac{1}{d}\left(\frac{I_0(\lambda)}{I(\lambda)} - 1\right)(1 - R(\lambda)) \qquad (17)$$

As seen in Equation 17, contrary to time domain methods where mirror reflectivities can be determined by carrying out empty cavity measurements, $(1 - R(\lambda))$ needs to be calibrated in the case of IBBCEAS in order to determine the absolute absorption coefficient $\alpha(\lambda)$ of the sample.

2.5 Light Emitting Diode

As this project employs a Light Emitting Diode (LED) as a light source, this section provides a brief discussion on the working principle of an LED. An LED is a solid-state semiconductor optoelectronic device that generates light via the phenomenon of electroluminescence. It has an active region comprising a p-n junction which is formed when a p-type semiconductor is brought in contact with an n-type semiconductor. This region serves as the main component of an LED which emits light under the influence of an applied electric field [98].

Figure 16 shows a simplified circuit and energy diagram of an LED when a forward bias voltage is applied across the p-n junction. At the p-n junction, due to the presence of a concentration gradient, i.e., the presence of holes on the p-side and electrons on the n-side, diffusion of charge carriers occurs across the p-n junction leading to recombination. This results in residual negative charges on the p-side and residual positive charges on the n-side forming a depletion region around the junction that is devoid of mobile charge carriers [99]. A resultant electric field is formed in this region by the residual charges which generates a potential energy difference (φ_B) between both the p- and n- sides, opposing any further exchange of charge carriers at equilibrium. On applying a forward bias to the p-n junction, the applied voltage difference (V_D) overcomes the potential energy difference thus disturbing the equilibrium. A current flows across the interface when electrons are injected from the n-side to the p-side. Electrons from the conduction band of the n-side combine with holes in the valence band of the p-side, releasing excess energy in the form of light and heat. The energy difference between the conduction and valence band energy levels is called 'bandgap'. This intrinsic property of the semiconductors determines the amount of energy released as well as

the wavelength of the light emitted. The bandgap and consequently the wavelength of emitted light can be tailored by employing different semiconducting materials and using different doping impurities at varying concentrations [100].

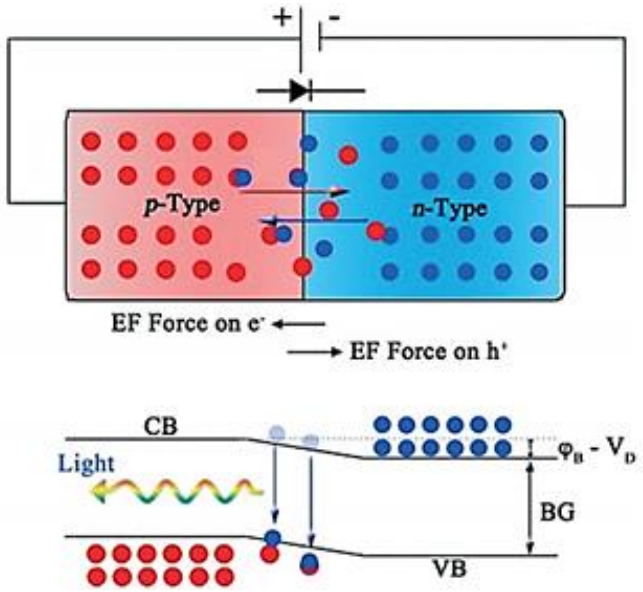

Figure 16 Simplified circuit and energy level diagram of a forward biased p-n junction of an LED [100]. Holes (h^+) from the p-region and electrons (e^-) from the n-region diffuse across the junction resulting in the formation of depletion region that lacks any mobile charge carriers. At equilibrium, this generates an electric field (EF) that opposes any further exchange of charge carriers. When a forward bias is applied across the p-n junction, this equilibrium is disturbed causing a flow of current across the junction as electrons are introduced from the n-region into the p-region. When electrons from the n-region conduction band (CB) combine with holes in the p-region valence band (VB), photons and heat with an energy equivalent to the bandgap (BG) of the semiconductor is emitted.

LEDs are compact, robust, power efficient, cost-effective and exhibit long lifetimes (up to >10000 hours). LEDs are available off-the-shelf with wavelengths ranging from near IR to the near UV (up to 220 nm). As this research project is mainly concerned with the UV-LED other spectral regions have not been discussed further. In recent years, research and development in UV-LED technology has observed a rapid growth due to increasing use of UV-LEDs in UV disinfection in the field of water treatment [101], sterilization and disinfection, bio-sensing, medicines [102], in curing of coatings [103] and controlled-environment agriculture [104].

The availability of off-the-shelf LEDs operating at various wavelength ranges ranging from near IR to the near UV has led to its utilisation as an alternative light source in spectroscopy. LEDs have numerous advantages over the more commonly employed lasers. Major benefits of using an LED over pulsed lasers are its compact size, low-cost, low energy consumption, robustness to temperature variations, low maintenance costs and long lifetimes. The broad emission spectrum of an LED can serve as an advantage in terms of being able to choose different wavelength ranges using a suitable wavelength selection approach. The broadband emission of an LED makes it possible to analyse mixtures of trace gas species that absorb at different wavelengths. This characteristic can also be a disadvantage when the emission spectrum is broader than the high reflectivity range of the cavity mirrors requiring spectral filtering to get rid of the undesirable wavelengths. Lasers (and cw-diode lasers) on the other hand, generally have the advantage of not requiring wavelength-selection and produce much higher output powers.

2.5.1 IBBCEAS with LEDs

In 2004, Ball et al. first demonstrated the use of LEDs in IBBCEAS [105] in the green (535 nm) and the red (661 and 665 nm) wavelength regions to carry out quantitative absorption measurements of trace amounts of three atmospherically important absorbers (NO_3, NO_2 and I_2). Since then LEDs have been widely used in gas phase spectroscopy in the visible as well as in the near-UV regions. A few years later, Langridge et al. developed a compact low power detector based on IBBCEAS for in situ measurements of atmospheric NO_2 using a high intensity LED array with an emission spectrum peaking at 455 nm [106]. In 2008, Gherman et al. [80] carried out the first IBBCEAS in the near-UV for the simultaneous detection of HONO and NO_2 in the wavelength range between 360 and 380 nm using high power LED. Triki et al. [107] and Ventrillard-Courtillot et al. [108] employed LEDs centred around 623 and 625 nm respectively, for the simultaneous detection of both NO_3 and NO_2 by IBBCEAS. Wu et al. in 2009 carried out IBBCEAS of NO_2 in laboratory ambient air with an LED at 455 nm [109] and in 2014 developed a UV-LED based IBBCEAS instrument for the simultaneous detection of HONO and NO_2 in ambient air around 365 nm [110]. Donaldson et al. [111] used a UV-LED centred around 368 nm in a cavity-enhanced absorption spectrometer to measure gas phase products released during HONO uptake on the soil surface. Scharko et al. [112] carried out CEAS measurements of HONO and NO_2 produced during the photodegradation of aqueous nitrate under acidic conditions using a UV-LED centred around

368 nm. In 2016 Min et al. [113] carried out aircraft IBBCEAS measurements of various trace species in the wavelength regions centred around 455 nm and 365 nm. Nakashima and Sadanaga [114] employed a UV-LED centred around 365 nm for validation of in situ measurements of atmospheric HONO using IBBCEAS. In 2018, Duan et al. [115] used a similar UV-LED in their IBBCEAS instrument. Recently in 2019, Jordan and Osthoff [116] used an LED centred around 367 nm for quantifying HONO and NO_2 in ambient air by IBBCEAS in the wavelength range between 361 – 388 nm. The UV-LED based IBBCEAS set-ups discussed here employed LEDs with high optical output power and these set-ups were able to quantify trace gas species like HONO and NO_2 as low as ppb and ppt.

Other incoherent light sources for IBBCEAS include:

- Xe-arc Lamps – emit white light continuum covering wavelengths from the start of the vacuum UV to the near IR (250 – 800 nm) [117]. In the context of IBBCEAS, it was first used in 2003 by Fiedler et al. [76]. Other applications of Xe-arc lamps in IBBCEAS include the works of Fiedler et al. [118, 119], Ruth et al. [83], Orphal et al. [120], Venables et al. [78], Vaughan et al. [121], Washenfelder et al [122], Dixneuf et al. [123], Nitschke et al. [124] and Chen et al. [97, 125]. Some issues encountered with Xe-arc lamps are that the intensity and shape of emission lines are influenced by the fluctuations in temperature and pressure of Xe-gas. The Xe-arc lamp emission can complicate the CEAS retrievals of certain species as seen in the case of Washenfelder et al. [122] where the Xe-gas emission lines overlapped with the spectral features of glyoxal [126]. LEDs in comparison to Xe-arc lamps have unstructured emission spectra that are stable with time, compact in size, much more power efficient, have longer life-time and do not require strong cooling [107, 126]. In terms of spectral filtering of out of band light i.e., wavelengths of light where the reflectivity of the cavity mirror falls, LEDs emit less light at these wavelengths compared to emission from a Xe-arc lamp.

  Superluminescent LEDs that generate emission over a broad wavelength range (from 5 to 100 nm) also exist. These SLEDs provide beam divergence and output power density comparable to a laser diode, but with broad emission and low temporal coherence of a conventional LED [127]. Denzer et al.[128] used a fiber-coupled near-IR SLED emitting light in the wavelength range 1.62 – 1.7 μm in combination with a BBCEAS for absorption measurements of 1,3-butadiene.

- Halogen Lamps – these have a continuous smooth emission spectrum ranging from the near-UV to near-IR region. However, lower brightness and big size of emitting filament make these lamps less attractive for use in IBBCEAS applications [93].
- Supercontinuum Sources (SC) (White Fibre Lasers) – these have broad emission spectrum ranging from about 400 nm to the near IR (to above 2000 nm) which enables them in simultaneous detection of multiple species. In SC sources the spectral broadening is produced by pumping a certain length of a strongly non-linear device such as a micro-structured photonic crystal fiber (PCF) with short optical pulses (fs to ns) from a seed laser [129]. SC sources are susceptible to showing considerable power and spectral fluctuations which are undesirable for CEAS applications. These sources also show considerable performance instabilities due to optical feedback into the PCF attributable to the strong back reflection from the entrance cavity mirror (particularly while working around the seed wavelength) [93]. In 2008, Langridge et al. used a supercontinuum source for the first time in the spectral range of 630 – 700 nm for the detection of NO_3 and NO_2 by BBCEAS [130].

Chapter 3 - Experimental Build

One of the aims of this project was to design a portable detector based on a UV-LED for detection of trace gas species in atmosphere and in exhaled breath. In addition to this aim, this project was also a proof of principle that a UV-LED based detector is feasible instead of a conventional laser-based detector. Thus, to carry out these proof of principle tests with a UV-LED, the LED set-up was integrated into the experimental set-up available in our laboratory. Modifications were made to the laboratory system to make it compatible for measurements in this project. Hence, the main objectives of this chapter are:

3.1 Employ the laboratory experimental set-up to carry out measurements for this project

3.2 Design a portable set-up

3.1 Laboratory Experimental Set-up for Acetone Measurements

The schematic diagram of the experimental set-up (which will be referred to as set-up 1 in this chapter) employed for acetone measurements using IBBCEAS is as shown in Figure 17. The main parts of the experimental set-up are the sample-containing chamber with optical cavity and the optical set-up which is explained in detail in section 3.1.2 and the far more detailed discussion in, section 4.9. The central chamber is a CF 6-way 6" stainless steel cube with CF100 flanges on each side. The side arms supporting the cavity mirror mounts (see section 3.1.1) extend on either side along the main axis of the chamber resulting in a cavity length of d = 37.52 ± 0.07 cm.

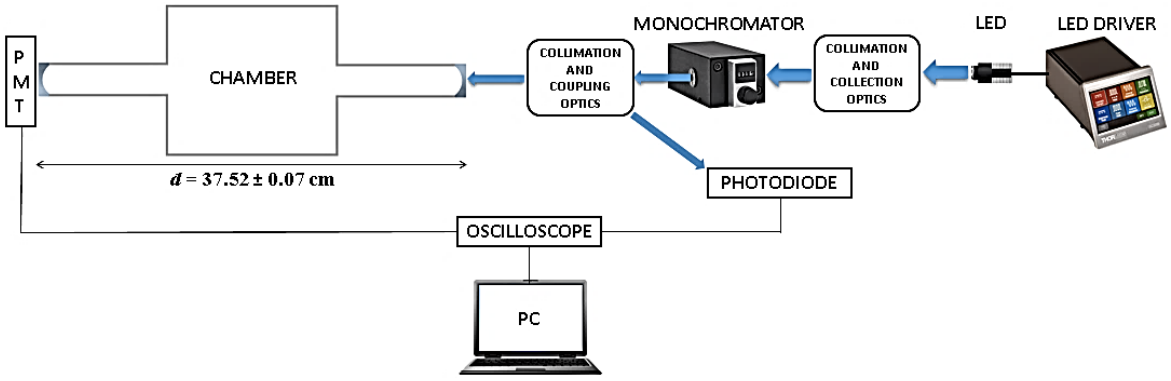

Figure 17 A simplified schematic diagram displaying different units of the laboratory experimental set-up employed for the LED based CEAS absorption measurements of acetone in this project.

A mounted 300 nm LED (M300L4, Thorlabs) with a typical output power of 32 mW (minimum output power 26 mW and manufacturer specified FWHM of 11 nm) is used as an excitation light source for CEAS measurements in this project. An LED driver (DC2200, Thorlabs) powers the 300 nm LED in a continuous mode up to a maximum driving current of 350 mA. Light from the LED is coupled into the optical cavity via a monochromator (for wavelength selection) using suitable collimation, collection and coupling optics. A detailed discussion on the optical set-up is given in section 3.1.2. The admission of gases into the chamber is carried out via the gas manifold system which is described in section 3.1.3 and 3.1.4. The photodetectors used here are a photomultiplier tube (PMT) to measure the cavity output intensity and a photodiode (PD) to measure the input light intensity by capturing some of the stray light that is reflected off the entrance cavity mirror. These outputs are connected to two channels of an oscilloscope (Picoscope 5244A, Pico Technology). The output signals are recorded simultaneously using the Picoscope 6 software on the PC. Every recorded data set comprises 32 traces with a total of 320128 data points for a given output signal (Picoscope settings:15-bits for 2-channel mode with an effective resolution of 13-bits, sampling rate 10 kS/s, and range ±10 mV).

3.1.1 Cavity Mirrors and Mirror Mounts

An optical cavity is constructed using a pair of highly reflective (>99.9 %, Ø25.0 mm) plano-concave mirrors (Transmission ~0.03 % low loss, radius of curvature = 1000 mm, #139542, Layertec GmbH). The reflectivity and transmission curves of the mirrors as provided by the manufacturer are shown in Appendix A.5. The cavity mirrors are mounted on a stainless-steel washer with the help of grub screws to hold them in place. The washer is inserted into a cavity mount top that has three fine adjustment screws attached to aid with cavity alignment. The cavity mirrors are pressed against the mount base attached to the side arms of the main system via an O-ring (see Figure 18).

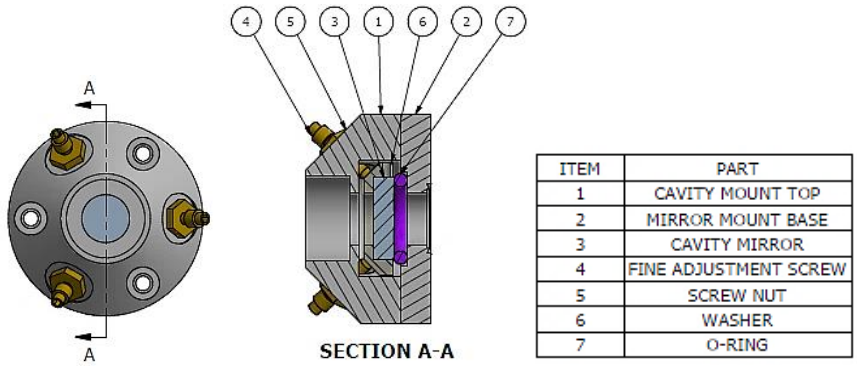

ITEM	PART
1	CAVITY MOUNT TOP
2	MIRROR MOUNT BASE
3	CAVITY MIRROR
4	FINE ADJUSTMENT SCREW
5	SCREW NUT
6	WASHER
7	O-RING

Figure 18 Top view and cross-sectional view of the cavity mirror mount assembly used with the main chamber system of the experimental set-up.

3.1.2 Optical Set-up

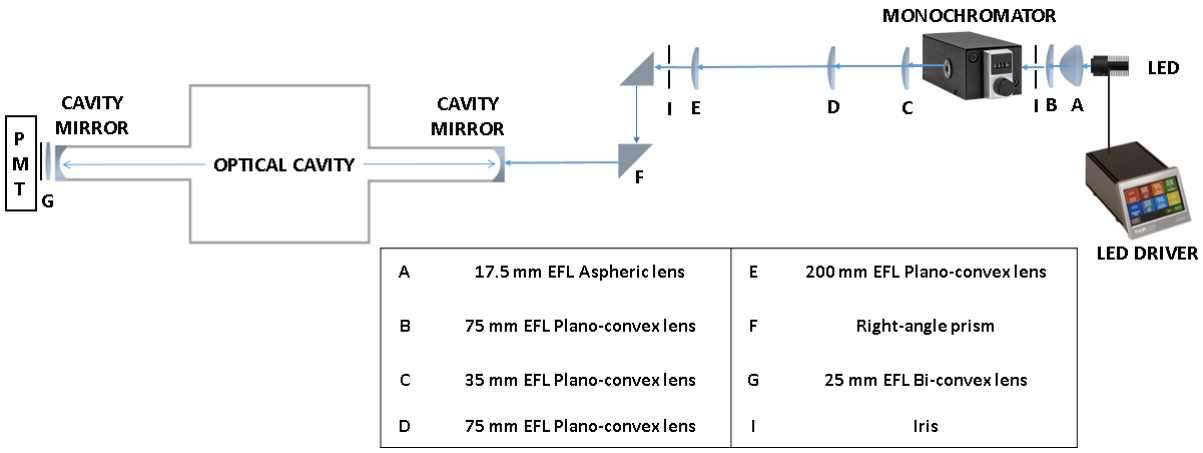

A	17.5 mm EFL Aspheric lens	E	200 mm EFL Plano-convex lens
B	75 mm EFL Plano-convex lens	F	Right-angle prism
C	35 mm EFL Plano-convex lens	G	25 mm EFL Bi-convex lens
D	75 mm EFL Plano-convex lens	I	Iris

Figure 19 Schematic diagram of the components of collimation, collection and coupling optics employed in the LED-based experimental set-up for CEAS measurements. The photodiode capturing the stray light reflected off the entrance cavity mirror to monitor the intensity of LED light is not shown here for simplicity.

Several optical configurations were tried and tested to obtain optimum collimation and coupling of LED light into the optical cavity (see Chapter 4). Since the LED output is uncollimated it is used in conjunction with suitable collimation and collection optics comprising an aspheric lens and a plano-convex lens for guiding the high bandwidth light into a manual Mini-Chrom monochromator (Model 37-597, Edmund Optics, see Appendix A.4 for details) for wavelength selection. For measurements carried out in this project, the monochromator was fitted with 600 μm slit set with light exiting centred around 297 nm (with a FWHM of ~4.4 nm) using the dial on the monochromator (which is calibrated beforehand).

The light exiting the monochromator is collected with a combination of optics and steered into the optical cavity with a pair of right-angle prisms as shown in Figure 19. The LED light intensity (I_{in}) entering the optical cavity is monitored with a photodiode that captures some of the stray light being reflected off the entrance cavity mirror. A 25 mm focal length aspheric lens is used to focus the stray light onto the photodiode along with a neutral density filter (optical density = 2). The cavity output intensity (I) is measured using a PMT placed behind the rear cavity mirror (see Figure 19). A 25 mm focal length bi-convex lens is used to focus the cavity output onto the PMT along with a Thorlabs FGUV11 filter to cut-off any stray light (bandpass region 275 – 375 nm). The intensity I_{in} is used to eliminate the fluctuations in the intensity of the LED light during the CEAS measurements. Thus the intensity I_{in} is used to normalise the PMT signal (I) during the measurements. As these intensities are measured with two different detectors with different responsivities and bias voltages, and as the PD captures just a small amount of the incident LED light, the resulting output signal I/I_{in} is often > 1.

To measure the light within the cavity (replicating light after the front cavity mirror), the spectrometer was placed behind an identical cavity mirror after the monochromator and the spectrum was measured (as shown in Figure 20).

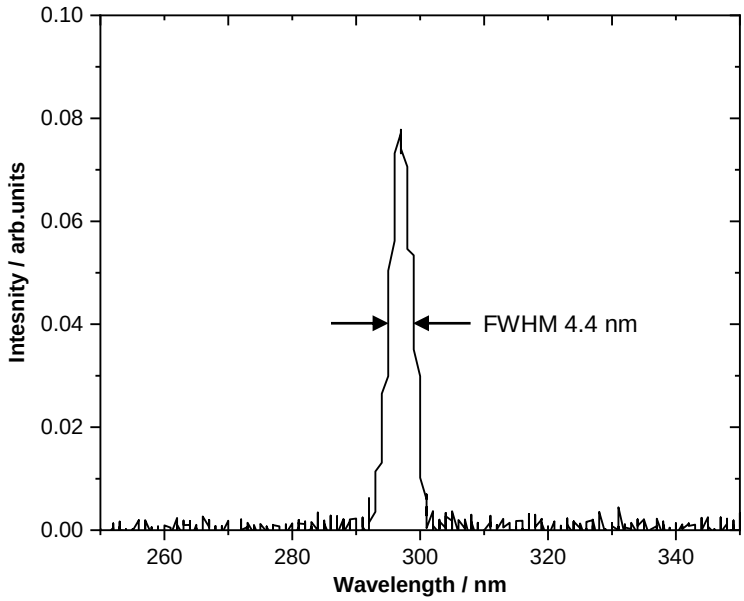

Figure 20 Spectrum of light measured behind the first cavity mirror (showing wavelengths of light within the optical cavity). The spectrum was measured using the CCS200/M spectrometer at an integration time of 10 s.

3.1.3 Gas manifold

To control admission and pumping of gases into the chamber for CEAS and Rayleigh scattering measurements, a gas manifold system was linked to the experimental set-up as shown in Figure 21. Various components of the gas manifold were connected by means of ¼" and 6 mm pipes using Swagelok and Ham-let fittings linking to the main system via CF and KF fittings. Figure 21 shows a simplified schematic diagram of this gas manifold employing standard process symbols for various components of the system.

	Model	Range / mbar
C1	MKS-Baratron 626A-1000	0.13 – 1333
C2	Inficon CDG020D	0.5 – 1100
C3	Leybold SKY Inficon CR090	6.6×10^{-3} – 13.33

Table 2 Pressure gauges employed in the experimental set-up used for CEAS measurements.

The main chamber system has a volume of about 3.5 L. To monitor and read out pressures, capacitance manometers C1, C2 and C3 (in Table 2) were attached to the system as shown in Figure 21. During the measurements in this project, the pressures were read using the capacitance manometer C1 which has an error of 0.25 % on its reading (specified by the manufacturer). Temperatures were monitored with thermocouples (TC) attached to each arm of the main assembly. These thermocouples had an error of 1 % on the readings (as specified by the manufacturer). Pumping out gases from the chamber was achieved utilising a scroll pump (Edwards nXDS10iC) via a regulating valve. The chamber system could achieve an absolute pressure of the order of 10^{-3} mbar (monitored with capacitance manometer C3). An N_2 cylinder (BOC-oxygen free) for Rayleigh scattering measurements was connected to the chamber via pneumatic valve 1. Helium (BOC CP grade) was filled into a 1 L cylinder prior to measurements and connected to the manifold via pneumatic valve 2. About 100 ml of acetone (HPLC grade) was put in a round bottomed Schlenk flask coupled to the gas manifold via metal to glass O-ring sealed connection. The air inlet via a diaphragm valve was used to vent the chamber and cavity assembly. It was also used to flush out He from the chamber during N_2/He measurements.

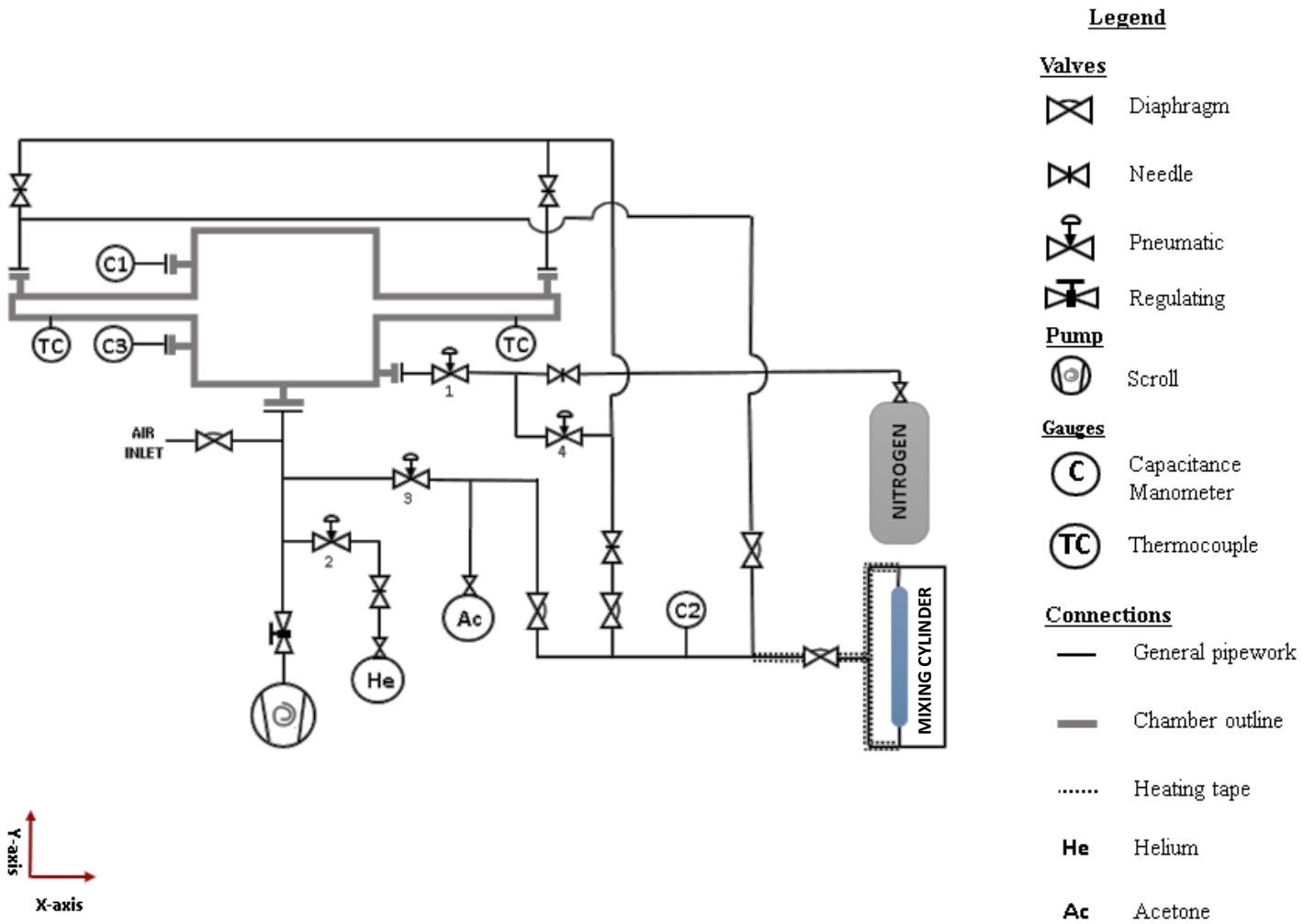

Figure 21 Gas manifold for controlled admission and pumping of gases linked to the chamber in the XY-plane. The chamber is represented as an over simplified schematic. The main flange-to-flange connections to the chamber are indicated by lines terminating perpendicular to the pipework. Additional flange components included within the main pipework are represented as straight lines for simplicity and clarity.

3.1.4 Gas Mixture - Preparation and Admission

Acetone/N_2 (Ac/N_2) gas mixtures were used to carry out absorption measurements of acetone in a N_2 background. Gas mixtures were prepared in a 0.5 L mixing cylinder connected to the gas manifold as shown in Figure 21. Several freeze-pump-thaw cycles were carried out to thoroughly degas acetone before transferring it to the mixing cylinder. A small amount of acetone was first admitted into the cylinder and then topped up to a total pressure of 1000 mbar with N_2. Gas mixing within the mixing cylinder was achieved by means of convection process. This was facilitated by a heating tape wound round the cylinder pipes of dissimilar lengths as shown in Figure 21. This approach also prevented acetone from sticking to the walls of the mixing cylinder. The pressures on the mixing cylinder section were monitored using the capacitance manometer C2.

The gas mixture was gradually admitted into the chamber in a controlled manner via the exit end cavity arm of the main assembly. The mixture in the chamber was then filled to a total pressure of 1000 mbar with N_2 via a needle valve and pneumatic valve (1) combination located at the centre of the chamber. Measurements were carried out after a waiting time of ~21 mins for thorough equilibration of the gas mixture within the chamber system.

3.2 Design of a Portable Set-up

The design of the set-up was achieved while bearing these three key objectives in mind:

1. Portability
2. Cost-effectiveness
3. Robustness

This section gives details on how these objectives can be accomplished with the portable set-up (which will be referred to as set-up 2 in this chapter).

3.2.1 Cage system and Mirror Mounts

In 2016, Min et al. carried out aircraft measurements of glyoxal (CHOCHO), methylglyoxal (CH_3COCHO), nitrous acid (HONO), nitrogen dioxide (NO_2) and water vapour (H_2O) using IBBCEAS [113]. Their set-up involved two channels, channel 365 and 455 with wavelength ranges 361 – 389 nm and 438 – 468 nm respectively. With channel 365 HONO

and NO_2 were detected while in channel 455 CHOCHO, CH_3COCHO, NO_2 and H_2O were detected. The optical set-up used two temperature-controlled LEDs centred around 365 nm and 455 nm. The light from the LEDs was coupled into the two optical cavities of length 48 cm with off-axis parabolic mirrors that provided both optimised photon throughput and space efficiency. The light exiting the optical cavity was imaged by an off-axis parabolic mirror and coupled into a grating spectrometer and thermoelectric cooled CCD detector via a coupling lens and fiber optic bundle. The optical components were mounted in a cage system which comprised six carbon fiber rods and mounts to attach each optical component to the rods. This system provided robust and stable optical alignment that was insensitive to vibrations, pressure and temperature variations. The admission of gases into the optical cavities was achieved with a flow system wherein the two cavities were connected to separate mass flow controllers to maintain a constant flow rate in each cavity. Overall, Min et al.[113] have claimed to have achieved robust performance using this custom designed optical mounting system (shown in Figure 22) which was insensitive to aircraft vibrations and rapid changes in ambient temperature and pressure.

The current set-up in the laboratory (set-up1 shown in section 3.1) is immobile for the purpose of field measurements as it is bulky and not mechanically rigid. The optical components of the set-up, although fixed, are susceptible to change in alignment with variation in pressure, vibration or movement. Therefore, in order to provide the set-up with mechanical rigidity and robust optical alignment, the set-up will need to be integrated into a cage system in order to achieve the purpose of portability of the set-up. To build a robust portable experimental set-up, the type of cage system and hardware used in the IBBCEAS instrument employed by Min et al. in their field measurements shown in Figure 22 were adapted.

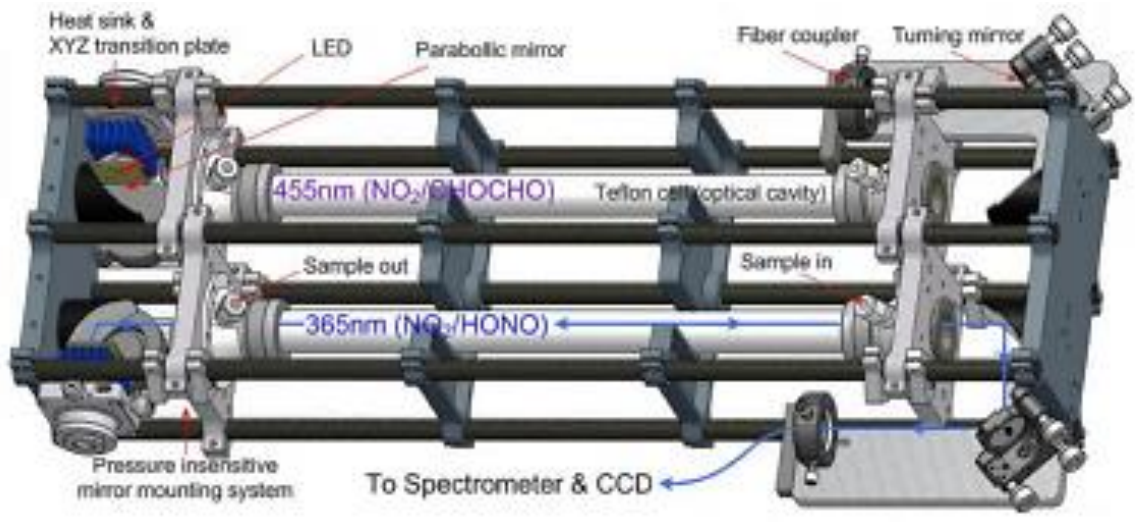

Figure 22 Schematic of the Airborne Cavity Enhanced Spectrometer (ACES) assembly taken from Min et al. [113]. The figure shows the LEDs, collimation optics, optical cavity and cage system with six carbon rods.

The main criteria for the set-up to be deployable in the field are:

- Mechanical rigidity
- Robust optical alignment
- Insensitivity to vibration, and
- Environmentally robust – being insensitive to temperature and pressure fluctuations

This section gives a detailed discussion on meeting these criteria using set-up 2. This set-up mainly comprises a cage system (including cage rods and cage plates), an optical cavity and cavity mirror mounts (see Figure 23).

The various optical elements are mounted in a cage system with overall dimensions 500 mm x 200 mm x 200 mm as shown in Figure 23. The cage system consists of four invar rods with an outer diameter (OD) of 22 mm and four custom-designed aluminium cage plates of dimensions 200 x 200 mm^2 with provisions made for mounting the optical components into the system. These cage plates are aligned and secured parallel to each other on the invar rods with the aid of clamps providing robust optical alignment without the need of commercial spring-loaded mirror mounts. The combination of aluminium cage plates and invar rods provides the system with high mechanical rigidity [131]. The final alignment of the cage plates can be achieved using fine adjustment screws (F25SS150, Thorlabs) that are attached to the

clamps at all four corners of the cage plate. As shown in Figure 26 in the portable set-up design, the cage plates can be held in place with the help of clamps with springs (part number 3 in Figure 26) to preserve the alignment and eliminate backlash.

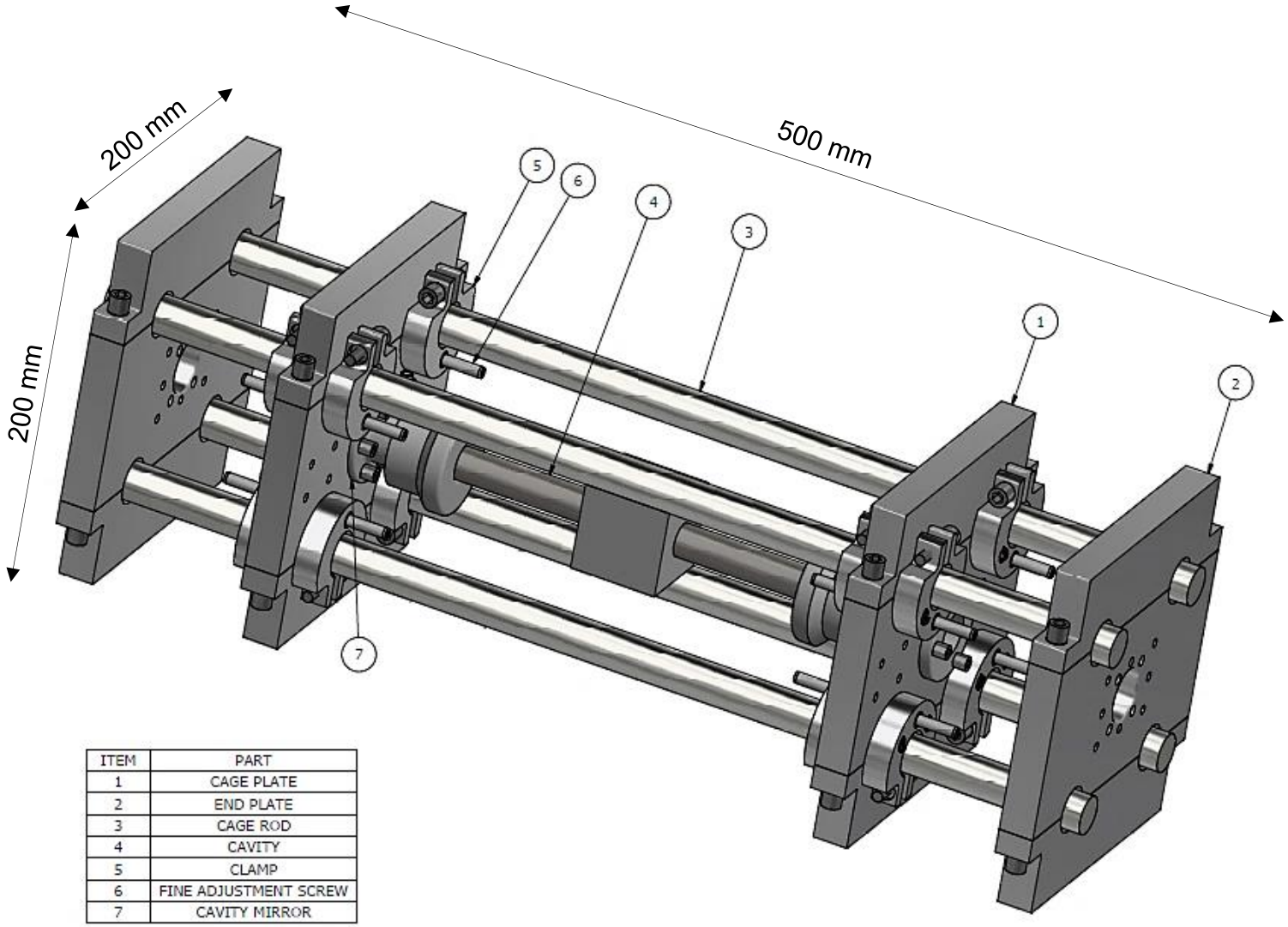

ITEM	PART
1	CAGE PLATE
2	END PLATE
3	CAGE ROD
4	CAVITY
5	CLAMP
6	FINE ADJUSTMENT SCREW
7	CAVITY MIRROR

Figure 23 Assembly of the portable set-up showing the cage system made up of invar cage rods and custom-designed aluminium cage plates.

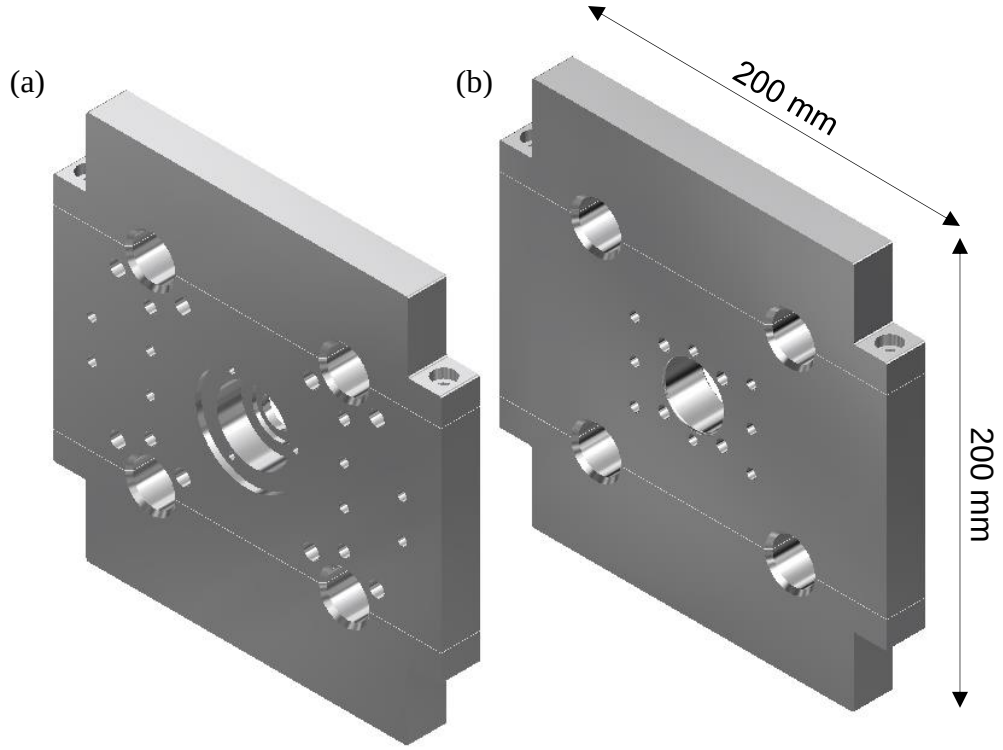

Figure 24 Custom-designed aluminium (a) cage plate and (b) end plate of the portable set-up. Also showing provisions made for incorporating optical components into them.

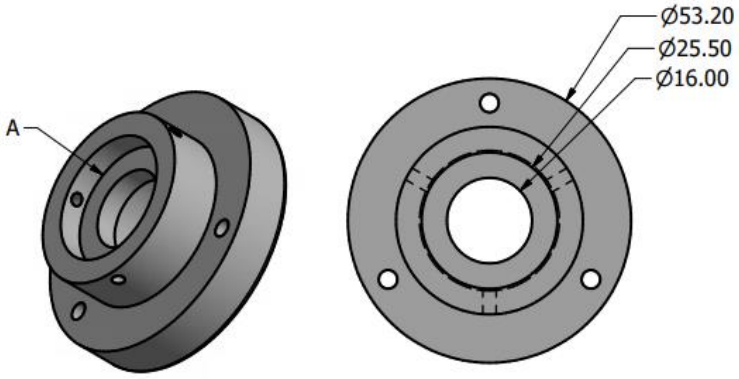

Figure 25 Isometric view and top view of the new cavity mirror mounts for the portable set-up. The cavity mirrors (Ø25 mm) sit in the location marked 'A' in the figure.

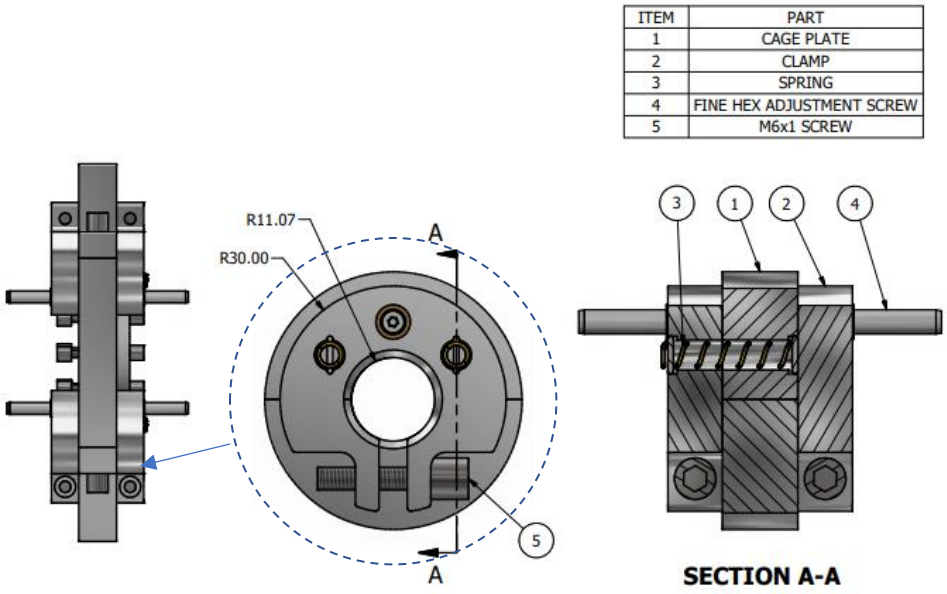

Figure 26 Side view of a cage plate showing detailed view of the clamp and spring in the cage plate assembly of the portable set-up.

The cavity mirror mounts on the set-up used for acetone absorption measurements (set-up 1 shown in section 3.1.1) are sensitive to pressure variations in the chamber. The alignment is fairly stable i.e., the alignment goes back to its previous position as long as the pressure differential between outside and inside the cavity is the same. The alignment is affected if there is a pressure differential across the mirror. Also, it was observed that the cavity alignment does not remain stable for different pressures of nitrogen during the corresponding Rayleigh scattering measurements as discussed in section 5.1.1.3. In the experimental set-up 1, there is a constant pressure exerted from the outside using the adjustment screws but, on the inside, has a compressible O-ring that may lead to variations. Hence, to overcome this issue in set-up 2, the cavity mirrors are mounted and sealed onto the cage system by using compressed O-rings on the aluminium plates as presented in Figure 27 (a) and (b). This allows the mirror face to be in full contact with the aluminium cage plate, consequently eliminating variable compression of O-rings with varying cell pressure and therefore providing minimum pressure sensitivity. Overall, the portable set-up 2 provides stable optical alignment that does not necessitate re-alignment and is largely insensitive to vibrations, and temperature, or pressure variations [113]. Thus, integrating the optical set-up with this custom-designed cage system will provide high mechanical rigidity, stability and robustness to the experimental system. Consequently, with this new set-up 2 it will be feasible to carry out field measurements of gas

species outside laboratory setting and it also has the potential to be used as a portable breath acetone analyser in a medical environment.

(a)  (b) 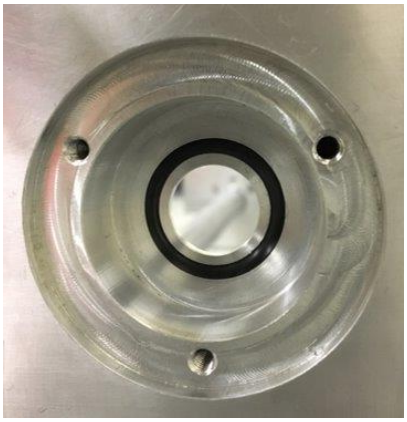

Figure 27 (a) New mirror mount and (b) its corresponding aluminium plate with O-ring of the portable set-up.

3.2.2 Detection System

Keeping in mind the three main objectives to build the portable set-up, the detection system should also match the criteria of being compact, robust and inexpensive. A photodiode meets all these criteria in comparison to a PMT as a detector. A photodiode is a solid-state detector which offers compactness and robustness which are vital in miniaturizing the set-up. A PMT on the other hand is a vacuum phototube detector which is prone to getting damaged while moving the set-up around. Also, a photodiode does not require a high-voltage power supply in contrast to a PMT. More details on the photodiode and the PMT used in this project can be found in Appendix A.

Photodiodes can be used to detect the intensity changes in CEAS when wavelength-resolved intensity measurements are not of concern. A CEAS technique requiring wavelength-resolved intensity measurements require a spectrometer as a detection system. A spectrometer is a solid-state detector that comprises an array of detectors and grating that can analyse a wide range of spectrum simultaneously. A spectrometer (a dispersive element) has low sensitivity and dynamic range, has no gain and requires cooling to maintain stability with varying temperatures. A PMT (a non-dispersive wavelength integrating element) has greater sensitivity and dynamic range. In this project with a 300 nm LED, using a spectrometer for intensity measurements was not possible as there was not enough light for detection of intensity

changes above the limiting threshold of the compact spectrometer (CCS200/M, Thorlabs). In the near future with more powerful LEDs becoming available in the 300 nm range, intensity measurements will be feasible with cost-effective and compact spectrometers like the one used in this project. Appendix A.3 gives more information on the spectrometer employed in this project to determine the spectra during various preliminary tests with the LED and to measure the spectrum of light entering the optical cavity.

3.2.3 Conclusion

From this chapter the feasibility of a portable and environmentally robust acetone analyser that is insensitive to vibrations, temperature and pressure variations can be understood. The combination of new mirror mounts with the cage system will provide the system with a robust alignment. The cage system will provide the system with high mechanical rigidity and enables portability of the set-up outside the laboratory environment. Commonly used laser-based detector set-ups often necessitate the laboratory to be equipped with an air-conditioned system to maintain stable temperature conditions. Also, these set-ups require expensive stable optical tables to minimise the influence of vibrations. In addition to the hardware upgrade proposed for the portable set-up, employing an LED as the light source adds to the robustness, cost-effectiveness and compactness of the experimental set-up. Also, the use of an LED as excitation light source involves lower maintenance costs in comparison to other light sources. Ultimately, the aim with the portable set-up is to have an analyser which once aligned with the whole optical set-up can be handed over to another person to carry out the measurements e.g. a nurse in a hospital. Another potential application is to operate the set-up in a remote location to carry out field measurements with the set-up powered by a battery.

Chapter 4 - Characterisation of 300 nm LED

Using an LED instead of a laser in CEAS offers opportunities (as discussed in section 2.5) but also poses unique challenges. The challenges of working with an LED in this project mostly involved collimation of the highly divergent LED output beam and coupling the light from the LED light into an optical cavity, which are discussed in detail in the following sections. Various configurations tried and tested in building the optical set-up are also discussed. Furthermore, this chapter presents simulations of the optical cavity response considering the spectral characteristics of the LED and the enhancement factor for the CEAS technique employing the 300 nm LED.

4.1 Selection of LED

As the carbonyl group (C=O) in acetone is responsible for the absorbance of UV radiation occurring around 300 nm which corresponds to the transitions between non-bonding orbitals (n) to anti-bonding orbitals (π^*) (as discussed in section 1.2.1), the light source for the absorption measurements of acetone needed to be in the UV-region of the electromagnetic spectrum. There are a number of LEDs available off-the-shelf in this wavelength range (220 – 300 nm), however, there are some specifications that need to be investigated, particularly in terms of overlap with the acetone absorption spectrum, lifetime of the LED and output power. In this wavelength range, the 300 nm LED was determined as the best fit for this project in comparison to other off-the-shelf LEDs available at the time. The chosen 300 nm LED is an uncollimated, mounted LED (M300L4) from Thorlabs that comprises a single LED attached to the end of a heat sink.

Figure 28 shows a normalised intensity emission spectrum of the 300 nm LED superimposed on the absorption cross-section of acetone. Here it is observed that the spectral overlap between the LED emission and acetone absorption spectrum is larger than for a narrow-band laser (represented by the dashed line in Figure 28). However, the power density (W/cm^2) of a laser is typically higher than for an LED.

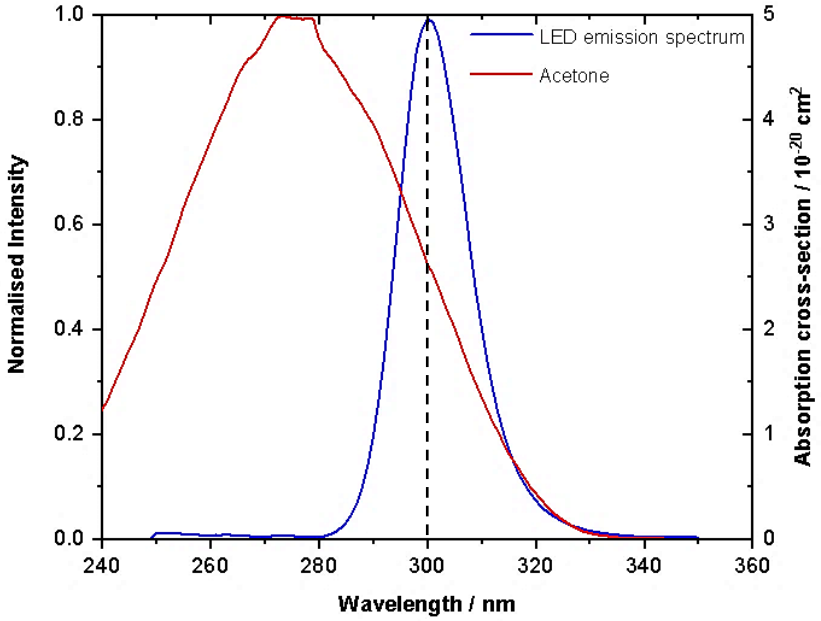

Figure 28 Superimposed plots of normalised intensity emission spectrum of the 300 nm LED (data as obtained from the manufacturer, Thorlabs) and absorption cross-section of acetone obtained from the MPI-Mainz UV/VIS spectral Atlas [9]. The dashed line represents a laser at the corresponding wavelength.

4.1.1 Emission Spectrum of the 300 nm LED

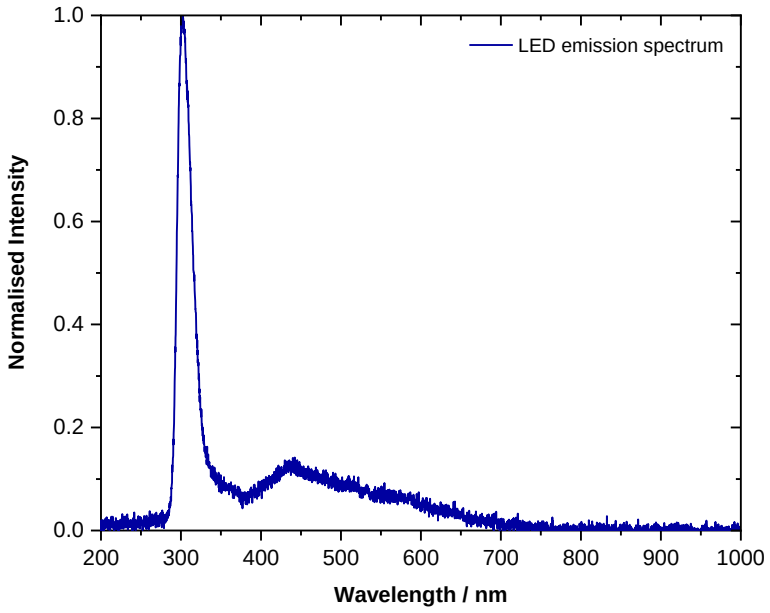

Figure 29 Normalised spectral output intensity as a function of wavelength of the 300 nm LED measured with spectrometer. The LED was operated at its maximum driving current.

The normalised emission spectrum of the 300 nm LED when operated at its maximum driving current, as measured with CCS200/M spectrometer (Thorlabs), is shown in Figure 29. From Figure 28 and Figure 29 it can be seen that the actual emission spectrum of the LED measured varies from that specified by the manufacturer. The actual spectral light output peaks around 302 nm with an overall bandwidth of ~22 nm (as opposed to 11 nm bandwidth specified by the manufacturer). Additionally, the LED exhibits a broad spectral feature in the wavelength range between 350 – 700 nm.

From Figure 30, it is evident that the LED has an emission bandwidth much broader than the high reflectivity range (273 – 323 nm) of the cavity mirrors. This gave rise to the challenge of spectral filtering of wavelengths outside the high reflectivity range of the cavity mirrors in order to suppress the detection of undesirable light that is non-resonant in the cavity and therefore will not benefit from cavity-enhancement, creating a potentially large baseline signal.

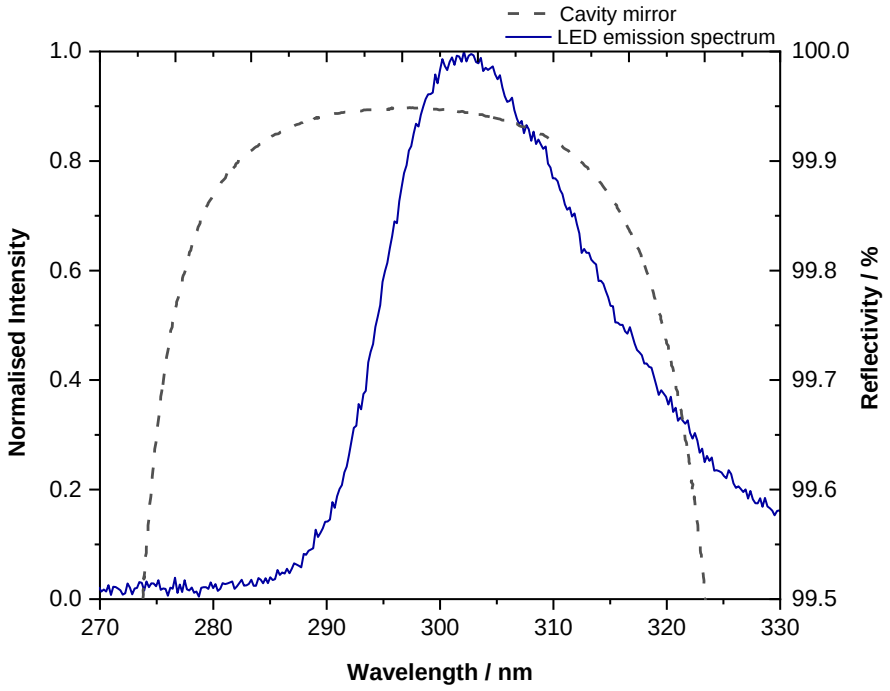

Figure 30 LED spectral output superimposed on the reflectivity curve of the 300 nm cavity mirror.

4.2 Cavity Mirrors as Spectral Filters

As seen in Figure 30, the LED emits light even beyond the high reflectivity range of the cavity mirrors and thus requires spectral filtering of this undesirable light. From the reflectivity and transmissivity curves shown in Figure A. 6 (a) and (b) (in Appendix A.5), it can be seen that theoretically these mirrors reflect ~99.9 % of the incident light within the high reflectivity range of 273 – 323 nm while wavelengths beyond this range get transmitted through the mirrors to a much larger degree. Hence, a few different configurations where the cavity mirrors were effectively employed as spectral filters were setup as shown in Figure 31 (a) and (b).

(a)

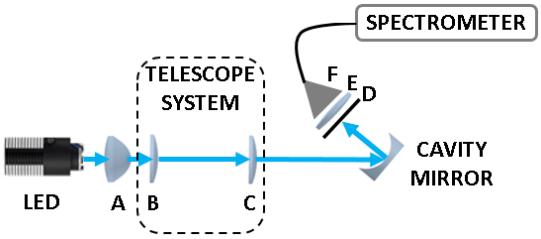

(b)

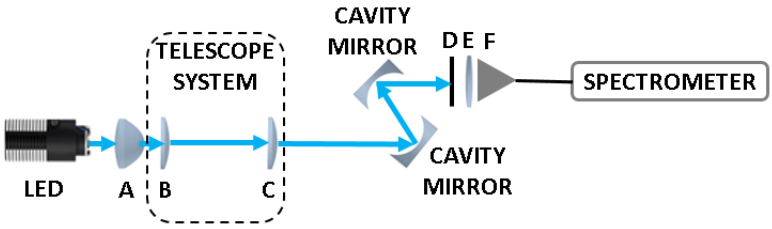

Figure 31 Optical set-up showing different configurations (a) using one-cavity mirror and (b) using two-cavity mirrors as spectral filters. A-Aspheric lens, lenses B and C constitute the Telescope system, D-Neutral density filter, E-Focusing lens and F-Fiber coupler.

Light from the LED is collimated by an aspheric lens and the beam size is reduced using the telescope system. This light is then reflected off the cavity mirrors for spectral filtering. The filtered light is then attenuated with a neutral density filter before coupling it into the spectrometer via a fiber coupler as shown in Figure 31 (a) and (b). The spectral outputs of different configurations are shown in Figure 32 for comparison.

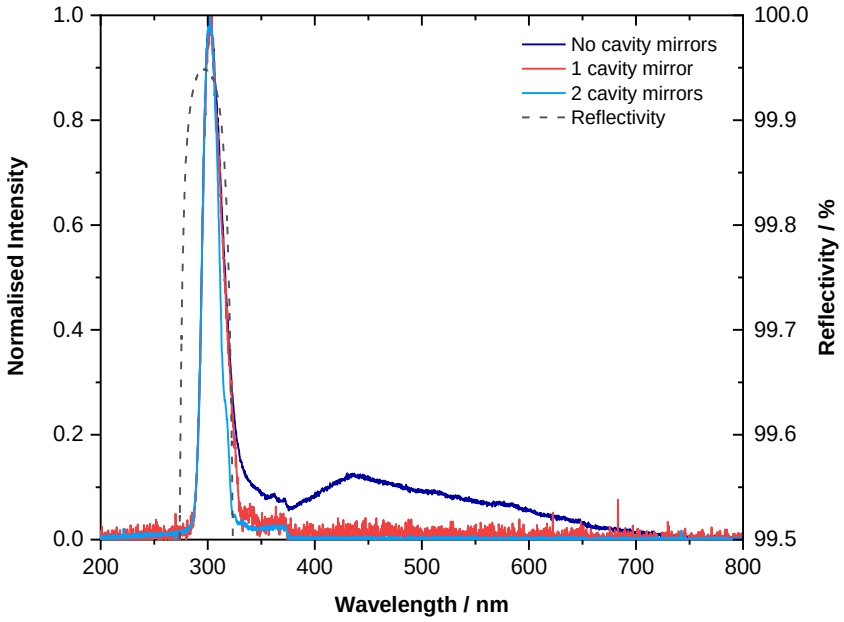

Figure 32 Spectral output obtained for different configurations of cavity mirrors when employed as reflective spectral filters. Also indicated here are the LED output without spectral filtering and reflectivity curve of cavity mirrors for reference. The LED emission spectrum was measured at an integration time of 9 s and the spectra with one and two cavity mirrors were measured at an integration time of 10 s. The noise seen in the normalised spectrum of one cavity mirror is due to the experimental error of coupling light into the spectrometer.

Configuration	FWHM / nm
Without cavity mirrors	22.2
1-cavity mirror	21.2
2-cavity mirrors	17.2

Table 3 Bandwidths obtained for the different configurations of cavity mirrors as spectral filters. The full width at half maximum (FWHM) were determined by measuring the width of the spectrum at half height.

From Table 3, it is seen that by using a pair of cavity mirrors the bandwidth reduced by only about 5 nm from 22.2 nm to 17.2 nm. Also from Figure 32, it is seen that in spite of using two cavity mirrors as reflective spectral filters some undesired light in the range between

320 – 380 nm (beyond the high reflectivity range of cavity mirrors) that will saturate the detectors for absorption measurements is still present. Thus requiring other approaches for spectral filtering to get rid of the light with an undesirable spectral characteristic with respect to this project work. The two possible options for spectral filtering in view of this project include employing:

1. Optical filters, or
2. Monochromator

To help determine the best approach for spectral filtering among these options, simulations were carried out that are discussed in further detail in this chapter in sections 4.3.1 and 4.3.2 for optical filters and monochromator respectively.

4.3 Simulations of the Optical Cavity Response

Generally CRDS uses a laser light source which by its definition is narrow bandwidth, typically not more than 1 – 100 GHz and hence one would not worry about the change in mirror reflectivity across the spectrum. But in the case of an LED the bandwidth is of the order of 10 – 100 THz and CEAS is typically carried out with a detection system that allows spectral resolution i.e., using a spectrometer as a detector. However, in this project a detector is chosen that does not spectrally resolve the light from the optical cavity but indiscriminately integrates all its wavelengths. Due to this unique approach (and acetone being a broad absorber), one needs to consider the spectral characteristics of the light source along with the spectral characteristics of the optical cavity and the detector. Engeln et al. [94] showed that when light from a narrowband CW laser in incident on an optical cavity, the intensity of light transmitted through the cavity at steady-state is directly proportional to the cavity's ring-down time. Similarly, for an optical cavity pumped with a broadband light source, each wavelength attains its own steady-state intensity within the cavity that is dependent on the intensity of the light source and the various loss processes occurring within the cavity (where the latter is related to the ring-down time). In BBCEAS the cavity output is a time integrated spectrum of the steady-state intensities transmitted by the cavity [40] and hence the optical cavity response is analysed in terms of ring-down times (RDTs) of the wavelengths of light coupling into the cavity. Thus, the optical cavity response in terms of RDTs helps to analyse the effect of the superposition of all the wavelengths that are incident on the optical cavity. From the discussions seen earlier in section 4.2, the characterisation of the 300 nm LED shows the presence of undesirable

wavelengths of light that can affect detection during absorption measurements of acetone. Therefore, simulations were carried out to determine the ring-down times with the 300 nm LED over its broad spectral output range. These simulations help determine a suitable spectral filtering approach to suppress the undesirable wavelengths of light. In addition to these, the simulations help determine the wavelength range that can achieve a low limit of detection for the acetone absorption measurements. Since these simulations give information on the optical cavity response, it also helps determine a suitable wavelength range to carry out pulsed-CRDS measurements in the future by operating the LED in pulsed-mode.

4.3.1 Simulations with Optical Filter

One of the options to suppress the undesirable wavelengths of light is the use of an optical filter that can be easily integrated into the beam path in comparison to a monochromator. This could be achieved by using a custom filter made for a specific spectral window or by using a pair of two edge filters (one long-pass and one short-pass). However, in the scenario of the LED requiring replacement, the new LED is likely to have its spectral output that no longer overlaps with the custom filters, thus, adding to the amount of time and cost spent on the experimental set-up. Compatibilities of off-the-shelf filters were checked with respect to spectral filtering required for this project. Simulations were carried out over the broad spectral output range of the LED considering the use of an off-the-shelf optical filter such as FF01-302/10-25, Semrock, that closely matched the requirements of this project. The transmission curve (as provided by the manufacturer) of this single-band bandpass filter used in the simulations is as shown in Appendix A.6 with average transmission of >45 % in the wavelength range 297 – 307 nm centred about 302 nm which is the range of interest. The intensities of light in the broad spectral output range of the LED were obtained by measuring the spectral output of the LED at its maximum driving current. The empty cavity RDT (τ_0) was calculated using Equation 9 with a cavity length set to d = 50 cm and reflectivity $R(\lambda)$ obtained from the reflectivity curve of the cavity mirrors (from Figure A. 6 (a)). The RDT (τ) in the presence of an absorbing species was calculated using Equation 11 considering 1 ppmv of acetone. The absorption cross-sections of acetone were obtained from the MPI-Mainz UV/VIS spectral Atlas [9]. The RDTs were calculated at all wavelengths in the output range of the LED and cavity output intensities I were calculated at each wavelength using the relation,

$$I = I_0 \exp(-t/\tau) \quad (18)$$

where I_0 was obtained via convolution of the incident LED intensity, transmissions of the cavity mirrors and that of the optical filter. The integrated intensities over the entire wavelength range were then plotted as a function of time and fitted with a single exponential decay equation given by,

$$y = A \exp(-t/\tau) + y_0 \quad (19)$$

where y_0 is offset to zero, A, t and τ are the amplitude, time and the RDT respectively.

(a)

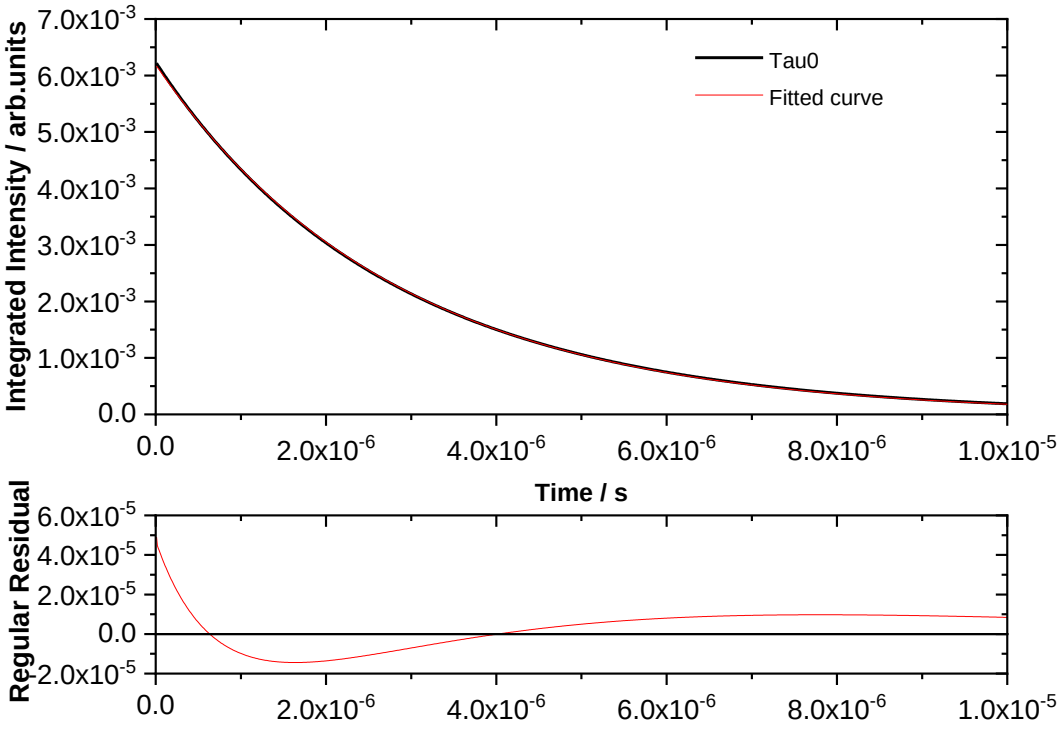

(b)

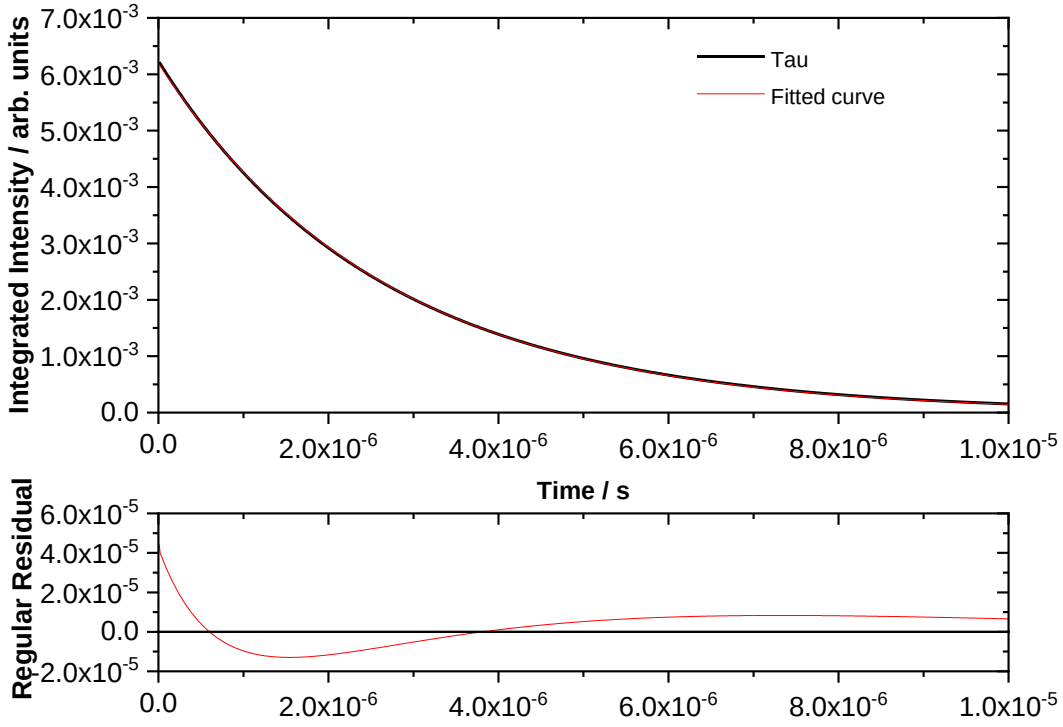

Figure 33 Simulations of the optical cavity response in the wavelength range 200 – 800 nm with the optical filter FF01-302/10-25, Semrock . (a) and (b) simulated plots of integrated intensity as a function of time for τ_0 and τ respectively fitted with a single-exponential. The regular residuals obtained for the fitted single exponential model are indicated at the bottom of each plot.

From the fits shown in Figure 33 (a) and (b) it was found that,

$$\tau_0 = 2.83 \text{ x } 10^{-6} \text{ s}$$

$$\tau = 2.67 \text{ x } 10^{-6} \text{ s}$$

with difference in their RDTs = 1.6 x 10^{-7} s. The intensity value at time zero was excluded in the plots to obtain a better fit. From the regular residuals obtained for single exponential fits it is clearly observed that the residuals and the integrated intensities differ by two orders of magnitude. From the fits and the residuals it can be concluded that single exponential decay is not the appropriate model for the cavity output in the scenario of using this off-the-shelf optical filter. This also implies that the output is a non-exponential decay. This is because the optical filter does not suppress the undesired light beyond its cut-off wavelength of 307 nm

efficiently. The data was further treated with a double-exponential model to check if there are two distinct time components (fast and slow) that can be correctly captured by a double-exponential fit. Several configurations were tested by either keeping certain parameters fixed or as floating. In Equation 20, the first part represents the fast decay corresponding to the wavelengths beyond the high reflectivity range of the cavity mirrors while the second part represents the slow decay corresponding to wavelengths of high reflectivity range.

$$y = A_1 \exp(-t/\tau_1) + A_2 \exp(-t/\tau_2) + y_0 \quad (20)$$

Various configurations of parameter values resulted in fits with residuals differing from their integrated intensities by one to three orders of magnitude and none providing the best fit (one such example is shown in Figure 34 (a) and (b) for τ_0 and τ respectively). Thus implying that there are no two distinct time components that can be fitted with a double-exponential and the characteristic is truly non-exponential rather than a double-exponential.

In conclusion, an off-the-shelf optical filter, such as FF01-302/10-25, Semrock discussed here is not a suitable option for this optical cavity set-up. This requires the use of two optical filters typically combining two edge filters, one long-pass and one short-pass filter or a custom-made filter for use with the chosen LED. But as already mentioned, if the current LED needs to be replaced, the new LED is likely to have a different spectral output. A slight change in the spectral characteristics of the LED would not cause an issue for acetone detection, however the LED emission spectrum may no longer overlap with the custom filter and this will result in further expense into making new custom-made optical filters. Thus adding to the overall cost and time spent on the experimental set-up.

(a)

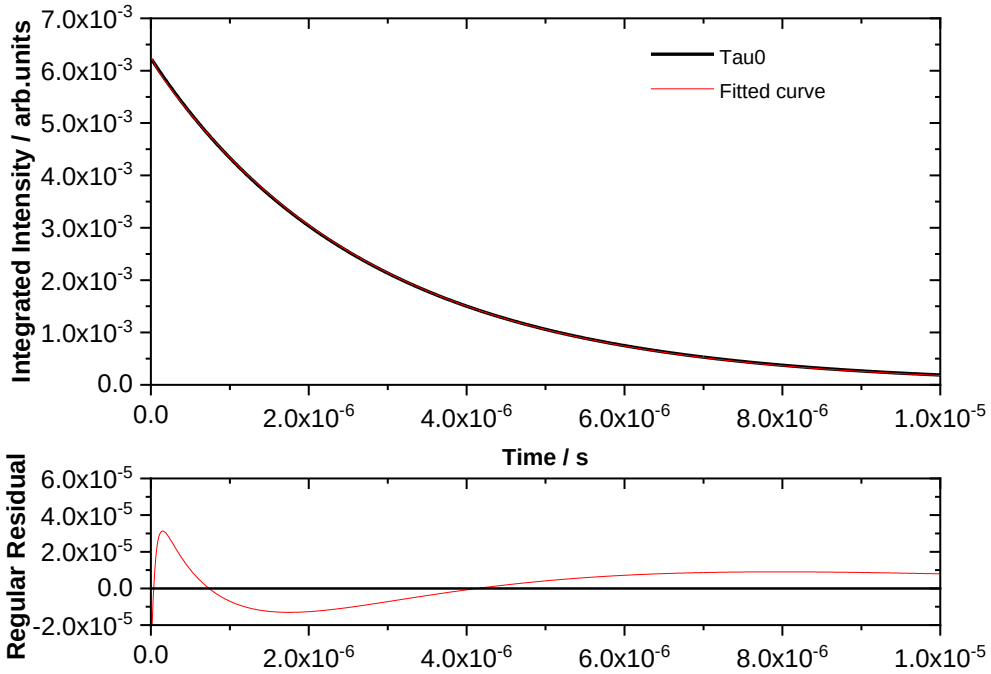

(b)

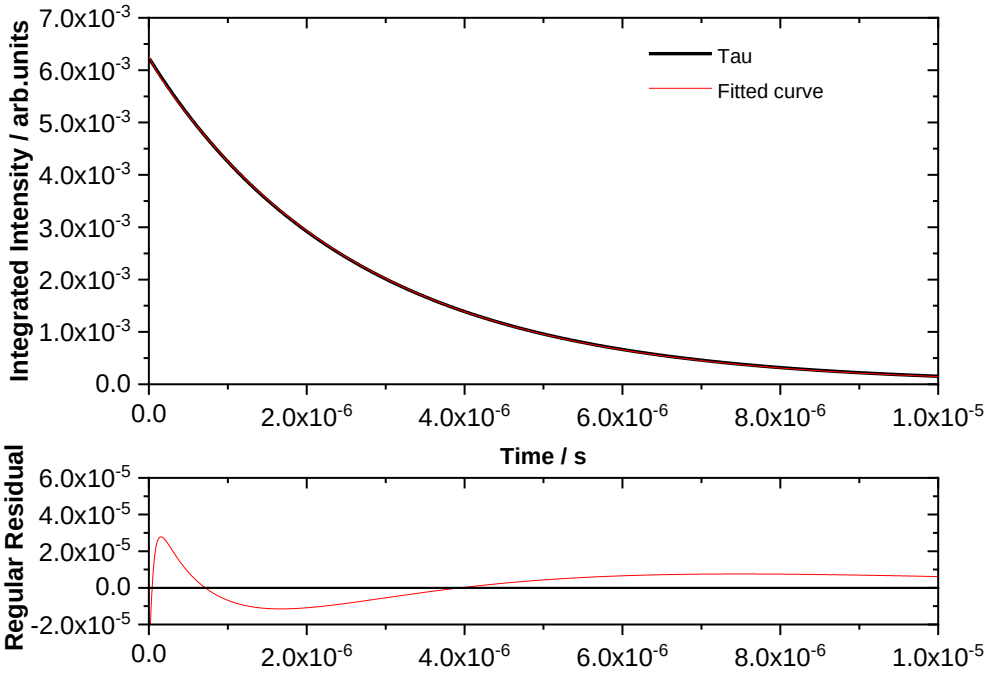

Figure 34 Simulations of the optical cavity response in the wavelength range 200 – 800 nm with the optical filter FF01-302/10-25, Semrock . (a) and (b) simulated plots of integrated intensity as a function of time for τ_0 and τ respectively fitted with a double-exponential. The regular residuals obtained for the fitted double-exponential model are indicated at the bottom of each plot.

4.3.2 Simulations with Monochromator

A monochromator may provide an alternative to optical filters. In general, monochromators are more versatile with respect to the spectral range that can be chosen and often also with respect to the bandwidth by adjusting the slit width. In comparison to an optical filter, monochromators generally have a lower transmission and are more challenging to set up in an optical beam path. In this section the simulations are carried out considering a monochromator with a spectral resolution of 2.2 nm and 4.4 nm that can be achieved by using appropriate slit sets on the monochromator. The values of τ_0, τ and integrated intensities are determined as reported earlier in section 4.3.1. The results obtained for simulations for spectral resolutions of 2.2 nm and 4.4 nm are discussed in the following sections.

4.3.2.1 2.2 nm Spectral Resolution

Considering a monochromator with a spectral resolution of 2.2 nm, the wavelength ranges simulated were (a) 293.9 – 296.1 nm, roughly near the wavelength of maximum acetone absorption within the LED spectral output range; (b) 295.9 – 298.1 nm, about the wavelength of maximum reflectivity of the cavity mirrors, and (c) 298.9 – 301.1 nm, near the maximum LED output intensity.

Tau0:

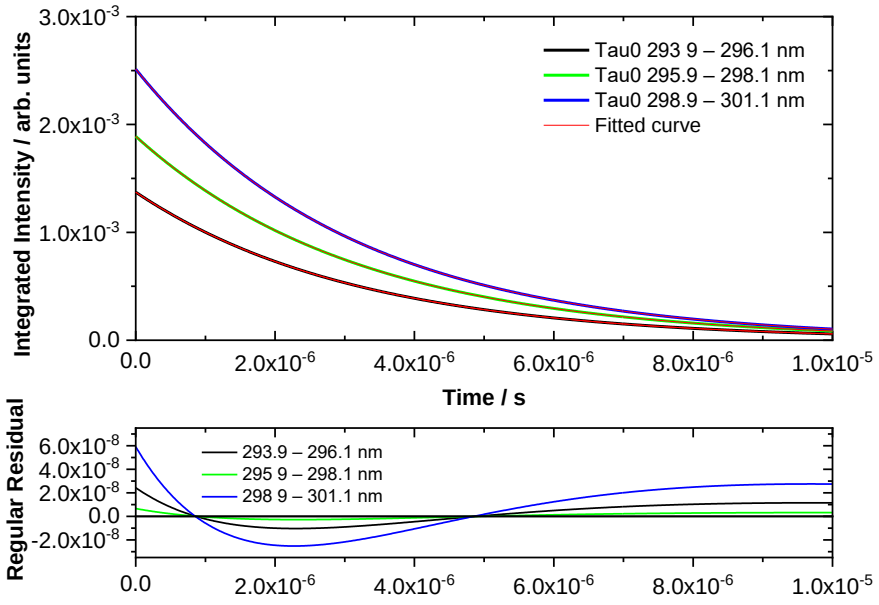

Figure 35 Simulated integrated intensities plotted against time obtained for a monochromator with a spectral resolution of 2.2 nm. Single-exponential fits and their corresponding regular residuals for an empty cavity are shown for the different wavelength ranges.

Tau:

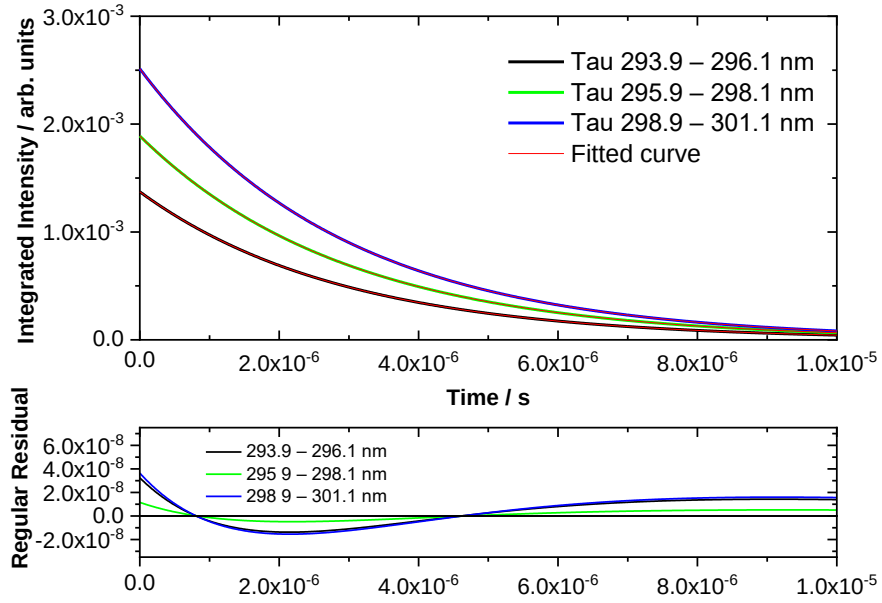

Figure 36 Simulated integrated intensities plotted against time obtained for a monochromator with a spectral resolution 2.2 nm. Single-exponential fits and their corresponding regular residuals corresponding to τ are shown for the different wavelength ranges.

Wavelength range / nm		RDT / 10^{-6} s	$\Delta\tau$ / 10^{-7} s	Acetone Absorption Probability / 10^{-28} arb.units.s.cm^2.nm	Residual Sum of Squares
293.9 – 296.1	τ_0	3.17	2.6	3.1	7.4 x 10^{-14}
	τ	2.91			1.3 x 10^{-13}
295.9 – 298.1	τ_0	3.23	2.5	3.9	5.5 x 10^{-15}
	τ	2.98			1.6 x 10^{-14}
298.9 – 301.1	τ_0	3.14	2.1	4.4	4.4 x 10^{-13}
	τ	2.93			1.6 x 10^{-13}

Table 4 Simulated values obtained for ring-down times and change in RDTs for different wavelength ranges using a monochromator with a spectral resolution of 2.2 nm.

From Figure 35 and Figure 36 it is seen that the residuals are smaller by five orders of magnitude and from the residual sum of squares it is observed that a single exponential fit is an acceptable model for the simulated cavity output obtained for a wavelength resolution of 2.2 nm. In Table 4, considering all the simulated wavelength ranges there is no drastic change in their RDTs. The acetone absorption probability obtained from convolution of the areas under the integrated intensity exponential decay curves for τ and the acetone absorption cross-section curve shows that 298.9 – 301.1 nm wavelength range has high acetone absorption probability than the other wavelength ranges. Overall, these simulations imply that absorption measurements are feasible using a monochromator with a spectral resolution of 2.2 nm and the broadband absorber (acetone) with a typical set of CRD mirrors.

4.3.2.2 4.4 nm Spectral Resolution

Considering a monochromator with a spectral resolution of 4.4 nm, a few wavelength ranges were simulated as shown in Figure 37 and Figure 39. An additional wavelength range 302.8 – 307.2 nm around which the reflectivity of the cavity mirrors starts to fall is also included for comparison with the other wavelength ranges.

Tau0:

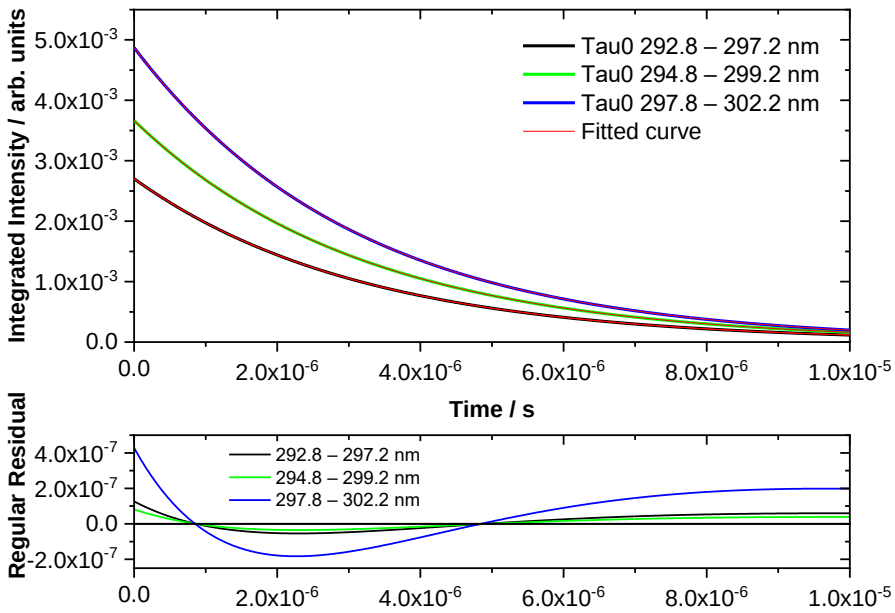

Figure 37 Simulated integrated intensities plotted against time obtained for a monochromator with a spectral resolution 4.4 nm. Single-exponential fits and their corresponding regular residuals corresponding to τ_0 are shown for the different wavelength ranges.

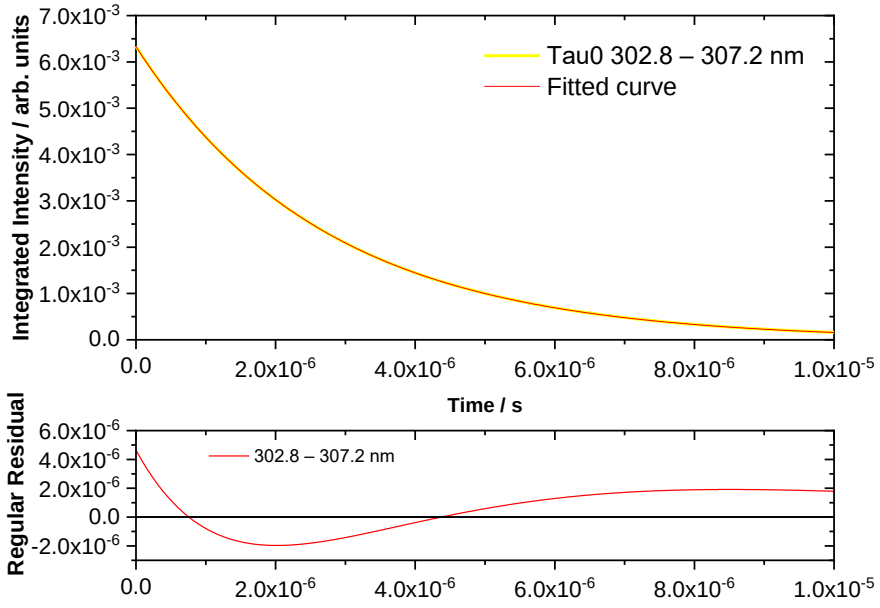

Figure 38 Simulated integrated intensities for τ_0 plotted against time for the wavelength range 302.8 – 307.2 nm (in the region where the reflectivity of the cavity mirrors begins to fall). The fitted curve and its corresponding regular residual for the wavelength range are shown. This plot is used to compare with the other wavelength ranges shown in Figure 37.

Tau:

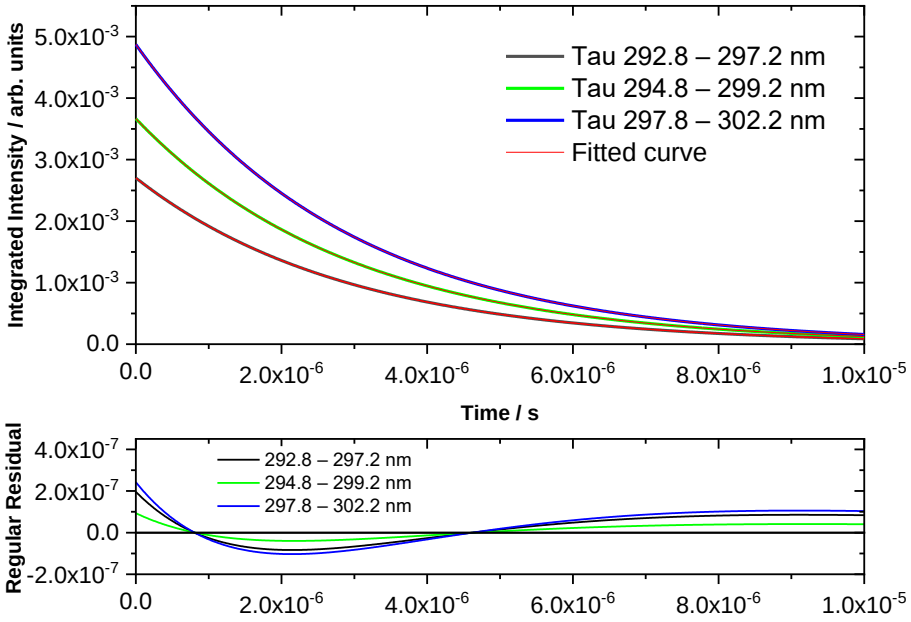

Figure 39 Simulated integrated intensities plotted against time obtained for a monochromator with a spectral resolution 4.4 nm. Single-exponential fits and their corresponding regular residuals corresponding to τ are shown for the different wavelength ranges.

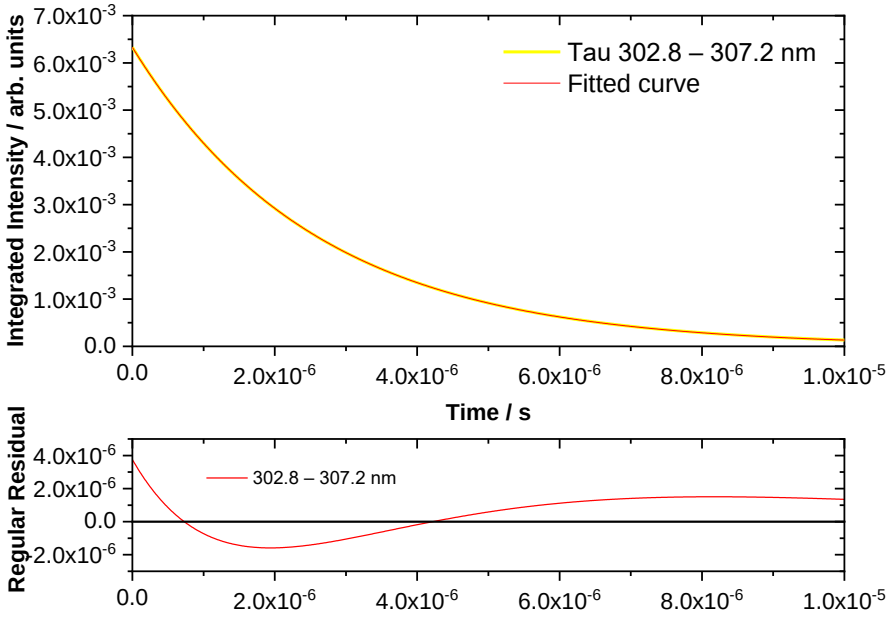

Figure 40 Simulated integrated intensities for τ plotted against time for the wavelength range 302.8 – 307.2 nm (in the region where the reflectivity of the cavity mirrors begins to fall). The fitted curve and its corresponding regular residual for the wavelength range are shown. This plot is used to compare with the other wavelength ranges shown in Figure 39.

Wavelength range / nm		RDT / 10^{-6} s	$\Delta\tau$ / 10^{-7} s	Acetone Absorption Probability / 10^{-27} arb.units.s.cm^2.nm	Residual Sum of Squares
292.8 – 297.2	τ_0	3.18	2.6	1.20	1.2 x 10^{-12}
	τ	2.92			2.8 x 10^{-12}
294.8 – 299.2	τ_0	3.20	2.4	1.51	5.9 x 10^{-13}
	τ	2.96			7.2 x 10^{-13}
297.8 – 302.2	τ_0	3.12	2.0	1.72	1.2 x 10^{-11}
	τ	2.92			4.0 x 10^{-12}
302.8 – 307.2	τ_0	2.71	1.1	1.52	1.3 x 10^{-9}
	τ	2.59			8.5 x 10^{-10}

Table 5 Simulated values obtained for ring-down times and change in RDTs for different wavelength ranges using a monochromator with a spectral resolution of 4.4 nm.

From Figure 37 and Figure 39 it is observed that the residuals are smaller by four to five orders of magnitude for lower wavelength ranges and hence are not very dissimilar to the case of a monochromator with a spectral resolution 2.2 nm discussed in section 4.3.2.1. From the residual sum of squares shown in Table 5, it is seen that a single exponential fit is an acceptable model for the optical cavity response obtained by employing a monochromator with a spectral resolution of about 4.4 nm. A large change in RDT is observed for the wavelength ranges of 292.8 – 297.2 nm and 294.8 – 299.2 nm corresponding to the regions of maximum reflectivity. The wavelength range 302.8 – 307.2 nm was simulated to show the effect of a drastic change in mirror reflectivity on its RDT. In Figure 38 and Figure 40, it is observed that the residuals are smaller by three orders of magnitude and the residual sum of squares (in Table 5) are greater by about two to four orders of magnitude in comparison to the other wavelength ranges. The wavelength range of 302.8 – 307.2 nm has a smaller change in RDT in comparison to the other wavelength ranges (see Table 5) as the reflectivity begins to fall in this range. While the ring-down time is appreciable in this wavelength range, potentially leading to a low limit of detection of acetone, the poor decay characteristics introduce a rather large error into any ring-down fit. The acetone absorption probability was determined by convolution of the areas under the integrated intensity exponential decay curves for τ and the acetone absorption cross-section curve for the different wavelength ranges. Although a larger change in RDT is observed in the wavelength range of 292.8 – 297.2 nm, the acetone

absorption probability is the lowest for this range. This is mainly because less light is available in this wavelength range which is evident from the area under its corresponding intensity curve. The wavelength range of 297.8 – 302.2 nm has higher acetone absorption probability (as seen in Table 5) in comparison to other wavelength ranges because the area under its integrated intensity curve is larger in comparison to the lower wavelength ranges. This indicates more light is available to interact with the acetone molecules. In addition to this, the residual is low and well-behaved in this wavelength range making for reliable ring-down fits with low errors as seen from its corresponding residual sum of squares. The combination of high mirror reflectivity in this wavelength range leading to a large change in RDTs and the residuals being smaller by four to five orders of magnitude and with more light available in the wavelength range of 297.8 – 302.2 nm results in a low limit of detection of acetone. Also, in future CRDS and LIF measurements of acetone should be feasible in this wavelength range.

In conclusion, the comparison between optical filters and a monochromator to spectrally filter the LED in this project points to a better suitability of the monochromator. The tunability of the spectrum easily available with the monochromator provides a clear advantage. In addition, a straightforward choice of spectral bandwidth by changing the slit widths can shape the cavity ring-down characteristics to the needs of the measurements. Moreover, the ability of employing the same monochromator with an LED centred around a different wavelength is an advantage in comparison to using custom-made optical filters.

4.4 Q-Factor for IBBCEAS

In IBBCEAS, placing two plano-concave dielectric coated mirrors into the optical path around the sample greatly enhances the sensitivity in comparison to conventional single-pass absorption measurements. Thus the enhancement factor or the Q-factor describes the enhancement of the signal-to-noise ratio (SNR) of the absorption coefficient determined by IBBCEAS in comparison to single-pass absorption measurements [77]. In order to simulate IBBCEAS for an optical cavity of length 50 cm using the 300 nm LED and cavity mirrors used in this project the Q-factor was determined using the relation [77],

$$Q = \frac{(1 - R - A)[1 + (1 - L)^2 R^2]}{\sqrt{[1 - (1 - L)^2 R^2]^3}} \quad (21)$$

where R, T and A are the mirror reflectivity, transmission and absorption of the cavity mirrors, respectively. Any losses in the cavity are summarised in L. The commonly used approximation $T = (1 - R)$ does not hold in the UV where a significant amount of light is absorbed or scattered at the mirror surfaces and coatings. Therefore, the correct expression to be used here is $T = (1 - R - A)$. In the simulations, the term $(1 - R - A)$ was substituted with the values of T as provided by the manufacturer (Figure A. 6 (b)).

In this section, the Q-factor was estimated for Rayleigh scattering of N_2 (mean σ_{N_2} = 5.6 x 10^{-26} cm^2) and He (mean σ_{He} = 7.9 x 10^{-28} cm^2) at various pressures in the wavelength range 298 – 302 nm considering three different R values corresponding to its maximum (99.948 %), mean (99.947 %) and minimum (99.945 %) in this wavelength range as shown in Figure 41 (a) and (b). The trends in Figure 41 show the decreasing Q-factor with increasing losses which are more pronounced in N_2 than He Rayleigh scattering. It is observed that for a given loss, the Q-factor increases as the reflectivity decreases due to an increase in the value of T. Overall, IBBCEAS in this set-up enhances Rayleigh scattering measurements by at least a factor of 13 in comparison to a single-pass experiment with typical absorption co-efficients of the order of 10^{-7} cm^{-1} and 10^{-9} cm^{-1} for N_2 and He respectively.

(a)

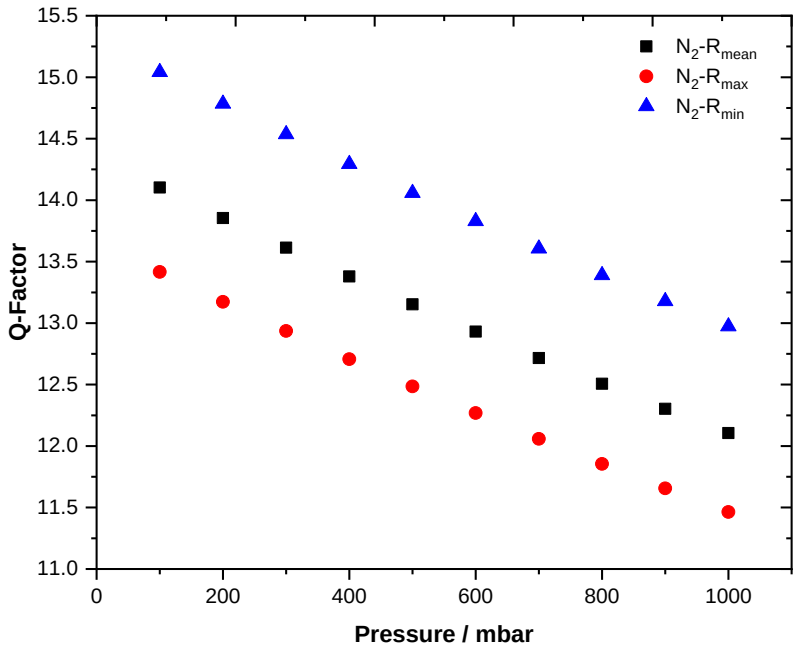

(b)

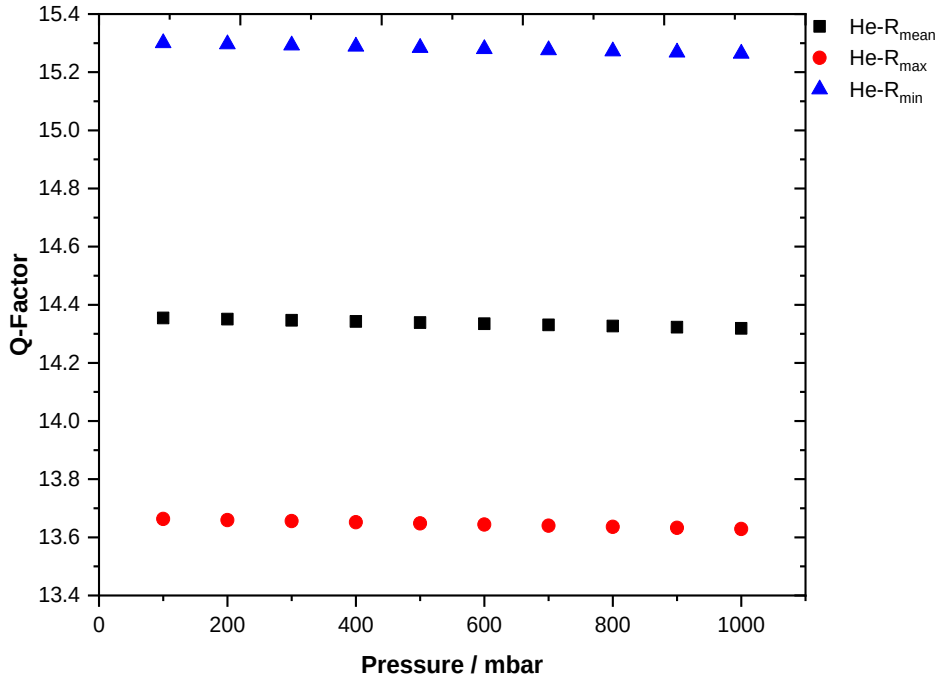

Figure 41 Q-factors estimated for Rayleigh scattering of calibration gases (a) N_2 and (b) He, at various pressures and at different reflectivity (R) values corresponding to its maximum (99.948 %), mean (99.947 %) and minimum (99.945 %) in the wavelength range 298 – 302 nm. In these calculations, losses L at varying pressures were determined considering a cavity length of 50 cm and substituting transmission of the cavity mirror $T = (1 - R - A)$ in Equation 21.

Likewise, Q-factors were also determined for IBBCEAS with acetone using Equation 21 for various partial concentrations of acetone. In Figure 42, it is seen that the Q-factor remains almost a constant for very low losses and begins to decrease around losses of the order of 10^{-5} equivalent to acetone concentrations of 1 ppmv. This clearly shows that towards very low concentrations of a species a multi-pass measurement is greatly enhanced compared to a single-pass experiment.

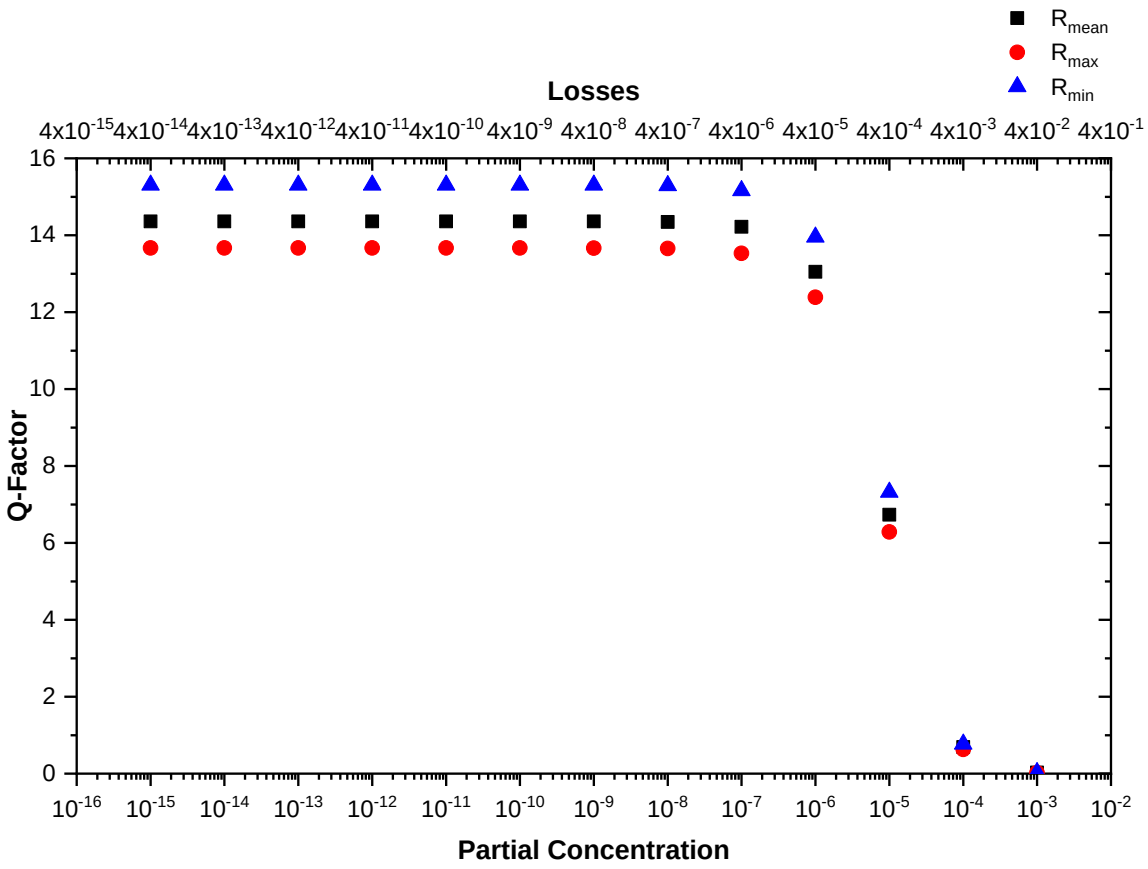

Figure 42 Q-factors for various partial concentrations of acetone calculated at different reflectivity (R) values corresponding to its maximum (99.948 %), mean (99.947 %) and minimum (99.945 %) in the wavelength range 298 – 302 nm. The losses L at varying concentrations of acetone were determined considering a cavity length of 50 cm and substituting transmission of the cavity mirror $T = (1 - R - A)$ in Equation 21. Mean absorption cross-section values for acetone in the wavelength range 298 – 302 nm were obtained from the works of W Schneider and G K Moortgat (1987) at 294 K 196.6 – 365.4 nm (0.1 nm) in the MPI-Mainz UV/VIS spectral Atlas [9].

Assuming $L \rightarrow 0$ and $R \rightarrow 1$ therefore, $1 + R = 2$ (i.e., when losses are very small and reflectivity is very high), Equation 21 for maximum enhancement factor becomes,

$$Q_{max} = \frac{T}{\sqrt{2[1-R]^3}} \qquad (22)$$

Using reflectivity and transmission values of the cavity mirrors in this equation, Q_{max} can be obtained which is plotted against wavelength as shown in Figure 43. From this figure it is seen that the enhancement factor in the wavelegnth range of interest 298 – 302 nm has an average Q_{max} value of ~14.

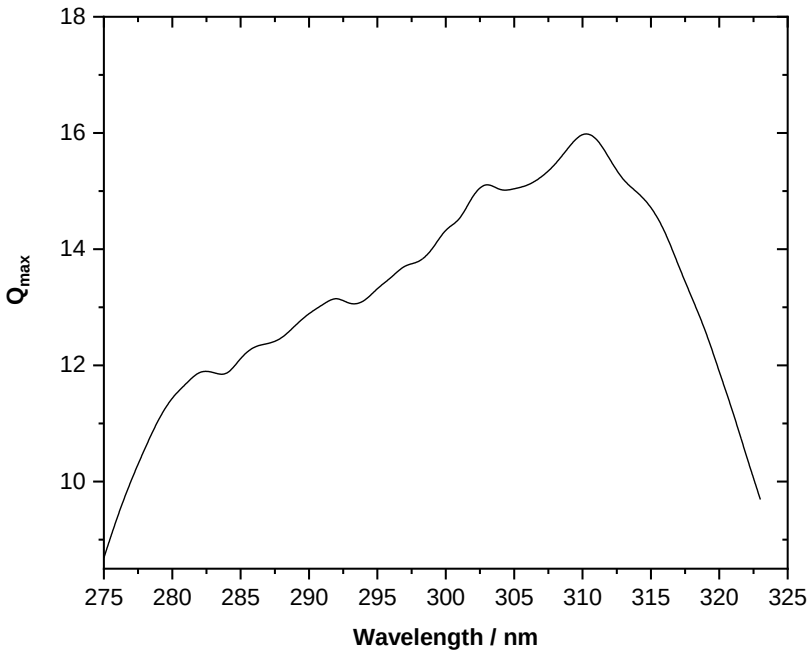

Figure 43 Q_{max} values at different wavelengths in the high reflectivity range of cavity mirrors used in the CEAS experimental set-up.

4.5 LED Optical Power

According to manufacturer specifications the M300L4 mounted LED has a minimum output power of 26 mW and typical output of ~32 mW when operated at its maximum driving current. Tests were carried out to determine the LED output optical power with the configuration of an aspheric lens and using the photodiode for measuring the output signal and the spectrometer to determine the spectral output. Knowing the responsivity of the photodiode at different wavelengths (see Figure A. 1) the optical output power of the LED was determined over its broad spectral output range. An optical power of 10.7 mW was measured which is ~33 % of the specified typical output power of the 300 nm LED.

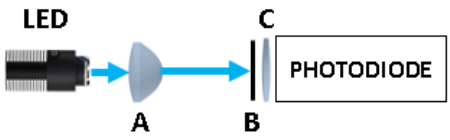

A	Aspheric lens (17.5 mm EFL, Ø25.0 mm)
B	Neutral density filters
C	Bi-convex lens (25 mm EFL, Ø25.4 mm)

Figure 44 Optical configuration used to determine the LED optical output power.

Optical power was also determined choosing different wavelength ranges using the 600 μm slit set on the monochromator (~4.4 nm resolution). The centre wavelengths were chosen in steps of 1 nm across the spectral output range of the LED. Figure 45 shows the normalised spectra recorded with the monochromator (resolution ~4.4 nm) at various wavelengths overlapped with the spectral output of the LED. This shows that a resulting spectrum with FWHM of ~4.4 nm can be achieved using the monochromator in comparison to the LED spectral output without spectral filtering which had a FWHM of 22.2 nm. The spectra from the monochromator also show that the undesirable wavelengths are successfully suppressed. After wavelength selection was carried out with the monochromator, the intensities were measured with the photodiode to determine the optical power. The spectra obtained with the monochromator centred around each wavelength were used to determine the weighted responsivity of the photodiode in order to calculate the optical powers as shown in Figure 46. From this figure, the wavelength integrated power is found to be ~0.3 mW.

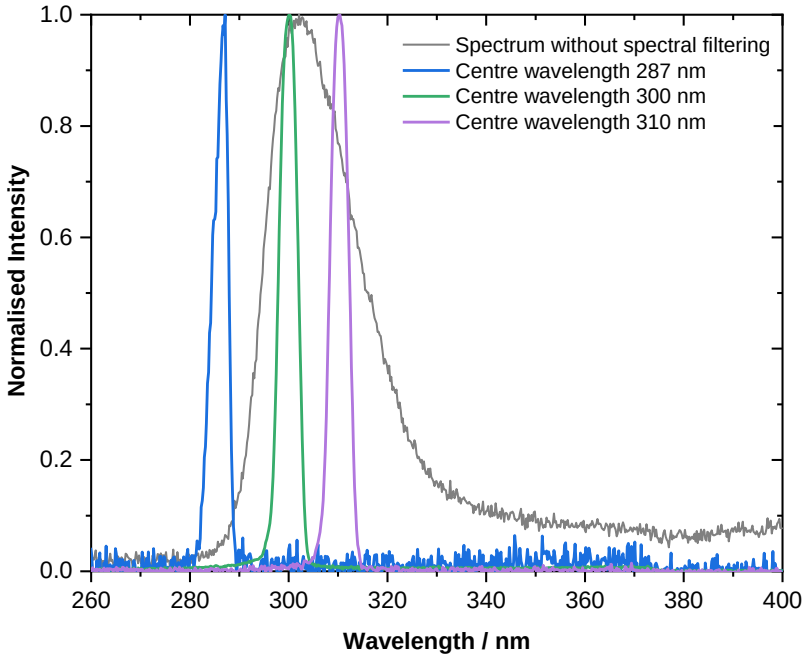

Figure 45 A few examples of normalised spectra obtained using the monochromator with a resolution of ~4.4 nm (600 μm slit set). The LED spectral output without spectral filtering (FWHM = 22.2 nm) is also overlapped for reference. The spectra were measured with the CCS200/M spectrometer.

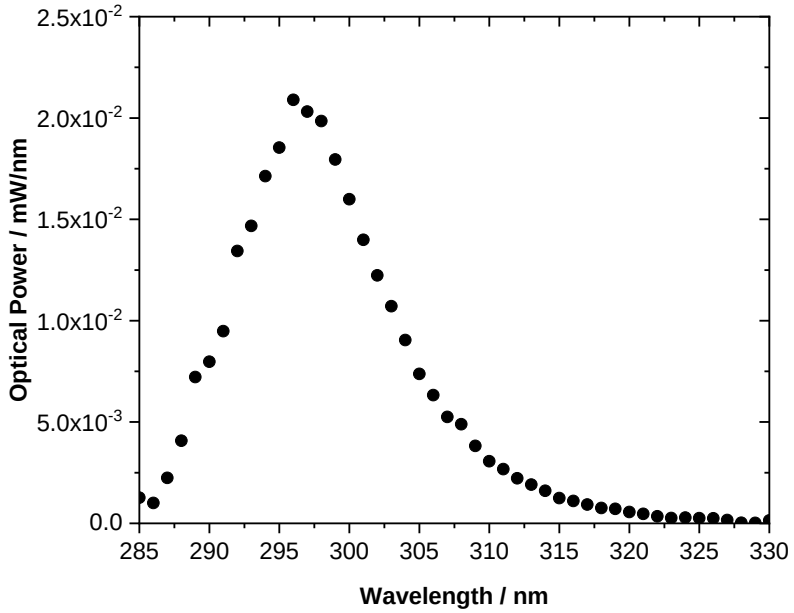

Figure 46 Optical power (mW/nm) as a function of wavelength. Wavelength selection at an interval of 1 nm was achieved with the monochromator fitted with 600 μm slit set with a resolution of ~4.4 nm. The wavelength integrated optical power is 0.3 mW.

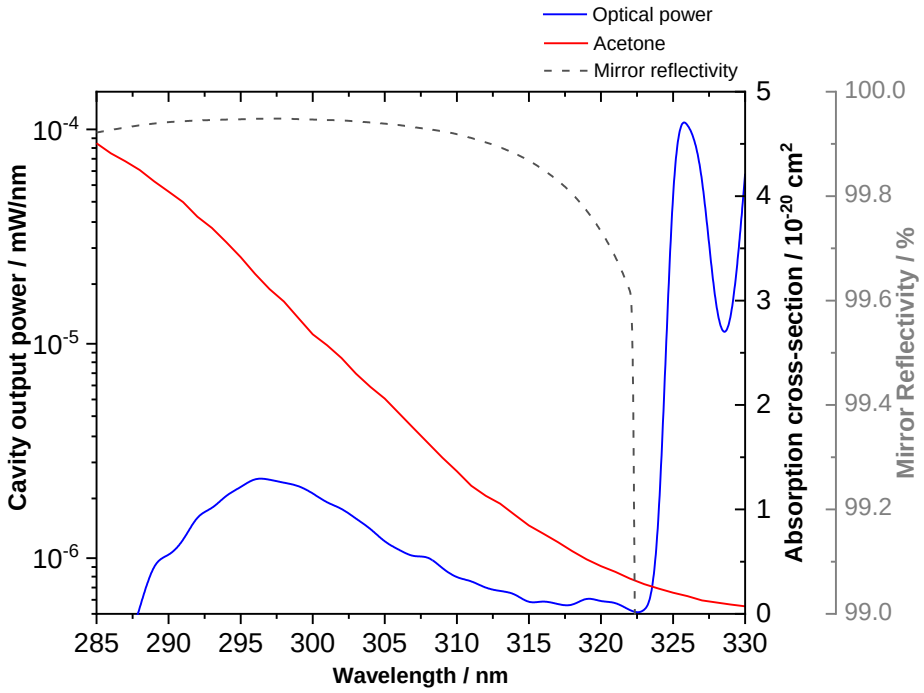

Figure 47 Simulated optical cavity output power (in mW/nm) is plotted as a function of wavelength superimposed on reflectivity curve of the cavity mirrors and acetone absorption cross-section. The simulations were carried out using the optical powers shown in Figure 46 and using the relation, Cavity output power = power x $(T/2)$, where T is the cavity mirror transmission.

To simulate the optical cavity response in terms of power, the power spectrum in Figure 46 was multiplied with the cavity transmission. This cavity output power is plotted as a function of wavelength which is superimposed on the acetone absorption cross-section and the mirror reflectivity curve (as shown in Figure 47). From Figure 47, it is seen that optical power is greatly reduced in the high reflectivity range of the cavity mirrors and beyond this range the optical power is higher due to the significant transmission of the mirrors in this range. Thus it can be concluded that it is essential to spectrally filter the LED output as otherwise a CEAS measurement is not possible.

4.6 Optics Tested for Light Coupling

LEDs are widely used in the visible wavelength range in lighting and spectroscopy. Many optical solutions are available for these LEDs to efficiently collimate and steer their light output. However, most of these optics are made of materials (BK-7, polycarbonate) that do not transmit UV light. Consequently, one of the big challenges in this project was to collimate and steer the light output of the 300 nm LED. The possibility of coupling light from the LED to an optical fiber (Ø200 μm fiber core size, BFL200HS02, Thorlabs) via a fiber optic collimator (#88181, Edmund Optics) and fiber refocusing assembly (#88185, Edmund Optics) was tested.

Figure 48 displays the output spectra obtained for various configurations of optical components with different numerical apertures employed for coupling light from the LED that has a numerical aperture of about 0.9 into an optical fiber with a numerical aperture of 0.22 (that is matched to the input of the spectrometer). A higher intensity (in the range of 300 nm) was observed for the configuration of an aspheric lens in combination with a 40 mm focal length plano-convex lens in comparison to other optical configurations. But overall the coupling efficiency of light from the LED into the fiber did not improve much. This could be further investigated in future to improve the coupling efficiency of LED light into an optical fiber as the light that comes out of the fiber could be much easier collimated and coupled into the optical cavity.

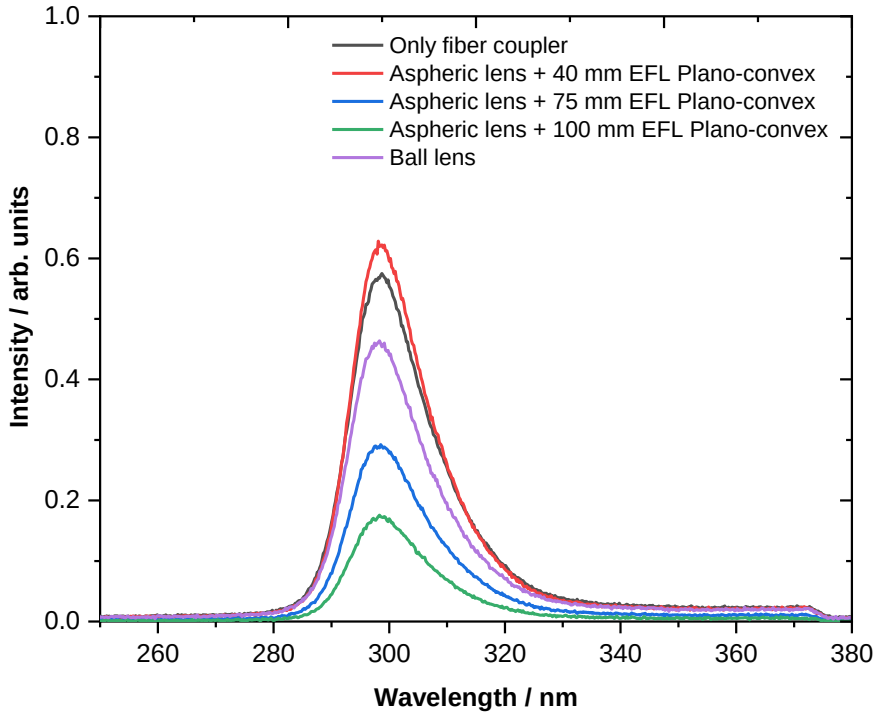

Figure 48 Output spectra obtained for various combinations of optics for coupling light from the LED to an optical fiber. In each set-up the following components were used: 300 nm LED → fiber coupler → Ø200 µm optical fiber → spectrometer. To improve the coupling efficiency, a selection of different optics (shown here) were used between the LED and the fiber coupler.

Among other optics, a 90° off-axis parabolic (OAP) mirror (model 50328AL, Ø38.1 mm, Newport Corporation) was tested as they produce a collimated beam from a point source without introducing spherical and chromatic aberrations. An optical set-up using an OAP mirror was tested in conjunction with the monochromator to spectrally filter and steer the light from the LED (Figure 49).

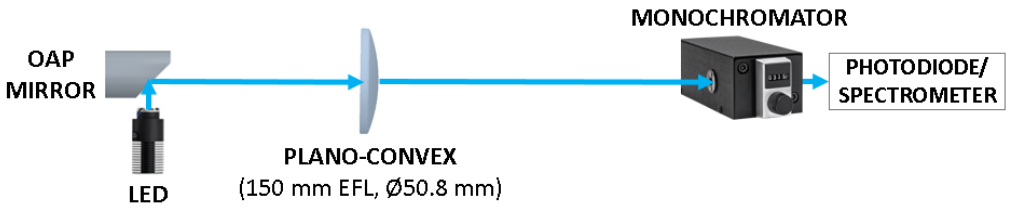

Figure 49 Optical set-up using an off-axis parabolic (OAP) mirror in conjunction with the monochromator.

Collimating light from the LED with an OAP mirror or an aspheric lens yielded overall similar light output power (Figure 50). The wavelength integrated power was found to be ~0.3 mW which agrees with that observed with an aspheric lens.

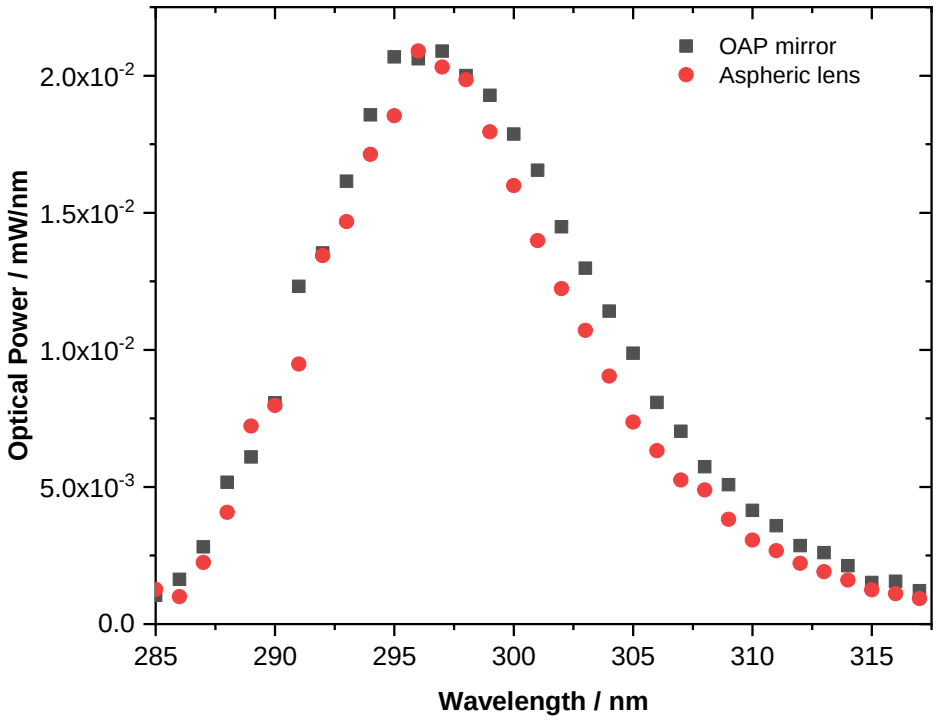

Figure 50 Comparison plot for optical powers obtained employing an OAP and an aspheric lens for collimating light from the LED.

4.7 Test Set-ups for Wavelength-Dependent Measurements

Collimation and steering of light from the LED present a great challenge and several set-ups were tried and evaluated for their suitability in an IBBCEAS set-up taking into account the divergence of the beam, the spectral composition and the transmitted optical power. Several set-ups with various combinations of optics were tried and tested to determine a reliable set-up for wavelength-dependent measurements using a spectrometer. They were aimed to obtain a set-up that would help achieve high optical coupling into an optical cavity. Also, as the inner diameter of the cavity in the experimental set-up was 16 mm, the beam spot size had to be within this limit at the entrance and the exit end for efficient coupling of light into the cavity without cutting off or becoming highly divergent within the cavity. In this section, some of the set-ups that fulfilled these criteria have been presented.

Optical Set-up	
1	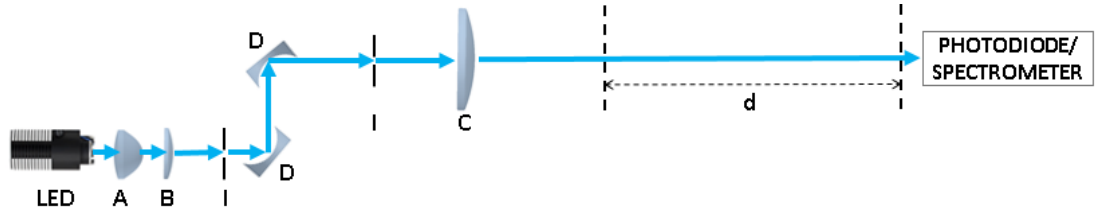
2	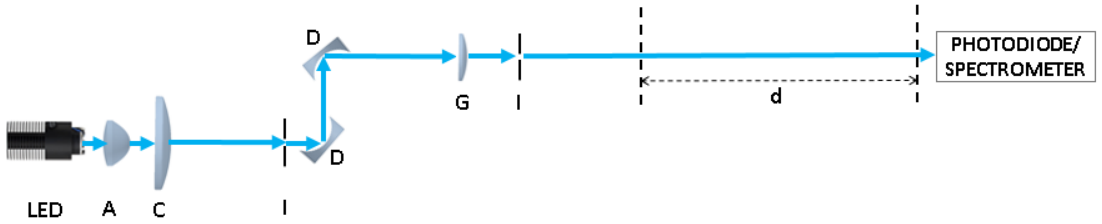
3a	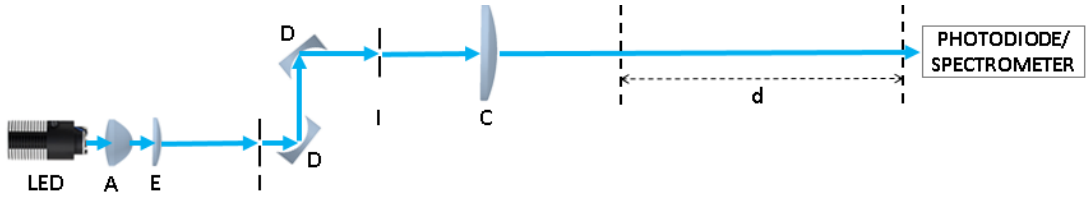
3b	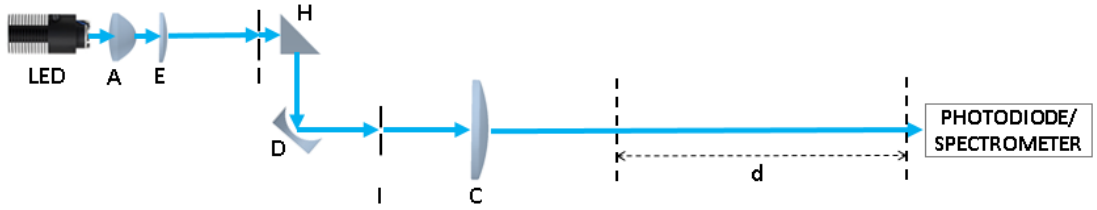
4	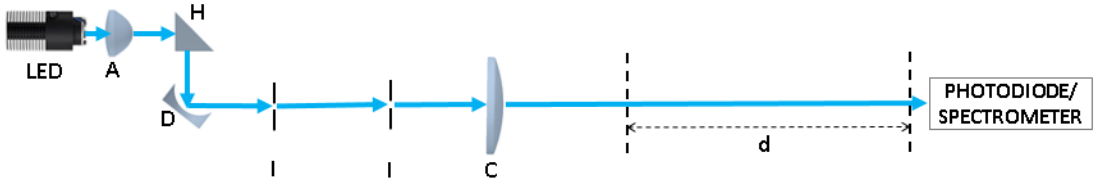
5	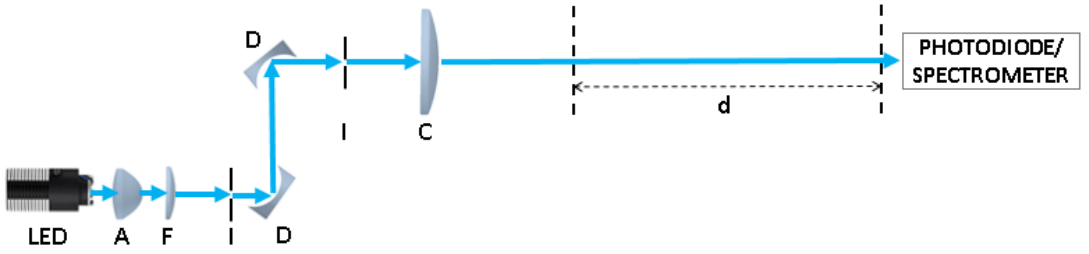

	Part		Part
A	Aspheric lens (17.5 mm EFL, Ø25 mm, 0.69 NA)	F	Plano-convex lens (50 mm EFL, Ø25.4 mm)
B	Plano-convex lens (75 mm EFL, Ø25.4 mm)	G	Plano-convex lens (200 mm EFL, Ø25.4 mm)
C	Plano-convex lens (150 mm EFL, Ø50.8 mm)	H	Prism
D	Cavity mirror	I	Iris
E	Plano-convex lens (100 mm EFL, Ø25.4 mm)	d	Cavity length ~450 mm

Figure 51 Set-ups tried and tested for wavelength-dependent measurements. A Bi-convex lens (25 mm EFL, Ø25.4 mm) is used to focus the light onto the photodiode to measure the output power of each set-up.

The test set-ups were mounted on an optical table assuming a cavity length of $d \approx 450$ mm (with no optical cavity). For comparison, optical powers (see Table 7) and spectra (see Figure 52) were measured for each of the tested set-ups shown in Figure 51 by operating the LED at its full optical output. FWHM were also determined for each as shown in Table 6.

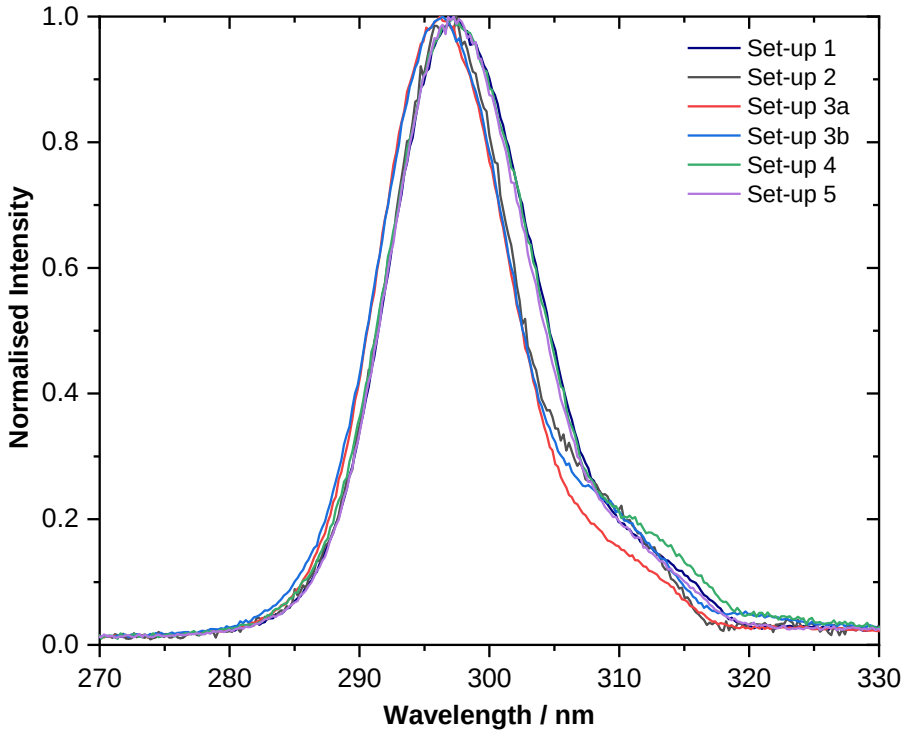

Figure 52 Normalised spectra obtained for the various test set-ups shown in Figure 51 for wavelength-dependent measurements.

Set-up	FWHM / nm
1	13.2
2	11.5
3a	12.0
3b	12.0
4	13.3
5	12.9

Table 6 FWHM obtained for the various test set-ups (displayed in Figure 51) for wavelength-dependent measurements.

Set-up	Optical Power / mW
1	0.189
2	0.034
3a	0.172
3b	0.161
4	0.109
5	0.179

Table 7 Optical powers obtained for the various test set-ups in Figure 51 for wavelength-dependent measurements.

The set-ups 1 and 5 which differ by the focal length of the lens used after the aspheric lens, vary by ~5 % in terms of their optical power. These set-ups have higher optical output powers in comparison to other set-ups as the lenses used after the aspheric lens have higher numerical aperture in comparison to the other set-ups. Thus capturing more light exiting the aspheric lens. However, it is observed that set-up 5 that uses the 50 mm focal length plano-convex lens formed a sharper focus (at iris 1 position) and the light became highly divergent along the beam path. Consequently, in order to control the beam spot size the aperture of the iris after this lens had to be further reduced. Whereas in the case of the 75 mm focal length plano-convex lens, the aperture of the iris was further increased as the beam was not too divergent along the beam path. Thus resulting in a higher optical power in comparison to the other set-ups. However, it is observed that set-up 1 has a FWHM of 13.2 nm, which is not desirable, caused by the

alignments of the cavity mirrors used for spectral filtering. Although set-up 2 has the narrowest FWHM, its corresponding optical output power is the lowest among the other optical set-ups. This is because the aperture of the iris placed after the 150 mm plano-convex lens (Ø50.8 mm) had to be reduced a lot in order to make the beam spot size fit within the diameter of 16 mm at the entrance and the exit end positions of the cavity. Therefore, based on this analysis, set-up 1 is most suitable and hence chosen for testing a wavelength dependent measurement using the spectrometer for wavelength selection at the output end of the optical cavity.

In the optical set-ups evaluated in Figure 51, the output from the LED is slightly spectrally filtered using the cavity mirrors along the beam path to steer the beam. However, in Figure 52, the spectra obtained for these set-ups show an appreciable amount of light at longer wavelengths. This light will have a high transmission through the optical cavity as the mirrors have a low reflectivity beyond 310 nm (Figure 53). Therefore, wavelength selection will be required on the detection side using a spectrometer. In order to test this, as set-up 1 had higher optical output in comparison to other test set-ups seen earlier in Table 7, an open cavity ($d \approx 370$ mm) was set-up on the optical table and spectra were measured behind the rear cavity mirror. For spectral comparison, the spectra were measured at first by placing the rear cavity mirror only, followed by placing the front cavity mirror forming an optical cavity. During the process of optimisation of the optical alignment, intensity fluctuations were observed in the wavelength range around 300 nm and the intensity of light was very weak in this range (see Figure 53) which made it difficult to optimise the cavity. A noisy and weak intensity spectrum for cavity response was observed as shown in Figure 53. The observed intensity fluctuations in the spectrum were due to variation of spatial composition over the integration time (10 s) of the spectrum. The spectrometer was set to its highest sensitivity which turned out to be insufficient to carry out an IBBCEAS measurement in the region of interest. Thus, a potential issue caused by the low output power of the LED in terms of sensitivity was observed in the desired wavelength range (highlighted area in Figure 53). And this was further complicated by the rather insensitive spectrometer used in this project. Thus, wavelength-dependent measurements with this spectrometer were not feasible. This set-up should be feasible with better light coupling into the optical cavity in the future.

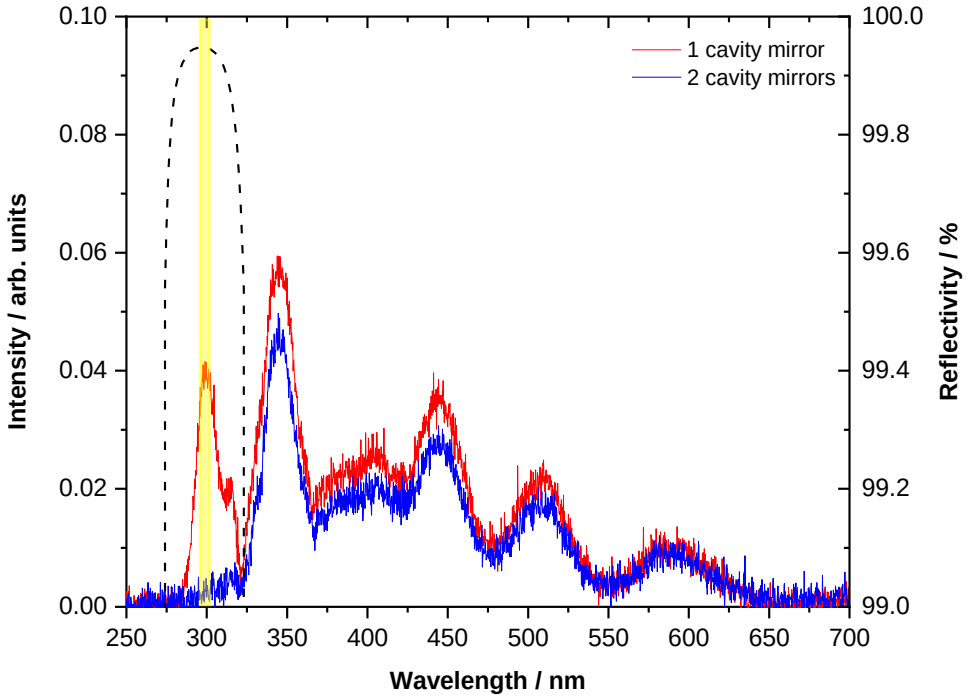

Figure 53 Spectra as obtained from the spectrometer for one cavity mirror and two cavity mirrors of the open cavity (for set-up 1) over an integration time of 10 s. The reflectivity of the cavity mirrors is shown for reference (as dashed lines). The yellow highlighted area represents the wavelength range of interest 298 – 302 nm.

4.8 Monochromator Output

As seen from section 4.7, the spectrometer is not sensitive enough to carry out IBBCEAS measurements by wavelength selection on the detection side of the set-up. Therefore, the alternative is to spectrally filter the LED output prior to the cavity using a monochromator and then use the much more sensitive photodiode to detect the spectrally integrated cavity output.

The light exiting the monochromator is expected to have a certain numerical aperture (NA), from where one would use a suitable lens to collimate the beam and couple it into the cavity. However, it was observed that the light exiting the slit became highly divergent in one-direction implying a different NA in this direction in comparison to the other. This posed a challenge for coupling LED light exiting the monochromator into the optical cavity using a lens. To further check this, few tests were carried out to determine the divergence of light after exiting the monochromator. The beam diameters of light exiting the monochromator were measured at various distances from the monochromator exit in the x and y-directions (see Figure 54).

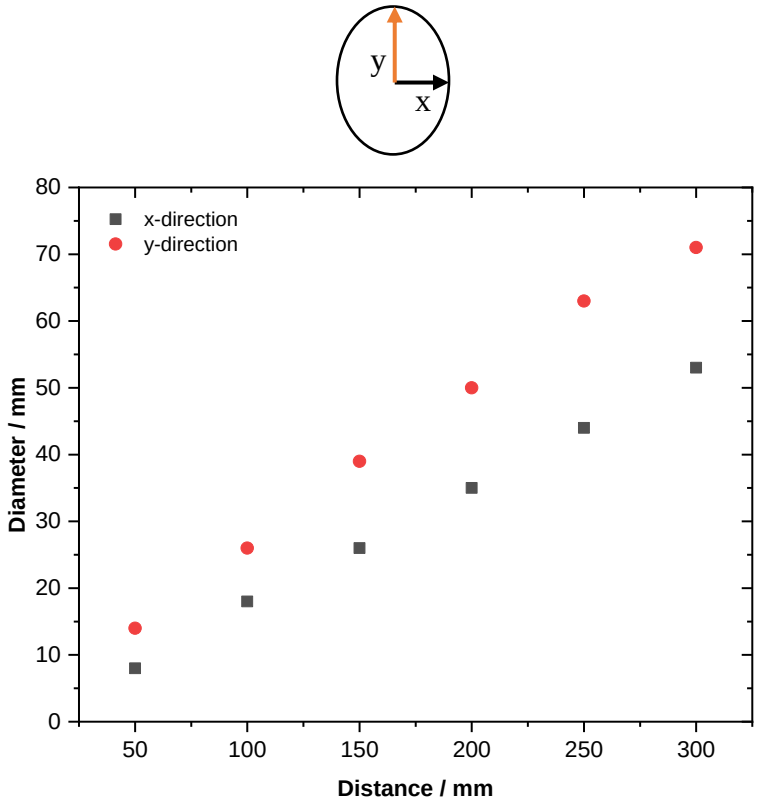

Figure 54 Beam diameters of light (along the x and y-directions) exiting the monochromator measured at various distances from the exit slit. The exit slit width (x-axis) and height (y-axis) were 600 μm and 4 mm respectively. Light was coupled into the monochromator with a 75 mm focal length plano-convex lens with f/# ≈ 3.

The NA at the exit end of the monochromator as per manufacturer specifications is 0.13 (same as its entrance NA). From Figure 54, it is observed that the beam diverges differently in the x and y-directions. The average NAs determined for the x and y-directions were 0.09 and 0.13 respectively. This indicates that the y-direction had the same NA as specified for the monochromator while that in the x-direction was much lower. For efficient coupling of light into an optical cavity, light exiting the monochromator must have the same NA in both the x and y-directions. As a test, a plano-convex lens (35 mm focal length) was placed after the monochromator exit and beam diameters were measured again in the x and y-directions as done before and the result obtained are as shown in Figure 55. Here, it was seen that the beam remains collimated over a distance of ~15 cm in the x-direction but becomes divergent along the y-direction. This indicated that placing a cylindrical lens that either converges the beam in the y-direction or diverges the beam in the x-direction to obtain an overall collimated beam could be tested in combination with the 35 mm plano-convex lens after the monochromator.

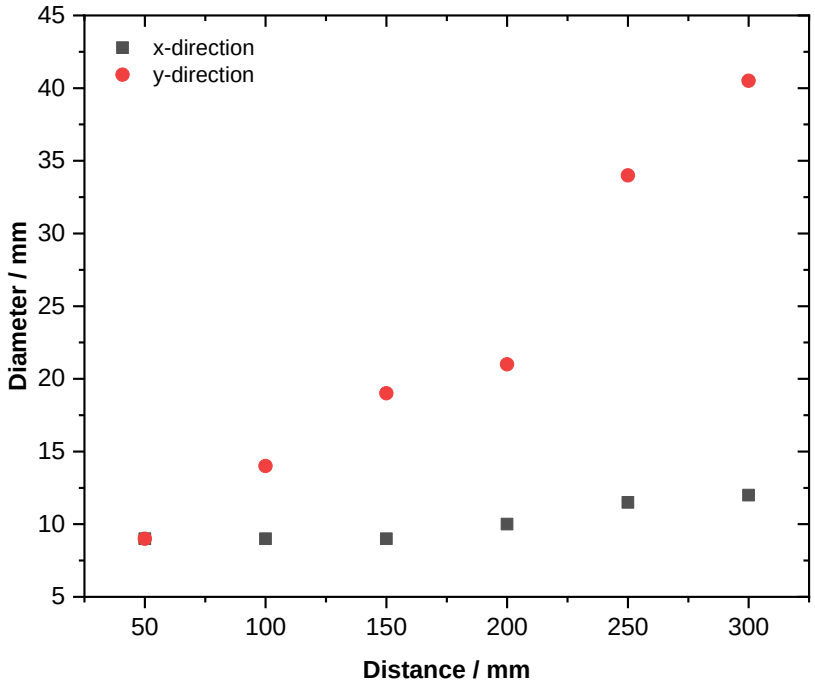

Figure 55 Beam diameters of light (along the x and y-directions) exiting the monochromator measured at various distances from the 35 mm focal length plano-convex lens placed after the monochromator exit.

Various combinations of cylindrical lenses and plano-convex lenses available in the laboratory were tried and tested to obtain a collimated beam from the monochromator exit. Unfortunately, they all failed to result in a collimated beam that could be efficiently coupled into an optical cavity. Since the LED output travelling within the monochromator is divergent by nature, an iris could be used before the monochromator entrance slit. To test this, beam diameters along the x and y-directions were measured with an iris (with aperture size ~Ø3 mm) placed before the monochromator entrance slit in the optical set-up as shown in Figure 56.

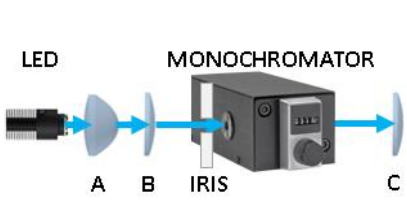

	PART
A	Aspheric lens (17.5 mm EFL)
B	Plano-convex lens (75 mm EFL)
C	Plano-convex lens (35 mm EFL)

Figure 56 Optical set-up used for determining beam diameters (along the x and y-directions) with an iris placed before the monochromator entrance slit. Iris aperture set to ~ Ø3 mm.

(a)

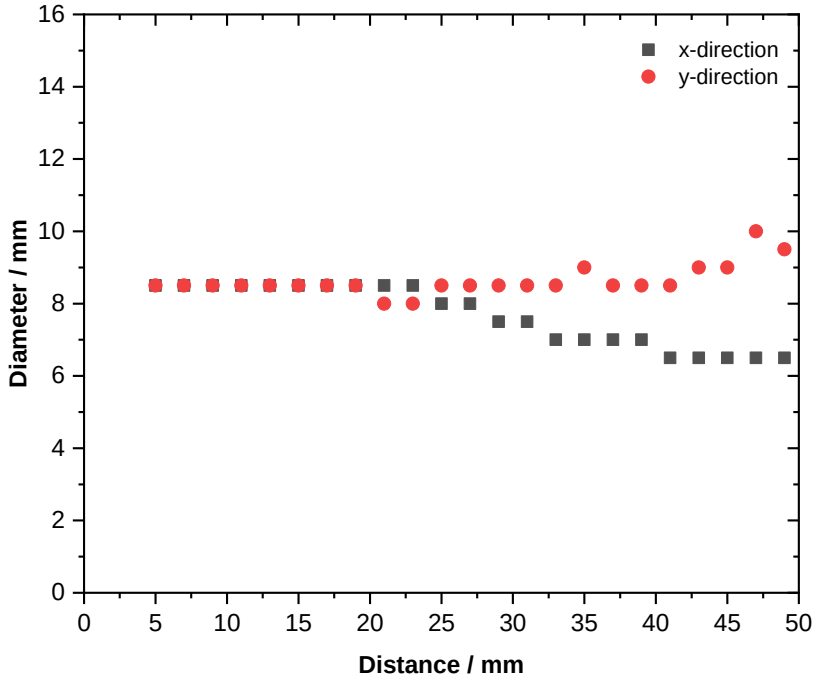

(b)

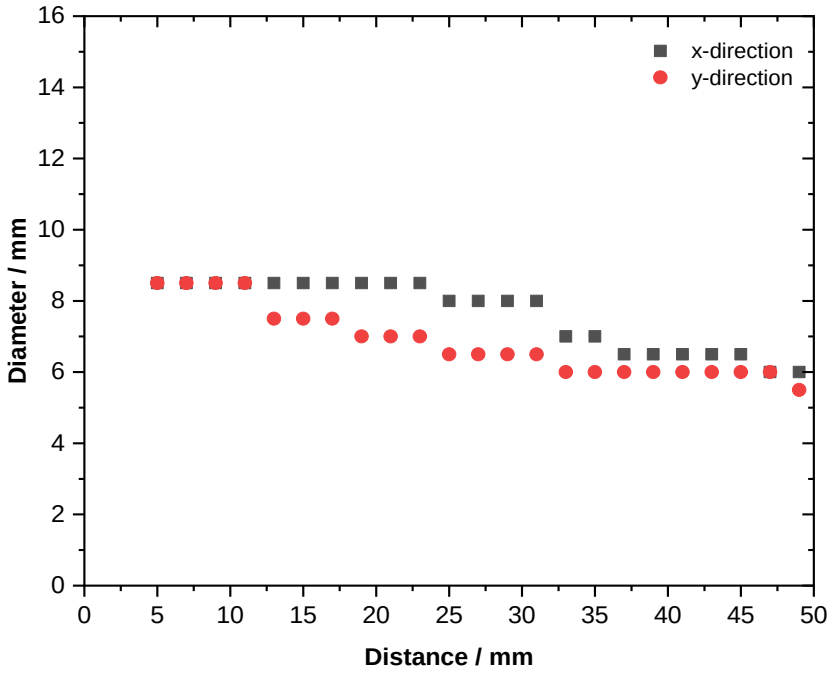

Figure 57 Beam diameters of light (along the x and y-directions) exiting the monochromator measured at various distances from the 35 mm focal length plano-convex lens placed after the monochromator exit for cases (a) with the iris completely open and (b) with the iris aperture ~Ø3 mm placed before the monochromator entrance slit.

From Figure 57 (a) and (b), in the case when iris was completely open, the beam diameters along the x and y-directions became divergent with distance. But, when the iris aperture was open by ~Ø3 mm, light at the exit end of the monochromator became collimated at a distance of about 50 mm from the 35 mm focal length plano-convex lens. From this measurement it can be said that the iris helped to control the beam spot size at the entrance slit of the monochromator and consequently helped to control the output beam size from the monochromator. Therefore, a smaller beam spot size at the entrance slit can help overcome this issue. To check if this can be further improved, a possible way to control the output from the monochromator that could be tried and tested in future would be using the configuration: LED → aspheric lens → fiber coupler → optic fiber → monochromator. In this experiment when the iris was completely open the optical power was found to be 97 µW while when the iris aperture was open by ~Ø3 mm the corresponding optical power was 49 µW.

4.9 Building an Optical Cavity

Light exiting the monochromator needs to be guided and coupled into an optical cavity to carry out CEAS measurements. Initially, a few configurations of optics were tried and tested to achieve this on the optical table assuming a cavity length of ~373 mm and keeping in mind the beam spot to be smaller than the inner diameter of the cavity (Ø16 mm) of the experimental set-up. The set-ups that met this criterion are displayed in Figure 58. The optical output behind the rear cavity mirror was measured (using a photodiode) in each case for comparison as shown in Table 8.

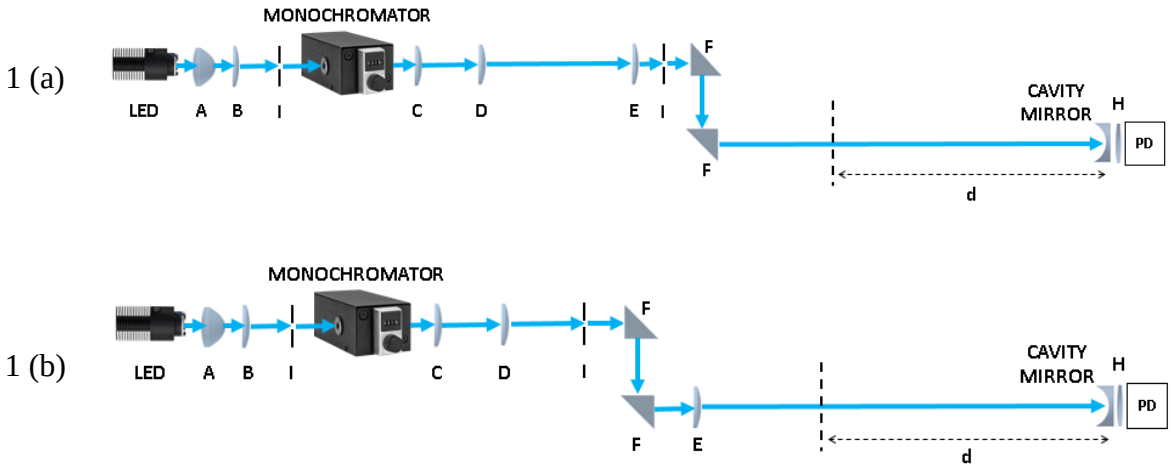

2 (a)

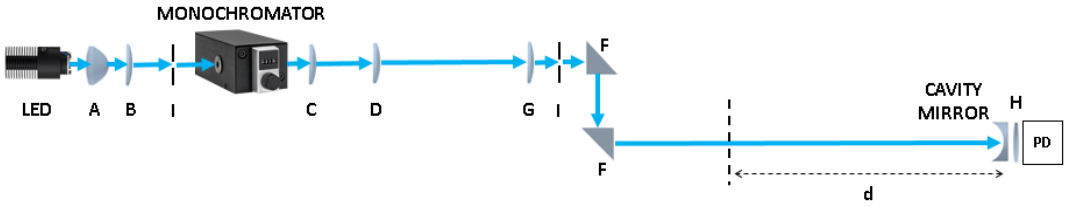

2 (b)

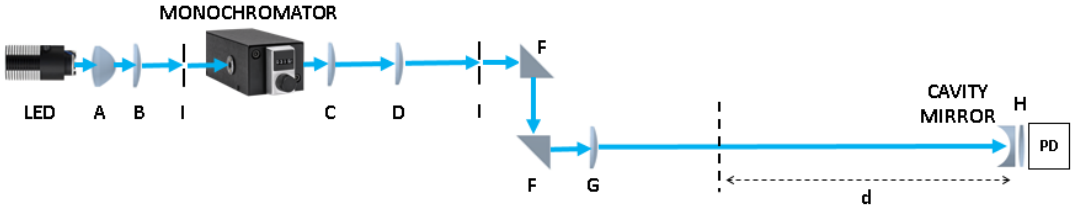

A	17.5 EFL Aspheric lens	F	Right-angle prism
B	75 mm EFL Plano-convex lens	G	300 mm EFL Plano-convex lens
C	35 mm EFL Plano-convex lens	H	25 mm EFL Bi-convex lens
D	75 mm EFL Plano-convex lens	I	Iris
E	200 mm EFL Plano-convex lens	PD	Photodiode

Figure 58 Optical set-ups tested for guiding and coupling light into an optical cavity. Set-ups (1) and (2) employ 200 mm EFL and 300 mm EFL plano-convex lenses respectively. Set-ups 1(a) and 2(a) employ: lens → iris → prisms configuration placed in between lens D and the cavity mirror. While set-ups 1(b) and 2(b) employ: iris→ prisms→ lens configuration. The cavity length was set to d ≈ 373 mm.

Optical Set-up	Photodiode signal / mV
1 (a)	31.96
1 (b)	13.96
2 (a)	4.25
2(b)	6.37

Table 8 Optical output measured using a photodiode behind the rear cavity mirror for the different set-ups shown in Figure 58.

The set-ups displayed in Figure 58 show a 200 mm or a 300 mm focal length plano-convex lens used after lens D to guide the light towards the rear cavity mirror (to couple light into the optical cavity). From the optical output signals for set-ups 1(b) and 2(b) (shown in Table 8) it is observed that placing an iris after lens D cuts off a lot of light, thus leading to low optical output power. Highest optical output power was observed for set-up 1(a) as a more intense beam spot was possible to achieve with the 200 mm focal length lens than with the 300 mm focal length lens. Also in the case of the 300 mm focal length lens, the iris aperture had to be further reduced in order to obtain a beam spot size within a 16 mm diameter. Therefore, losing a considerable amount of light in the set-up with the 300 mm focal length lens. In conclusion, these measurements indicated that set-up 1 (a) can be used to couple and guide LED light into an optical cavity. In order to test this, an open cavity was built on the optical table as shown in Figure 59. The cavity response signal was measured using the photodiode (shown in Table 9) for the cases when the cavity was aligned and when the cavity was misaligned (each cavity mirror was misaligned in a systematic manner) and it was observed that they varied by a factor of about 15 which is in close agreement with the simulated average Q_{max} value of 13.8 in the wavelength range centred around 297 nm (see Figure 43).

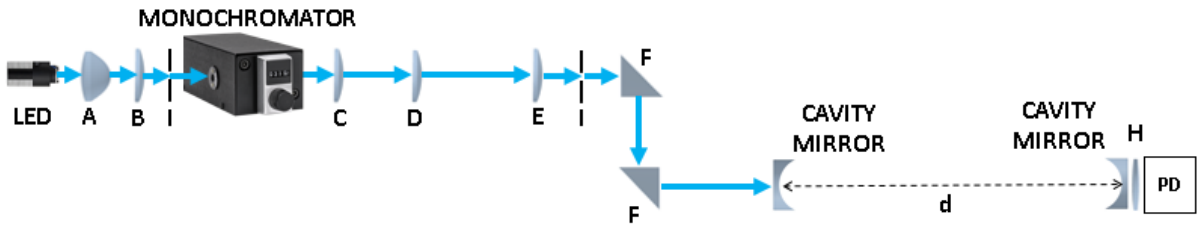

A	17.5 mm EFL Aspheric lens	F	Right-angle prism
B	75 mm EFL Plano-convex lens	H	25 mm EFL Bi-convex lens
C	35 mm EFL Plano-convex lens	I	Iris
D	75 mm EFL Plano-convex lens	d	~373 mm
E	200 mm EFL Plano-convex lens	PD	Photodiode

Figure 59 Test open cavity set-up built on the optical table with cavity length ~373 mm.

	Photodiode signal / mV
Aligned	1.267
Misaligned	0.083

Table 9 Cavity output measured with the photodiode when the optical cavity (shown in Figure 59) is aligned and misaligned.

To check optimum position and influence of the coupling plano-convex lens (E) on the overall cavity output, it was placed at three different positions from the lens (D) in the set-up shown in Figure 59. Starting from the initial position (considering this as the zeroth position) to furthest away position from the lens (D). Negative distances from the zeroth position were not measured as the beam spot on the rear cavity mirror was greater than Ø16 mm (the inner diameter of the cavity tube of the chamber set-up). The cavity output was measured for each of these cases by keeping the positions and alignments of all other optical components fixed. From Figure 60, it was observed that moving the coupling lens (E) further away from the lens (D) in the set-up (shown in Figure 59) overall lowers the optical cavity output signal. Thus, indicating that the coupling lens is coupling lesser amount of light into the cavity as moved further and further away from the lens (D).

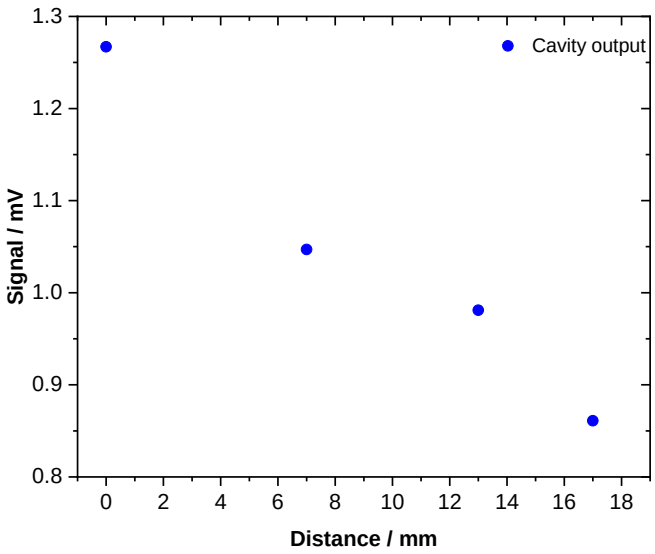

Figure 60 Cavity output signal obtained for varying positions of the coupling lens (E) from the lens (D) shown in Figure 59. Negative distances from the zeroth position were not measured as the beam spot on the rear cavity mirror was greater than Ø16 mm (the inner diameter of the cavity tube of the chamber set-up used in this project).

To check the influence of cavity length, the set-up as shown in Figure 59 was arranged such that the cavity length was about 450 mm. The optical cavity output signal was measured to be 1.156 mV corresponding to a 8.76 % decrease in the output signal. Therefore, an optical cavity set-up with cavity length ~373 mm can be built employing the configuration as shown in Figure 59 to carry out CEAS measurements. This configuration of optical set-up was integrated with the chamber system available in the laboratory for closed cavity CEAS measurements in this project.

4.9.1 Optical Cavity Measurements

In order to check the influence of the beam spot size entering the optical cavity, a graduated iris was attached in front of the entrance cavity mirror. It is known that the area of the aperture (aperture size) scales with the square of the aperture radius and therefore the same is expected for the light transmitted through the aperture assuming a uniform beam spot. Thus, a linear relation is expected between the measured intensity and the aperture area. The cavity output was determined by measuring the response of an empty optical cavity using a PMT as the detector behind the rear cavity mirror (the PMT was chosen as the detector with the optical cavity because of its lower white noise in comparison to the photodiode during the CEAS and Rayleigh scattering measurements in this project). The aperture size was varied in steps of Ø1 mm up to Ø12 mm. The transmitted light intensities are plotted against the aperture area as shown in Figure 61. In this figure, it is observed that the cavity output intensity increases with increasing aperture size as expected and a linear relation is observed in the cavity output and the aperture area for beam spots lesser than or equal to Ø6 mm which can be seen in the inset plot shown in Figure 61. However, a slight deviation from linearity is observed for apertures greater than Ø6 mm which indicates that the light incident on the cavity is not linearly transmitted through the optical cavity for beam spots greater than Ø6 mm. This non-linearity is mainly due to the light beam becoming divergent within the cavity and being lost due to reflections on the walls and surfaces within the cavity.

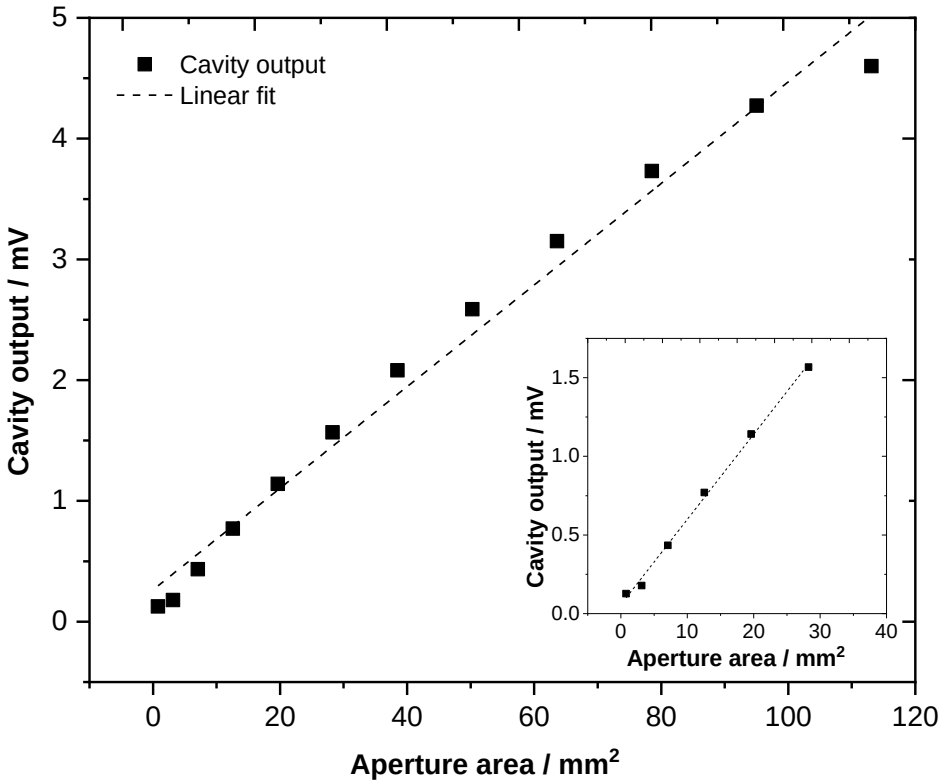

Figure 61 Cavity output measured by the PMT for varying aperture size at the entrance cavity mirror using a graduated iris. Aperture size was varied in steps of Ø1 mm up to Ø12 mm. The wavelength range involved in this measurement was 292 – 302 nm. The inset shows the plot for cavity output obtained for aperture sizes up to Ø6 mm.

The cavity losses and the amount of incident LED light interacting with the sample were investigated for the optical cavity set-up used in this project. A transmission of 2.20×10^{-4} of a single cavity mirror was directly measured in the wavelength range of 292 – 302 nm by using only the rear cavity mirror of the optical cavity set-up. The average transmission of the cavity mirrors as per manufacturer specifications in this wavelength range is 2.41×10^{-4}. But in the deep UV spectral region the dielectric coating layers of cavity mirrors show an absorption A that must not be neglected. And therefore, the transmission of cavity mirrors would be $T = 1 - R - A$ instead of $T = 1 - R$. Using the relation between cavity response I and ingoing light intensities I_{in},

$$I = I_{in} T/2 \qquad (23)$$

the expected cavity response was 68.3 mV (using measured intensity I_{in}= 621 V) but the measured value was 7.20 mV. This difference in value is mostly a result of a lot of light being lost due to high divergence of the beam that occurs within the cavity. Consequently, this results

in a low $(1 - R)$ value of the cavity (see Table 13) and thus a low enhancement factor of 0.81 (using Equation 22). Some contribution to the discrepancy in the cavity output may also be due to the positioning of the PMT. Light exiting the optical cavity is divergent. Hence capturing this light with the detector will need a lens to focus the light onto it. In this set-up the collection optics included a 25 mm focal length bi-convex lens placed in front of the PMT along with a Thorlabs FGUV11 filter to cut-off any stray light (bandpass region 275 – 375 nm). The collection optics could be tested with different sets of lenses in future to check if more light can be coupled into the detector.

Now, considering that light is lost due to divergence of the beam within the cavity and using the average reflectivity value of 0.9995 as specified by the manufacturer (in the wavelength range 292 – 302 nm) and using Equation 24 and Equation 25 [132] it was determined that the loss L was 1.59 x 10^{-3}.which is significantly larger than $(1 - R)$ value of 5 x 10^{-4}.

$$I_0 = I_{in} T^2 (1 - L) \tag{24}$$

where I_0 is the intensity after initial single pass.

$$I = \lim_{n \to \infty} I_n = \frac{I_0}{1 - (1 - L)^2 R^2} \tag{25}$$

The amount of light interacting with the sample within the cavity I_L can be calculated using the relation [132],

$$I_L = I \frac{[1 + (1 - L)R](1 - L/2)}{T(1 - L)} \tag{26}$$

From Equation 26, I_L = 65.4 V which in turn gives the ratio I_L/I_{in} = 0.11 which implies that 11 % of light intensity outside the cavity will interact with the sample.

4.10 Conclusion

From this chapter it is seen that the LED spectral output needs spectral filtering by either using optical filters or a monochromator due to the presence of undesirable wavelengths of light beyond the high reflectivity range of the cavity mirrors. But employing the monochromator has disadvantages of lower transmission along with being more challenging to set-up in the optical beam path in comparison to using optical filters. In addition to this, the monochromator posed another challenge of collimating the light exiting the monochromator

into an optical cavity as seen in section 4.8. These challenges can be overcome in the future by using custom made optical filters. Consequently, this should couple more light into the optical cavity. The configuration of LED → OAP → optical filter → coupling optic → optical cavity → spectrometer could be a way forward for future tests without having the need to use a monochromator for wavelength selection. In this configuration the spectrometer will be the wavelength selection element of the CEAS set-up. Also, the LED beam spot size incident on the optical cavity could be slightly reduced in the future in order to minimise the divergence and loss of light that continues to take place within the optical cavity. Overall, this should be able to couple more light into the optical cavity.

Chapter 5 - IBBCEAS Measurements

On establishing a stable optical cavity, calibration measurements were carried out to determine the effective reflectivities of the cavity which is an essential step in IBBCEAS in order to determine the absolute absorption coefficient of the sample. For this purpose, Rayleigh scattering measurements of N_2 at different pressures and N_2/He at 1000 mbar were carried out followed by absorption measurements of acetone in N_2 background. Since these two modes of operation utilise the same light source and optical alignment, it minimises the probable systematic errors in the measurements [133]. In these measurements the outputs from the detectors were read via a PC oscilloscope (Picoscope) linked to the PC via USB connection. The data collected was then analysed using a Python program.

5.1 Determination of Effective Cavity Mirror Reflectivities

As CEAS necessitates the calibration of $(1 - R)$ for the determination of absolute absorption coefficients (as discussed in section 2.4), the two approaches that were experimented with to determine the effective $(1 - R)$ of the cavity in this project were:

5.1.1 Nitrogen Rayleigh Scattering Measurements

5.1.2 Rayleigh Scattering Measurements of N_2/He

5.1.1 Nitrogen Rayleigh Scattering Measurements

Nitrogen was chosen for these measurements as it was readily and cheaply available in our laboratory. In order to carry out calibration measurements with N_2 at two different pressures it is necessary to ensure that the intensity varies linearly as expected. To verify this, nitrogen Rayleigh scattering measurements were carried out with the 300 nm UV-LED in the wavelength range (selected using the monochromator) 292 – 302 nm centred around 297 nm by varying pressures between 0 → 1000 mbar and 1000 mbar → 0 mbar in steps of 100 mbar. Rayleigh scattering cross-sections of nitrogen were derived from Equation 3 using the Rayleigh cross-section parameters from Ityaksov et al. [20] extended over the range of 300 nm.

5.1.1.1 Experimental Set-up

The experimental set-up used for these measurements is as shown in Figure 17 (section 3.1 in chapter 3). The LED was kept on for at least an hour to obtain a stable output before

starting any measurements (see Appendix B). The LED light was coupled into the optical cavity as explained in greater detail in section 3.1.2. The intensity of light exiting the optical cavity (I, recorded with the PMT) was normalised with the ingoing light intensity (I_{in}, the intensity of stray light that reflected off the entrance cavity mirror recorded with the photodiode). The outputs of the detectors were read simultaneously by connecting them to the two channels of the Picoscope with each channel collecting 320128 data points (1 data set containing 32 traces). The optical cavity was aligned carefully using the fine adjustment screws on the mirror mounts as shown in Figure 18. Pressures were read using the capacitance manometer (C1) attached on the chamber as shown in Figure 21. N_2 from the cylinder was gradually introduced into the chamber via a needle valve and pneumatic valve 1 in a controlled manner in order to prevent destabilising the optical cavity and for proper equilibration of the gas within the chamber. Intensities were measured from 0 to 1000 mbar in steps of 100 mbar (filling). Once topped to 1000 mbar, intensities were also measured from 1000 to 0 mbar in steps of 100 mbar (evacuating). The evacuation was also carried out in a controlled manner through a regulating valve connected to a scroll pump. On filling/evacuating to the desired pressure, a wait time of ~2 minutes was allowed for equilibration of the gas within the chamber as established from previous work carried out in the laboratory over the years for similar measurements. Background levels of light in the absence of the light source were measured every 15 minutes during the course of the measurements by blocking the LED light at the monochromator exit using a black hardboard. Temperatures were recorded using thermocouples attached on both cavity arms.

5.1.1.2 Results

The intensity ratio (I_0/I) was determined using the normalised intensity (I/I_{in}) values at each pressure for both filling and evacuating cycles. Using Equation 17, $(1-R)$ was determined from the slope of linear fits for the plots of $((I_0/I)-1)$ against number density based on the weighted Rayleigh scattering cross-section of N_2 in the wavelength range 292 – 302 nm, σ_{N_2} = 1.38 ± 0.02 x 10^{-25} cm^2 [20] and cavity length, d = 37.52 ± 0.07 cm. Figure 62 shows the plots of $((I_0/I)-1)$ against number density for the Rayleigh scattering measurements of N_2 taken at varying pressures during filling and evacuating cycles of runs 1, 2 and 3. The runs 1, 2 and 3 were carried out in succession with the same cavity alignment.

In Figure 62 (a), it is seen that although the filling cycles of the three runs are reproducible, the intensity ratio (I_0/I) – 1 shows a slight dip at ~100 – 200 mbar indicating some non-linearity at lower pressures. The same was observed for evacuating cycle of all the three runs as shown in Figure 62 (b). Also, in Figure 62 (b), it is observed that the evacuating cycle of run 2 has deviated from linearity in comparison to that of the runs 1 and 3. All of these indicate that the optical alignment is not stable while varying N_2 pressures and that the alignment needs further optimisation.

(a)

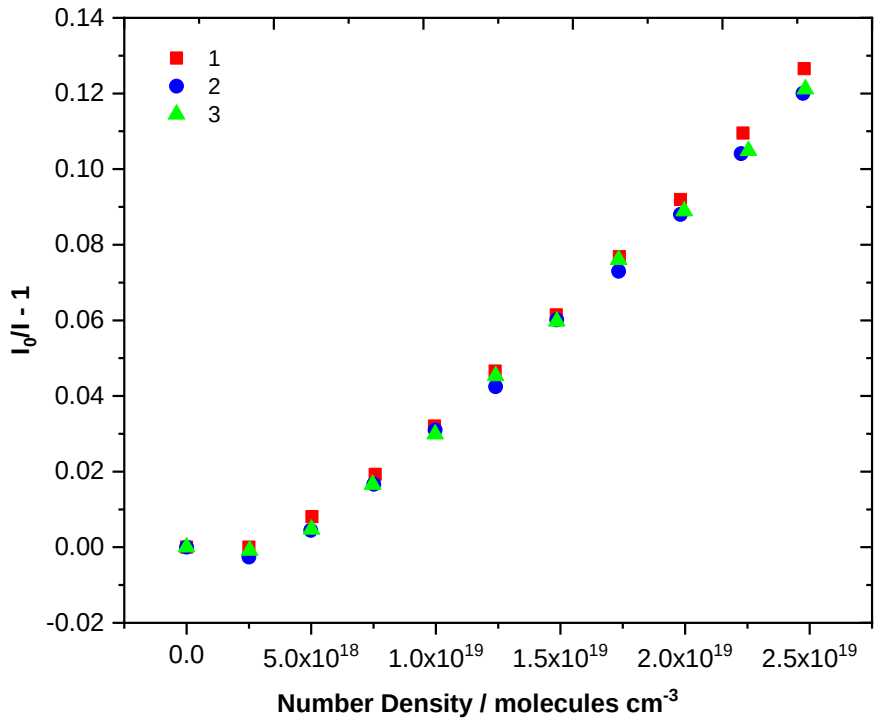

(b)

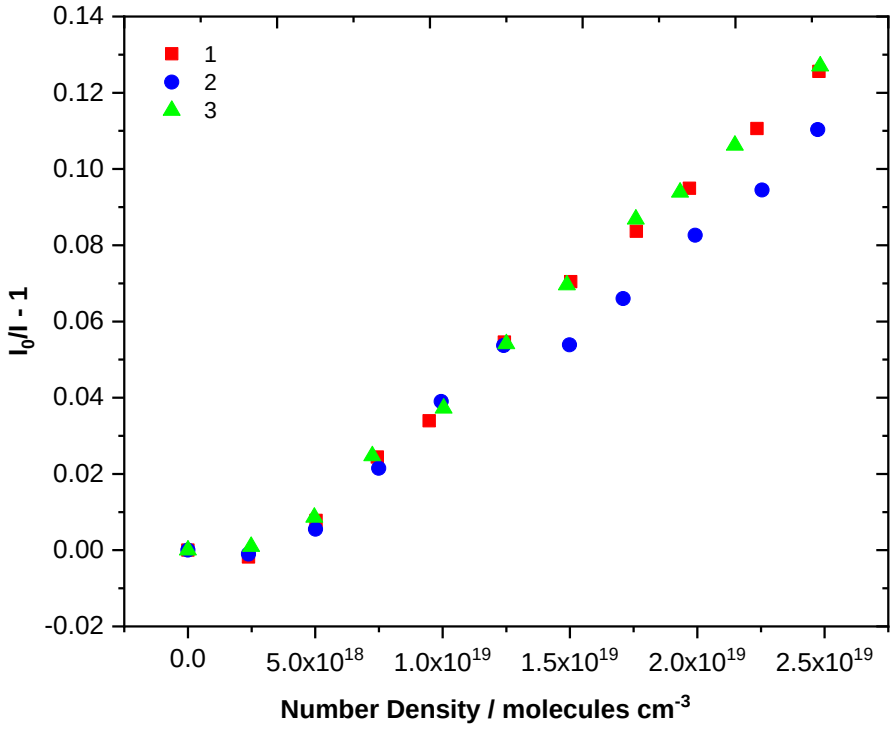

Figure 62 (I_0/I) – 1 plotted against number density of N_2 for Rayleigh scattering measurements of N_2 at varying pressures. (a) and (b) are the filling and evacuating cycles respectively for the runs 1, 2 and 3.

The adjustment screws on the cavity mirror mounts were slightly adjusted in a reproducible manner to further optimise the cavity alignment. Once the cavity alignment was optimised another set of three runs of filling and evacuating cycles for Rayleigh scattering measurements of N_2 were carried out with resulting plots as shown in Figure 63.

(a)

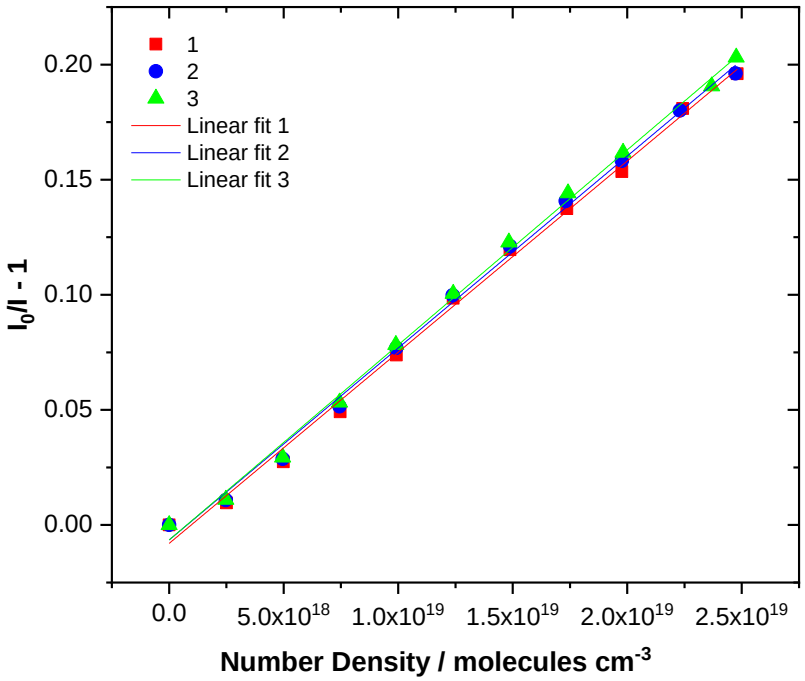

(b)

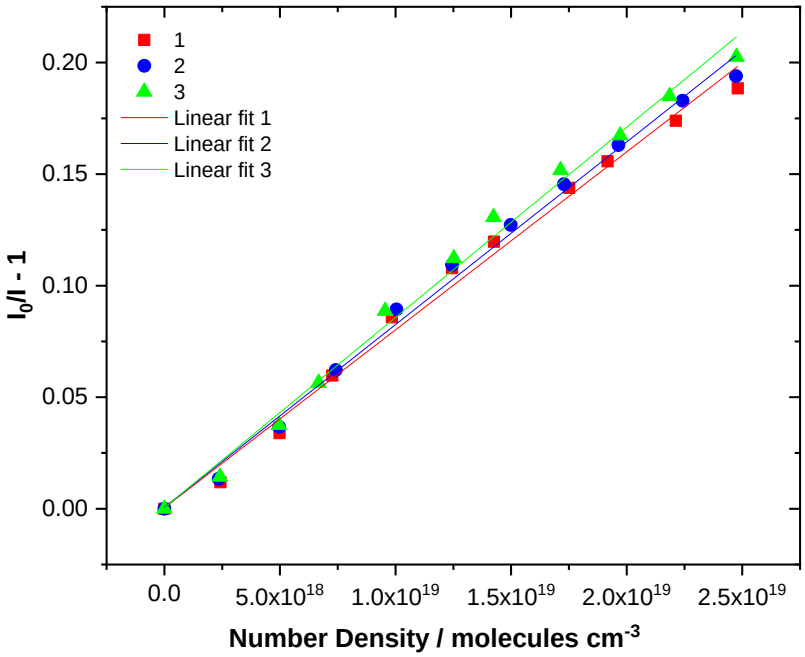

Figure 63 (I_0/I) – 1 plotted against number density of N_2 for Rayleigh scattering measurements of N_2 at varying pressures. (a) and (b) are the filling and evacuating cycles respectively for the runs 1, 2 and 3 after further optimising the optical cavity alignment used for the first set of three runs shown in Figure 62. Plots also display linear fits for the filling and evacuating cycles for each of the three runs.

The corresponding $(1 - R)$ values obtained for the three filling and evacuating cycles (a) and (b) in Figure 63 are shown in Table 10.

	Filling	Evacuating
	$(1 - R)$ x10^{-4}	
1	6.2 ± 0.2	6.5 ± 0.2
2	6.2 ± 0.2	6.3 ± 0.2
3	6.1 ± 0.2	6.1 ± 0.2

Table 10 $(1 - R)$ values determined from the slopes of linear fits of plots shown in Figure 63 (a) and (b) for filling and evacuating cycles of the runs 1, 2 and 3 carried out consecutively.

The Rayleigh scattering measurements of N_2 discussed so far were carried out before any gas manifold connections were made to the cavity mirror mounts. After gas manifold connections required to carry out acetone absorption measurements were made, several cavity alignment reiterations were carried out to obtain a stable optical alignment. A filling and evacuating cycle is carried out in order to compare the results of this approach with those obtained from N_2/He measurements (in section 5.1.2.3). The resulting plots of $(I_0/I) - 1$ plotted against number density of N_2 for the filling and evacuating cycles are shown in Figure 64. These plots show that this cavity alignment was not as stable with varying pressures as seen earlier in the case of Figure 63. The resulting $(1 - R)$ values obtained for the filling and evacuating cycle (a) and (b) in Figure 64 are shown in Table 11. The justification for discrepancy in the value of $(1 - R)$ obtained for this measurement is discussed in detail in section 5.1.1.3.

(a)

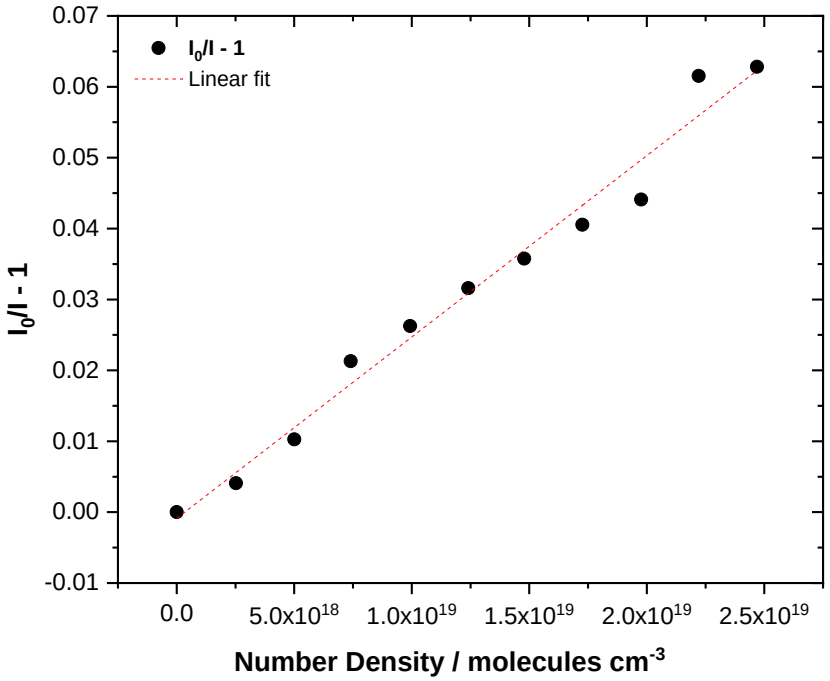

(b)

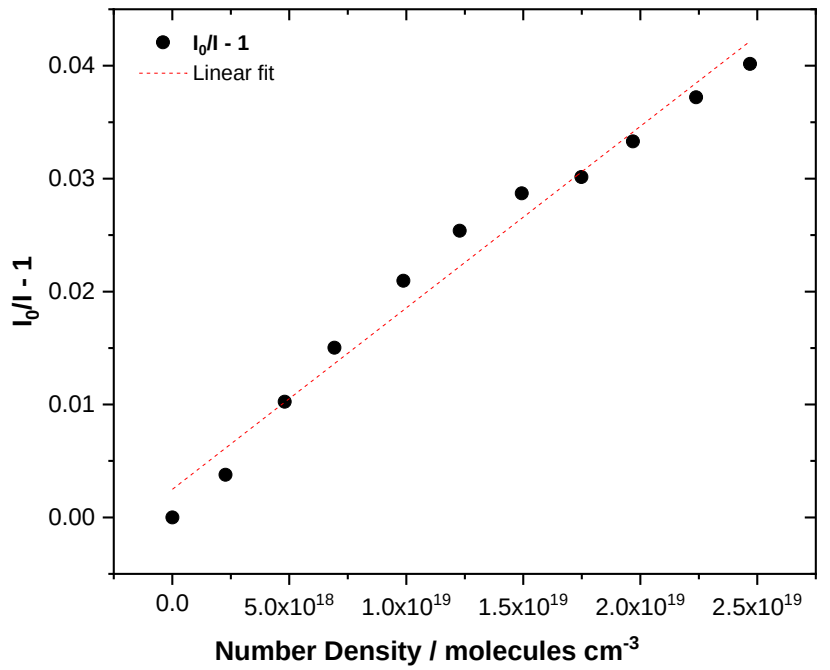

Figure 64 $(I_0/I) - 1$ plotted against number density of N_2 Rayleigh scattering measurements of N_2 at varying pressures. (a) and (b) are the filling and evacuating cycles respectively obtained for an optical alignment different from Figure 62 and Figure 63 after necessary gas manifold connections were made to the cavity mirror mounts for acetone absorption measurements. Plots also display linear fits for the filling and evacuating cycles. Details on the discrepancy and instability of this optical alignment are discussed in section 5.1.1.3.

	$(1-R)$ x10^{-3}
Filling	2.0 ± 0.1
Evacuating	3.2 ± 0.2

Table 11 $(1-R)$ values determined from the slopes of linear fits of plots (a) and (b) shown in Figure 64.

5.1.1.3 Analysis and Conclusion

Along with serving as a calibration measurement to determine $(1-R)$ values, the Rayleigh scattering measurements of N_2 at varying pressures also serve as a measurement to test the stability of the optical cavity alignment with varying pressures. From the plots (a) and (b) shown in Figure 63, it is seen that all filling and evacuating cycles of the three runs 1, 2 and 3 are reproducible as they show similar linear trends and their corresponding $(1-R)$ values lie within the 3σ of each other. The error analysis was carried out using the error propagation formula shown in Appendix D. The $(1-R)$ values have an uncertainty of 3.2 % both for filling and evacuating cycles. The major source of error towards the total error of $(1-R)$ is the error on the slope contributing ~73 % to the total error and has a relative error of 2.4 %. Therefore, implying that the optical cavity is stable with varying pressures for this optical alignment. Thus, it can be said that the filling and evacuating cycles carried out on a stable cavity alignment follows a reproducible trend with an error source mainly as a result of the fitting routine and not due to the way the measurements are carried out. In Table 10, it is observed that the $(1-R)$ value for the evacuating cycle has slightly higher value than the filling cycle in each run. When filling the cavity from 0 mbar to some pressure, the forces that act on the cavity mirrors increase and vary. In the case of an ideal cavity alignment which is insensitive to pressure variations, this pressure effect will be negligible. However, in reality the cavity mirrors experiencing this pressure variation adjust slightly to accommodate them and hence result in a small change in the cavity alignment. Hence the small difference in the $(1-R)$ values for evacuating and filling cycles is observed in Table 10.

Plots (a) and (b) in Figure 62 are for similar Rayleigh scattering measurements of N_2 at varying pressures but with an optical alignment which is slightly different from Figure 63. In these plots although some reproducibility is observed in their trends in at least two runs (except run 2) the issue of non-linearity with varying pressures is highlighted. Thus, implying

that this optical cavity alignment is not stable with varying pressures. And as mentioned earlier, these two different optical alignments discussed so far in Figure 62 and Figure 63 were obtained during optimisation of the cavity alignment before any gas manifold connections were made to the cavity mount.

Figure 64 shows one filling and evacuating cycle carried out after an optical alignment was set for acetone measurements with necessary gas manifold connections with effective $(1 - R)$ value of the optical cavity as shown in Table 11. From Figure 64 (a) and (b) it is seen that the alignment is varying with pressures and is not as stable as observed earlier in the case of Figure 63. The resulting $(1 - R)$ values are of the order of 10^{-3} and an order of magnitude higher than the values in Table 10. Also, a vast difference is observed between the filling and evacuating cycle indicating that the optical alignment is sensitive to pressure variations. The $(1 - R)$ values have an uncertainty of ~33 % between the filling and evacuating cycles and each $(1 - R)$ value has an uncertainty of ~6 %. The error on the slope of the linear fits having an uncertainty of ~5 % is the major contributor with ~98 % towards the total error on $(1 - R)$ value. The optical alignment seen in Figure 64 has resulted in a smaller intensity change with pressure (therefore smaller slope value) that is an order of magnitude lower than seen in the case of Figure 63. Thus, resulting in an effective $(1 - R)$ value of the order of 10^{-3}.

From the discussion above, it is seen that the optical cavity set-up used here for these measurements using the cavity mirror mounts (shown in Figure 18) are not good at providing a stable optical alignment with varying pressures. Hence it can be concluded that calibration measurements cannot be carried out by considering the intensity ratios of N_2 at two different pressures. A cavity that may seem well aligned at atmospheric pressure conditions may easily misalign at lower pressures. Therefore, many alignment reiterations are typically required to achieve a well-aligned cavity over the 0 – 1000 mbar pressure range as trying to optimise the alignment could either make it less stable or more stable towards varying pressures. Hence using this set-up and approach as calibration measurement for determining the effective $(1 - R)$ value of the optical cavity is not a reliable method. This issue of cavity misalignment with pressure variations could be fixed with the mirror mounts and the cage system designed for the new portable set-up as shown in Figure 23 and discussed in section 3.2. With an optical cavity alignment immune to pressure variations, the intensity ratios of N_2 Rayleigh scattering measurements at two different pressures could be employed as a calibration measurement.

Hence with the new portable set-up it will be possible to carry out N_2 Rayleigh scattering measurements at different pressures without having a need for expensive pumps to pump down to 0 mbar or needing an additional bath gas cylinder (such as He to carry out N_2/He calibration measurement).

5.1.2 Rayleigh Scattering Measurements of N_2/He

Another way of determining the effective $(1 - R)$ value of the cavity for a given optical alignment is by carrying out Rayleigh scattering measurements of two calibration gases of known Rayleigh scattering cross-sections as discussed in section 2.4. While this may seem more involved due to the use of two different gases, this approach mitigates the issue of pressure-induced cavity misalignment. While employing this approach the user must make sure that cross-contamination of the gases are minimised as a small amount of N_2 will considerably affect the He measurement. Rayleigh scattering measurements of N_2 and He were carried out with the 300 nm UV-LED in the wavelength range (selected using the monochromator) 292 – 302 nm centred around 297 nm at 1000 mbar pressure for each gas. The weighted Rayleigh scattering cross-section of N_2 in the wavelength range 292 – 302 nm is same as in section 5.1.1.2. Rayleigh scattering cross-sections of He were obtained from the empirical expression σ_{He} = 1.336 x 10^{-17} x $\lambda^{-4.1287}$ cm^2 derived by Min et al. [113] from the works of Shardanand and Rao [134].

5.1.2.1 Experimental Set-up

The experimental set-up employed for these measurements was the same as discussed in section 3.1 in chapter 3. 1000 mbar of N_2 was gradually introduced into the chamber as reported in section 5.1.1.1. The intensity of light transmitted through the cavity was measured after a wait time of about 2 – 3 mins. N_2 was pumped out gradually and once the pressure in the chamber reached a minimum value, pumping was continued for another 3 – 5 mins to make sure that all N_2 was pumped out to avoid cross-contamination. Next, 1000 mbar of He (BOC CP grade) was slowly filled into the chamber from 1 L cylinder (shown in Figure 21). Similar wait times were observed as earlier for the equilibration of the gas within the chamber. Helium was then pumped out and the chamber was flushed several times with air and N_2 (final flush) to make sure that all He was pumped out. Background levels of light in the absence of the

light source were measured before commencing the Rayleigh scattering measurement for each gas. Temperatures were recorded using thermocouples attached on both cavity arms.

5.1.2.2 Results

Nitrogen filling and evacuating tests were carried out to check the stability of the cavity on filling from 0 → 1000 mbar and evacuating consecutively several times. The chamber was gradually filled from 0 → 1000 mbar and intensities were measured after a wait time of ~2 mins. The chamber was evacuated slowly to ~0 mbar and again filled with 1000 mbar N_2. This was carried out 16 times to obtain good statistics on the data. The normalised intensities I/I_{in} were calculated for each trial. Each intensity measurement comprised a set of 32 traces i.e., 320128 data points.

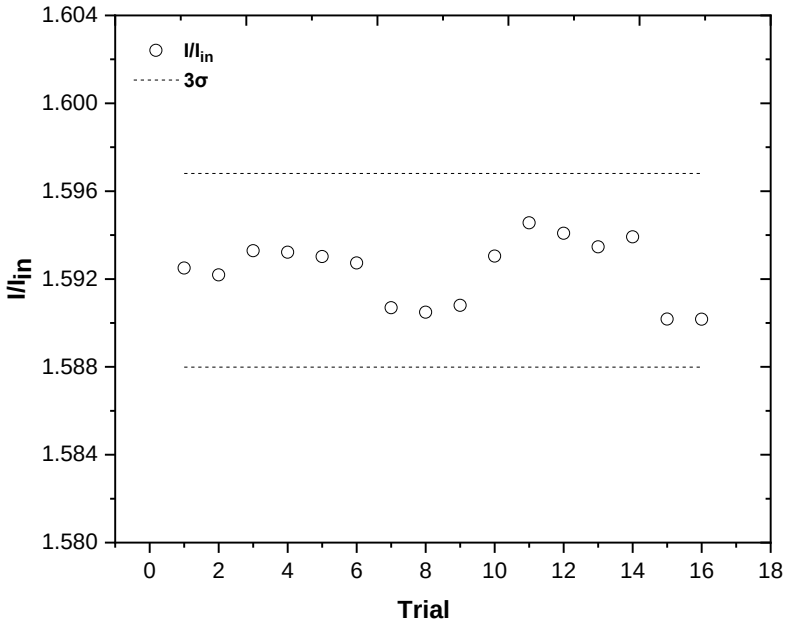

Figure 65 Normalised intensity I/I_{in} obtained for filling with 999 ± 2 mbar N_2 and evacuating consecutively several times. Consecutive trials carried out to check the stability of the cavity alignment on filling from 0 → 1000 mbar. The dashed lines represent 3σ limit of the sample mean. Each intensity value is obtained by averaging 320128 data points.

A detailed discussion on the preliminary tests and establishing a protocol for N_2/He calibration measurements are given in Appendix C.3. N_2/He Rayleigh scattering measurements were carried out in accordance to the experimental protocol established in Appendix C.3. Each intensity value was obtained by averaging the data points in 32 sets of

traces (each set 320128 data points) captured with the Picoscope. For a cavity sequentially filled with N_2 and He, $(1 - R)$ is calculated using Equation 12,

$$(1 - R) = d\left(\frac{(I_{N_2}/I_{He})\alpha_{N_2} - \alpha_{He}}{1 - (I_{N_2}/I_{He})}\right)$$

which can also be rewritten as,

$$(1 - R) = d\left(\frac{I_{N_2}\alpha_{N_2} - I_{He}\alpha_{He}}{I_{He} - I_{N_2}}\right) \quad (27)$$

where $\alpha_{N_2}$and α_{He} are the extinction coefficients for Rayleigh scattering of N_2 and He respectively. $(1 - R)$ was determined by Equation 12 using the normalised intensities (I/I_{in}) measured for N_2 and He and weighted Rayleigh scattering cross-section of N_2 and He in the wavelength range 292 – 302 nm, σ_{N_2} = 1.38 ± 0.02 x 10^{-25} cm^2 [20], σ_{He} = 1.88 x 10^{-27} cm^2 [113] respectively and cavity length, d = 37.52 ± 0.07 cm.

The resulting $(1 - R)$ values obtained for the two sets of N_2/He Rayleigh scattering measurements carried out consecutively with the same optical alignment are shown in Table 12. This was followed by a set of acetone absorption measurements (set 1) discussed in section 5.2.2.

	$(1 - R)$ x 10^{-3}
1	3.9 ± 0.4
2	3.4 ± 0.1

Table 12 $(1 - R)$ values obtained for the two sets of N_2/He Rayleigh scattering measurements carried out consecutively with the same optical alignment.

Another set of N_2/He measurements was carried out as calibration measurement to obtain the effective $(1 - R)$ value (shown in Table 13) to determine the partial concentrations of acetone in Ac/ N_2 mixture (set 2) discussed in section 5.2.2. The measurements were carried out with the same optical alignment as before.

$(1-R)$ x 10^{-3}
3.3 ± 0.1

Table 13 $(1-R)$ value obtained for N_2/He Rayleigh scattering measurements carried out with the same optical alignment as seen in Table 12 which was followed by acetone absorption measurements.

5.1.2.3 Analysis and Conclusion

The cavity was subjected to successive trials of filling with 999 ± 2 mbar N_2 and evacuating and normalised I/I_{in} Rayleigh scattering intensities measured were plotted against trials as shown in Figure 65. It was seen that successive trials lie within the 3σ limit of the sample mean with an overall uncertainty of ~0.09 %. Thus, indicating that consecutively filling the chamber to 1000 mbar and evacuating to 0 mbar was stable. Although the cavity alignment varied with varying pressures (as seen in section 5.1.1), the alignment went back to its previous position as long as the pressure differential between outside and inside the cavity was the same.

While the preliminary N_2/He test discussed in Appendix C.1 had an uncertainty of ~12 %, the $(1-R)$ values in Table 12 and Table 13 obtained from N_2/He Rayleigh scattering measurements show an overall uncertainty of 8.6 %. The major contribution of ~77 % to the total error of $(1-R)$ values comes from the error on the intensity ratio I_{N_2}/I_{He} which had an uncertainty of ~0.1 – 0.3 % (using error propagation in Equation 12). Considering the difference in intensities $I_{He} - I_{N_2}$, this had an uncertainty of ~8 %. The error on absorption coefficients of N_2 (α_{N_2}), He (α_{He}) and the cavity length contribute ~23 %, ~2.5 x 10^{-3} % and 0.2 % respectively to the total error on $(1-R)$. The intensities I_{N_2} and I_{He} have an uncertainty of ~0.07 %. Other sources of errors include the errors from the capacitance manometer and the thermocouples employed in this project. During the measurements the pressures were read out from the capacitance manometer by eye which introduced an error of ± 1 mbar on the reading in addition to the 0.25 % error on the readings from the capacitance manometer. Thus, using Equation 33 the pressure readings have an overall uncertainty of 0.27 %. The temperatures were recorded using thermocouples which as per manufacturer specifications

have an error of 1 % on the readings. This error is doubled as two thermocouples are attached, one on each arm of the cavity set-up. Thus, the temperatures have an overall uncertainty (using Equation 32) of 1.4 %.

5.2 Determination of Absorption Coefficient of Acetone

In this project, the concentrations of acetone (Ac) were determined in Ac/N_2 mixtures from CEAS measurements of gaseous acetone in N_2 at ambient conditions (1 bar, 21 °C). The effective $(1 - R)$ value of the set-up determined in section 5.1 serves as a calibration for the determination of absolute absorption coefficients of acetone using Equation 17,

$$\alpha(\lambda) = \frac{1}{d}\left(\frac{I_0(\lambda)}{I(\lambda)} - 1\right)(1 - R(\lambda))$$

where the absorption coefficient $\alpha(\lambda) = \sigma(\lambda)\,\rho_{ac}$, where ρ_{ac} is the particle density (in cm^{-3}) and σ is the absorption cross-section (in cm^2) of acetone. The weighted absorption cross-section of acetone in the wavelength range 292 – 302 nm is 8.28 x 10^{-20} cm^2. Concentrations of acetone (in ppmv) in N_2 at 1 bar can thus be determined as follows:

$$C = \frac{10^6\, k_B\, T}{\sigma(\lambda)\, d\, P\, 10^{-4}}\left(\frac{I_0(\lambda)}{I(\lambda)} - 1\right)(1 - R(\lambda))$$

$$C = \frac{10^{10}\, k_B\, T}{\sigma(\lambda)\, d\, P}\left(\frac{I_0(\lambda)}{I(\lambda)} - 1\right)(1 - R(\lambda)) \qquad (28)$$

where P and T are the pressure (in kg cm^{-1} s^{-2}) and temperature (in K) respectively and k_B (in cm^2 kg s^{-2} K^{-1}) is the Boltzmann constant. (Note that Equation 28 is valid if all inserted terms are in cm).

5.2.1 Experimental Set-up

The experimental set-up employed was the same as the one used for calibration measurements as shown in section 3.1 in chapter 3. N_2/He Rayleigh scattering calibration measurement was carried out before any absorption measurement in order to determine the effective $(1 - R)$ value of the cavity set-up. A Rayleigh scattering measurement with 1000 mbar of N_2 served as a background (I_0) for acetone absorption measurements. Gas mixtures for Ac/N_2 measurements were prepared as explained in detail in section 3.1.4. A

small amount (typically 50 – 52 mbar) of Ac/N_2 was introduced into the chamber from the mixing cylinder and topped up to 1000 mbar with N_2. Intensity measurements were carried out after a certain time in which the mixture equilibrated within the chamber. Consecutive Ac/N_2 measurements were carried out by subsequent dilutions of the mixture in the chamber.

5.2.2 Results

After keeping the LED and PMT on for ~2 hours (according to the protocol established in Appendix C.3) about 1000 mbar of N_2 was admitted into the chamber to test the stability of the N_2 background. The intensities of light transmitted through the cavity and ingoing light (stray light captured with the photodiode) were measured. A total of 32 sets of data were captured with each set containing 32 traces (320128 data points).

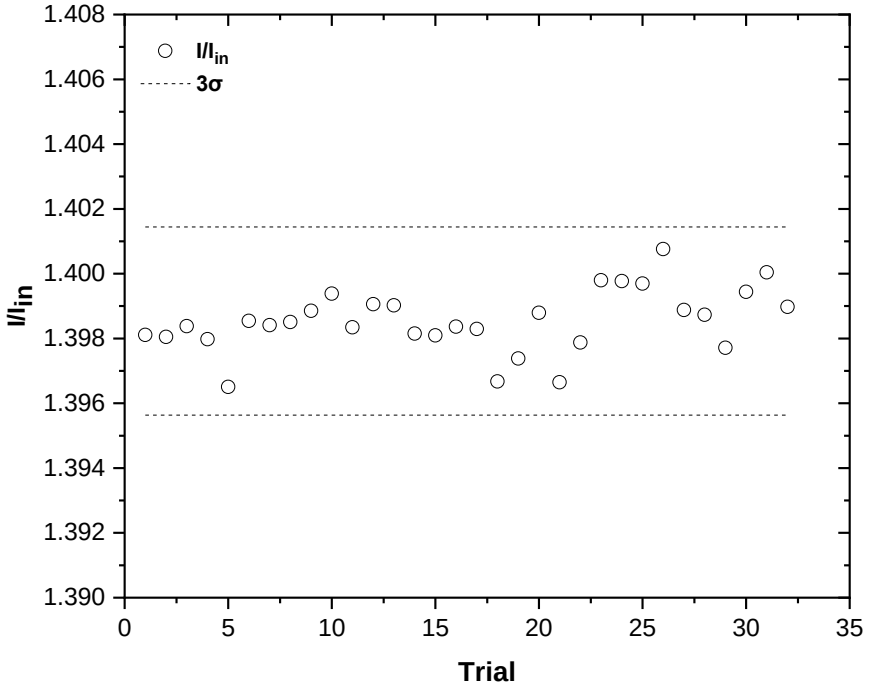

Figure 66 Normalised intensity I/I_{in} measured for the chamber filled with ~1000 mbar N_2 to check the stability of the N_2 background. The dashed lines represent 3σ limit of the sample mean. Each intensity measurement point shown here is an average value of 320128 datapoints. The duration of these measurements was 11 mins.

To test the stability and equilibration of Ac/N_2 mixture in the chamber over time, intensity measurements of the first mixture of set 1 was monitored for about an hour after the mixture was allowed to equilibrate in the chamber for ~4 mins. Over this time period, 45 sets

of measurements were conducted with background levels of light measured (carried out as before) every 15 minutes.

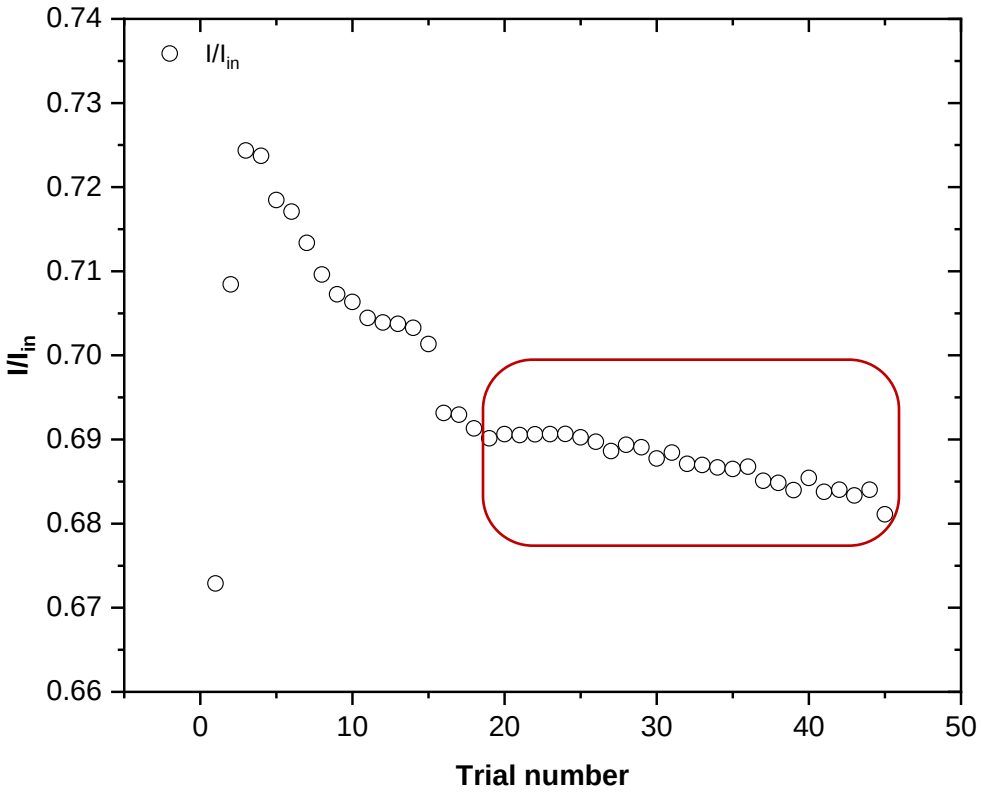

Figure 67 Normalised intensities I/I_{in} (45 sets) measured for first Ac/N_2 mixture of set 1. The data within the box was analysed as mixture 1. The mixture equilibrates around the 19th trial which is ~21 mins from the commencement of measurements. Each point shown here is an average of 320128 datapoints.

From Figure 67 it can be seen that the mixture has not equilibrated even after 4 minutes wait time before starting the measurements. The mixture becomes equilibrated around the 19th set of measurement which is ~21 mins from the start of measurements. The next measurements were carried out by subsequent dilutions (aimed subsequent dilutions were 25 %, 50 % and 75 %) of the initial mixture in the chamber. The intensity measurements (32 sets of traces) were carried out after ~21 mins of wait time to allow the mixture to equilibrate within the chamber. The absolute absorption coefficient of acetone was determined using Equation 17. Acetone concentrations (in ppmv) in N_2 background were calculated using the average of $(1-R)$ values from Table 12 and, N_2 background $I_0 = 1.3937 \pm 0.0009$ and $d = 37.52 \pm 0.07$ cm using Equation 28.

Mixture	Measured acetone concentration / ppmv
1	49.6 ± 4.1
2	41.8 ± 3.4
3	21.5 ± 1.8
4	6.97 ± 0.58
5	2.70 ± 0.24

Table 14 Concentrations of acetone in N_2 background for various mixtures of set 1calculated using the average $(1 - R)$ value from Table 12. The aimed subsequent dilutions were 25 %, 50 % and 75 %.

A N_2/He Rayleigh scattering calibration measurement was carried out to determine the effective $(1 - R)$ value of the set-up (see Table 13) before the next set of acetone mixtures were analysed. For mixtures of set 2, after a small amount of Ac/N_2 mixture was introduced into the chamber from the mixing cylinder it was topped to an overall pressure of 500 mbar with N_2. After a wait time of ~40 mins (for thorough mixing), it was topped to 1000 mbar with N_2. Following this, another wait time of ~21 mins was allowed for the mixture to equilibrate. For subsequent mixtures the dilution (50 %) was carried out each time by pumping out 500 mbar of the initial mixture in the chamber and topping to 1000 mbar with N_2, followed by ~21 mins of equilibration time. The partial concentrations of acetone in these mixtures were obtained using $(1 - R)$ value from Table 13 and, background I_0 = 1.390 ± 0.001 and d = 37.52 ± 0.07 cm using Equation 28.

Mixture	Measured acetone concentration / ppmv
1	31.0 ± 1.1
2	15.6 ± 0.5
3	7.30 ± 0.25
4	4.23 ± 0.17
5	2.76 ± 0.13
6	2.20 ± 0.09

Table 15 Concentrations of acetone in N_2 background for various mixtures of set 2 calculated using the $(1 - R)$ value from Table 13. The aimed subsequent dilutions were 50 %.

5.2.3 Analysis and Conclusion

Test for stability of N_2 background shows (in Figure 66) that the normalised intensities (I/I_{in}) are within the 3σ limit of the sample mean and the measurements have an overall uncertainty of ~0.07 %. Thus, implying that N_2 background is stable to carry out acetone absorption measurements in N_2 background. An uncertainty of ~8.4 % was observed for concentrations of acetone (in N_2 background) for various mixtures from set 1 and ~3.8 % in the case of set 2. This higher uncertainty was mainly due to insufficient time allowed for equilibration of the mixture within the chamber in the case of set 1. Therefore indicating that the approach used to attain equilibration of mixtures within the chamber in set 2 was better than the approach used in the case of set 1. Temperatures and pressures in these measurements had an uncertainty of 1.4 % and 0.27 % respectively (determined using Equation 32 and Equation 33 in Appendix D). By applying error propagation formula Equation 34 to concentration Equation 28, it was found that the error on $(1 - R)$ contributed ~67 % and the error on intensity ratio I_0/I contributed ~17.5 % to the total error on the concentrations of acetone for set 2. Hence the error on $(1 - R)$ was a major contributor to the total error on the concentrations of acetone in Ac/N_2 mixtures. (And as seen from section 5.1.2.3 the error on intensity ratio I_{N_2}/I_{He} was the major contributor to the total error on $(1 - R)$). The intensity ratios I_0/I for the concentrations of acetone have an uncertainty of ~0.15 %. The intensities

(I) measured for various concentrations of acetone have an uncertainty of ~0.13 % which could be minimised by using a better mixing system. Other sources of error include the errors on temperature and pressure that contribute ~15 % and 0.5 % respectively to the total error on the concentrations of acetone in Ac/N_2 mixtures. The error on the pressures can be reduced to ~0.25 % by using a program such as LabView to record the pressures rather than taking readings by eye.

In the case of mixtures 5 and 6 in Table 15, the expected concentrations should have halved on dilution, but it had decreased by only ~20 %. This was mostly as a result of adsorption of acetone to the inner walls of the chamber at lower partial concentrations. Over time some of this acetone gets desorbed from the chamber walls due to collisions with N_2 molecules. This clearly indicated that one should trust the measured concentrations than the calculated concentration ratios. The lowest amount of acetone (2.2 ppmv) analysed in set 2 mixture 6 corresponds to about 2 x 10^{-3} mbar i.e., absorption coefficient of ~4.5 x 10^{-6} cm^{-1}. For future measurements a better mixing system that spans the range of dilutions would be required with a sufficiently large mixing cylinder. In order to prevent issues of long mixing times and partially mitigate the issue of adsorption, a flow system could be used rather than a stagnant cell. The overall volume of the cavity chamber could be reduced, thus requiring less sample and should also speed up mixing.

5.2.4 Minimum Absorption Coefficient

In IBBCEAS the minimum absorption coefficient α_{min} that can be measured with the experimental set-up can be determined using [93],

$$\alpha_{min} = \frac{1}{d}\left(\frac{\Delta I_{min}}{I}\right)(1 - R) \qquad (29)$$

where ΔI_{min} considers the 3σ standard deviation of statistically significant data set of transmissions of a target-free cavity which in this case would be a N_2 background measurement. It is clear from this equation that the minimum absorption coefficient depends on the smallest detectable intensity variation $\Delta I_{min} = (I_0 - I)_{min}$. Considering the average of the N_2 measurements carried out for the last set of acetone absorption measurements (set 2), 3σ standard deviation $\Delta I_{min}/I$ = 3.1 x 10^{-3}, average $(1 - R)$ = 3.5 ± 0.3 x 10^{-3} and

d = 37.52 ± 0.07 cm, the minimum absorption coefficient is 2.8 ± 0.2 x 10^{-7} cm^{-1} which corresponds to ~0.1 ppmv (~1 x 10^{-4} mbar) of acetone.

The averaging time corrected noise-equivalent absorption coefficient (α_{NEA}) of the set-up was obtained using [93],

$$\alpha_{NEA} = \alpha_{min}(t^{\frac{1}{2}}) \quad (30)$$

Considering the total data acquisition time for background and absorption measurements (time, t = 204.86 s), the resulting noise-equivalent absorption coefficient is 4.1 ± 0.3 x 10^{-6} $cm^{-1}Hz^{-1/2}$ (corresponding to ~2 ppmv of acetone). The resulting noise-equivalent absorption coefficient (NEA) can be used for comparison of instruments using different detection methods [93].

From Equation 29, it is seen that α_{min} that can be measured with this set-up could be further improved if the effective $(1 - R)$ value of the cavity were of the order of 10^{-4}, and if the cavity length were increased to, for example, a 50 cm (considering the case that LED light could be coupled for this cavity length). This can improve the α_{min} value by almost an order of magnitude. However, from experience of working with the 300 nm LED which is highly divergent, in order to achieve a lower α_{min} value by simply increasing the cavity length will be difficult. This will truly require a less divergent LED that will also consequently improve light injection into the cavity. If α_{min} needs to be further improved by using cavity mirrors of higher reflectivity, this will further reduce the amount of light being coupled into the cavity and this would need a more radiant LED light source than the one currently being used. As seen in section 4.9.1, a lot of light is lost due to the divergence of the beam within the cavity and consequently this has resulted in low value of $(1 - R)$. Therefore, with better light coupling and less divergent LED, it should be possible to attain an effective $(1 - R)$ value an order of magnitude lower than currently achieved, consequently improving the limit of detection by almost an order of magnitude.

The literature on gas-phase acetone IBBCEAS measurements using a UV-LED is sparse. Most acetone absorption measurements seen in the literature were generally carried out for breath acetone analysis. As one of the potential applications of this set-up is as a breath acetone analyser, this section summarises some of the experimental techniques and their sensitivities

employed in the detection of breath acetone. Recently in 2018, Li et al. [54] developed a compact breath acetone analyser based on a UV-LED peaking at 285 nm. The gas analyser employed in their work was a compact multi-pass cell with a lower detection limit of 0.7 ppmv for acetone which is lower by a factor of ~3 in comparison to the NEA that can be achieved with the IBBCEAS set-up employed in this project. In 2007, Wang et al. [135] constructed a portable CRD acetone detector (using acetone sample solutions) employing a Q-switch Nd:YAG laser operating at 266 nm with a detection limit (based on 1σ) of 0.49 ppmv. A quantum cascade laser (QCL) based mid-IR CEAS detector for breath acetone detection was demonstrated by Ciaffoni et al. [136] with a detection limit of 0.51 ppmv and optimal acquisition time of 0.2 s. Dummer et al. [48] measured breath acetone concentrations in the range of 600 – 3000 ppbv using SIFT-MS. A detection limit of 0.049 ppbv for acetone in breath was achieved by Deng et al. [137] by using GC-MS and solid-phase microextraction (SPME) with on fiber-derivatization. Denzer et al. [138] used a supercontinuum source in the near-IR using Fourier transform IBBCEAS which had α_{min} of ~4 x 10^{-9} cm^{-1} within a 4 min acquisition time. In 2015, high sensitivities of 57 ppbv were achieved by Sun et al. [139] using a Q-switched Nd:YAG laser at 266 nm in a portable CRD breath acetone analyser. Blaikie et al. [52] used a near-IR diode laser (at ~1670 nm) in their portable device and demonstrated a limit of detection of 159 ppbv (1σ) on samples from breath bags. From this summary it can be concluded that although most commonly used GC and MS techniques have been able to obtain lower limit of detection with low uncertainties, (as already mentioned in section 1.8.2) these instruments are bulky (therefore not portable), expensive, require skilled operators and have long response times. All these disadvantages make them less desirable for real-time point-of-care monitoring of breath acetone. The spectroscopic analysers operating in the IR range have the disadvantage arising from strong interferences from other gas species in exhaled breath. Hence, requiring use of filters and calibrations that complicate the system in comparison to techniques operating in the UV range which are at less risk from interference. The CRDS in the UV range seen in this summary were mostly carried out at 266 nm. At this wavelength the cavity mirror materials fluoresce, which in the long run of this project, if fluorescence measurements (LIF) are to be carried out for acetone, would create a background noise. While around 300 nm the cavity mirror materials do not fluoresce. Thus, a portable acetone analyser based on a UV-LED has potential applications in the field of medical diagnostics.

The average breath acetone concentration in healthy people is in the range of 0.39 – 1.09 ppmv [140], but the minimum detectable acetone concentration in terms of its NEA that can be achieved with the set-up used in this project is ~2 ppmv which is about an order of magnitude higher for detection of breath acetone. If an effective $(1 - R)$ value of the cavity of the order of 10^{-4} is attained with better light coupling into the cavity and with a more intense LED, it should be possible to further improve the limit of detection (LOD) of the set-up into the range of few ppbv. Also, in future if this set-up is used in conjunction with LIF (as a combination of IBBCEAS and LIF) and with the availability of high-power UV-LED it should be possible to further improve the LOD of the set-up. With these upgrades, this set-up has potential application as a breath acetone analyser and as a detector for trace gas species in atmospheric field measurements.

5.3 Conclusion and Future Work

The main aims of this project were the design of a portable analyser based on Cavity-Enhanced Absorption Spectroscopy (CEAS) using a UV-LED to detect trace gas species in the atmosphere and in exhaled breath, with acetone as a model system (as a biomarker particularly in people on a ketogenic diet or to detect/monitor DKA condition) in real-time and also as proof of principle that a UV-LED can be used as an excitation light source in place of a laser. In addition to these aims, overall the design of the set-up needed to be portable, robust and cost-effective.

There are several advantages to using an LED as a light source instead of a laser (and other light sources) as discussed in detail in section 2.5. Despite these advantages, one of the major challenges in this project (as seen in chapter 4) was collimating and coupling LED light into the optical cavity. This was mainly due to the unavailability of suitable off-the-shelf collimation optics in the desired UV wavelength range. Although a few optics could be customized, it would defeat the aim of making the set-up cost-effective as custom-built optics tend to be highly priced. Despite these challenges, the collimation and coupling of LED light into the optical cavity was achieved and CEAS measurements of acetone with the 300 nm LED were carried out employing the experimental set-up available in our laboratory (with necessary modifications). The IBBCEAS set-up with the 300 nm LED achieved a noise-equivalent absorption coefficient of $4.1 \pm 0.3 \times 10^{-6}$ $cm^{-1}Hz^{-1/2}$ (corresponding to ~2 ppmv of acetone).

Thus, establishing as a proof of principle that a UV-LED can be used as an excitation light source in place of a laser.

The IBBCEAS set-up employed in this project can be integrated with the designed portable set-up (discussed in section 3.2) that will provide the experimental system with mechanical rigidity and robust optical alignment along with immunity to vibrations and variations in temperature and pressure. With a more stable optical alignment that is insensitive to pressure variations it should be possible to carry out nitrogen Rayleigh scattering measurements at two different pressures to determine the effective $(1 - R)$ value of the cavity. Overall, the simplicity of operation and portability of the set-up point towards its potential to be used in applications in atmospheric chemistry for field measurements and in medical diagnostics as a breath acetone analyser.

In terms of making changes or improvements to the experimental set-up, there are some options that could be employed. One of these options is to use an LED smaller in size even if it has less output power as it would allow to form a better collimated beam. A couple of collimation lenses could also be used to shape the beam which would simultaneously help align the cavity. Also, if the LED was small enough in size, a parabolic mirror could be used for collimation instead of an aspheric lens. In terms of spectral filtering, a narrow-band interference filter could be used instead of the monochromator as this poses far fewer issues in terms of beam alignment (which is discussed in section 4.8) and also have a higher transmission than the monochromator. However, the issue with the optical filters is that they may not be suitable for a replacement LED due to variation of centre wavelengths from different LED batches. The other alternative could be using a fibre-coupled LED. Although its output power is considerably less than that of the 300 nm LED used in this project, the output light is fully collimated and will be able to couple a larger amount of light into the cavity.

In terms of coupling the LED light, as future work there are a few optical configurations that could be tried with an optical fiber. In the case of an optical fiber, it could be easier to collimate the light that emerges out at its exit and couple into the cavity. One of the possible configurations that could be tested is: LED → aspheric lens → fiber coupler → optical fiber → monochromator → optical fiber → OAP mirror → optical cavity. This may help to achieve a beam entering the cavity that would not experience large loss of light due to divergence as seen in the current set-up. Another possible alternative based on a suitable custom optical filter

would be: LED → optical filter → aspheric lens → fiber coupler → optical fiber → OAP mirror → optical cavity.

Apart from using an LED in continuous mode, LEDs can also be operated in pulsed mode to carry out CRDS by measuring the ring-down transient. Although, this will need rapid optical switching of an LED. There are fast optical pulse generating circuits which are fairly easy to build that allow the fast switching (ns) of an LED [141, 142]. Other possibility includes intensity modulation of LED output to carry out Phase-Shift CRDS (PS-CRDS). In this technique, intensity modulated LED light incident on the cavity undergoes a phase shift $\phi(\lambda)$ due to the presence of the cavity. Absorption can be determined from the wavelength-dependent phase-shift, that is related to the ring-down time $\tau(\lambda)$ and the angular modulation frequency Ω by:

$$\tau(\lambda) = -\Omega^{-1}\tan[\phi(\lambda)] \qquad (31)$$

PS-CRDS technique can also be employed as a calibration approach to determine the effective reflectivity of the cavity mirrors. Measurements of PS-CRDS are best carried out employing a lock-in amplifier to determine the phase-shift between the ingoing intensity modulated light and the phase-shifted light exiting the cavity [87, 143, 144].

In 2013, the groups of Nahler and Wrede [132] developed the technique of Cavity Enhanced Laser-Induced Fluorescence (CELIF), a combination of Cavity Ring-Down Spectroscopy (CRDS) and Laser-Induced Fluorescence (LIF). In CELIF, which makes use of a pulsed laser as an excitation light source, the CRD and LIF transients are measured simultaneously on a shot-to-shot basis. This technique has demonstrated high sensitivity and a large dynamic range for the determination of absolute absorption coefficients. In the future the new set-up can be upgraded to carry out simultaneous IBBCEAS and LIF measurements based on a UV-LED. This should also make it possible to attain lower limit of detection than currently achieved in this project. The 300 nm LED used in this project lacked adequate number of photons (3 photons per second for an acetone concentration of 1 ppmv) required for simultaneous LIF measurements. CEAS-LIF measurements in this UV range should be possible in a few years when more powerful LEDs will become available in the market.

Similar CEAS measurements can be carried out with high power LEDs at a different wavelength. The 455 nm LED available in our laboratory can be used to carry out measurements on glyoxal/NO_2 mixtures. Glyoxal (CHOCHO) which is an important

atmospheric trace gas species has been gaining importance in the field of atmospheric chemistry due to its role in aerosol formation and its utility as an indicator for oxidative chemistry. Glyoxal has been found to contribute to the formation of Secondary Organic Aerosol (SOA) and has been proposed as an indicator of SOA formation in the atmosphere. The apparent utility as a tracer for atmospheric oxidative processes and SOA formation make glyoxal advantageous for satellite validation and model inter-comparison [145]. Measurement of glyoxal in the atmosphere serves as a vital indicator molecule for Volatile Organic Compound (VOC) chemistry. For the detection of glyoxal by CELIF in the background of NO_2, the NO_2 in the sample will be detected via absorption and for determination of glyoxal, the plan is to do a subtraction of the NO_2 background based on glyoxal fluorescence or phosphorescence.

This CELIF set-up can be integrated into the cage system (as discussed in section 3.2) inspired from the set-up used by Min et al. [113]. This cage system will provide greater mechanical rigidity and stability to the optical cavity making it insensitive to temperature and pressure variations. Overall, this will make the set-up portable and make it feasible to move the set-up outside the laboratory environment and carry out atmospheric field measurements. Also, the cage system integrated set-up has potential applications in medical diagnostics as a breath acetone analyser for real-time monitoring of DKA or in people following a ketogenic diet.

Appendix A Detectors

Appendix A.1 Photodiode

The photodiode (MicroFJ-SMA-30035, SensL) employed in this project is a Silicon Photomultiplier (SiPM) composed of an array of single photon avalanche diodes (SPADs). The photodiode has an active sensor area of 3.07 x 3.07 mm^2. The responsivity curve of the photodiode (as per manufacturer specifications) is as shown in Figure A. 1.

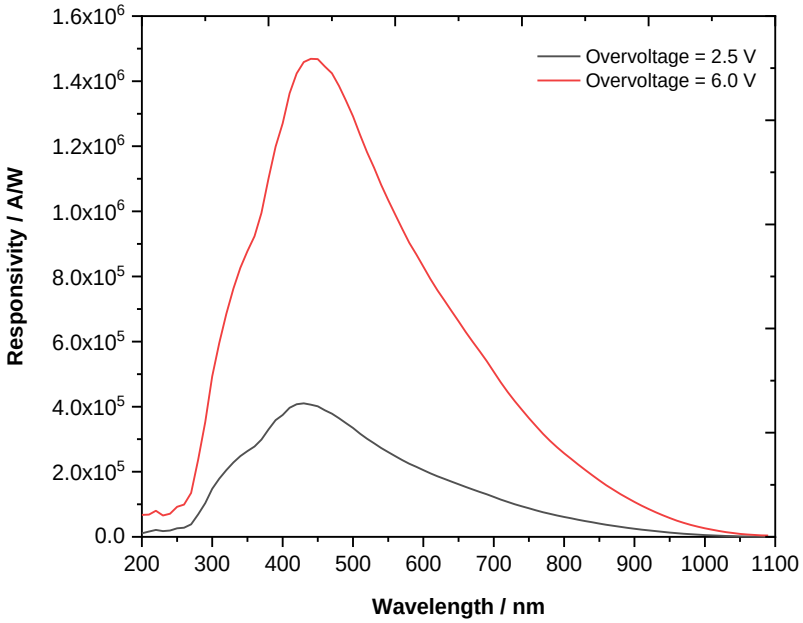

Figure A. 1 Responsivity of the photodiode as a function of wavelength at + 2.5 V and + 6 V overvoltage (provided by manufacturer). These overvoltages correspond to 27 V and 30.5 V bias voltage respectively. (Bias voltage = average breakdown voltage + overvoltage)

The average breakdown voltage of the photodiode is 24.5 V. Overvoltage that can be applied over its breakdown voltage ranges from 1 – 6 V. During characterisation of 300 nm LED the photodiode was typically operated at an overvoltage of 2.5 V with the bias supply set to 27 V. The responsivity at 2.5 V overvoltage (supplied by manufacturer) was used to determine the light intensity in terms of power (mW). During Rayleigh scattering measurements and acetone absorption measurements the photodiode was operated at 26.6 V. As per the information from the manufacturer, the responsivity *R* of the photodiode does not

vary linearly with applied overvoltage and is related to the gain (G), photon detection efficiency (PDE), crosstalk probability (PXT), after-pulsing probability (PAP) as,

$$R = \frac{PDE\ x\ \lambda\ x\ G\ x\ e\ (1 + PAP)(1 + PXT)}{h\ x\ c\ x\ 100\ \%}$$

where λ is the light wavelength, e is the electron charge, c speed of light and h is the Planck's constant.

Appendix A.2 PMT

The PMT used to measure the cavity output intensities is a Hamamatsu R1527 that has the responsivity and quantum efficiency as shown in Figure A. 2.

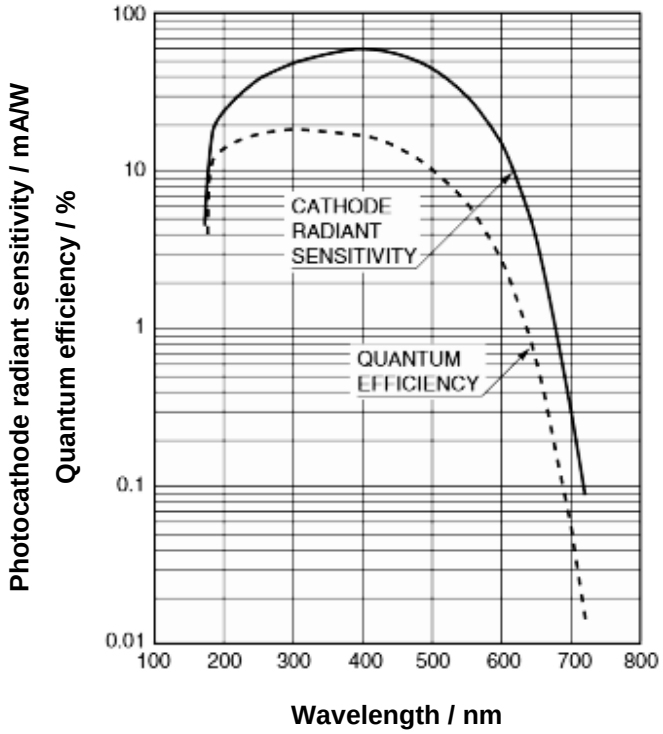

Figure A. 2 Responsivity and quantum efficiency of the PMT as a function of wavelength (as provided by the manufacturer).

Appendix A.3 Spectrometer

The CCD spectrometer employed in the project is a Thorlabs CCS200/M fiber-based, compact size Czerny-Turner spectrometer operational in the wavelength range 200 – 1000 nm. The grating in the spectrometer has 600 lines/mm (800 nm blaze wavelength). The CCD

sensor in the spectrometer has a resolution of 4 px/nm and a sensitivity of 160 V/(lx.s). This spectrometer can be connected to the PC and used via Thorlabs Optical Spectrum Analyzer (OSA) software package. Figure A. 3 shows the overall sensitivity of the spectrometer in the wavelength range 200 – 1000 nm as obtained from Thorlabs.

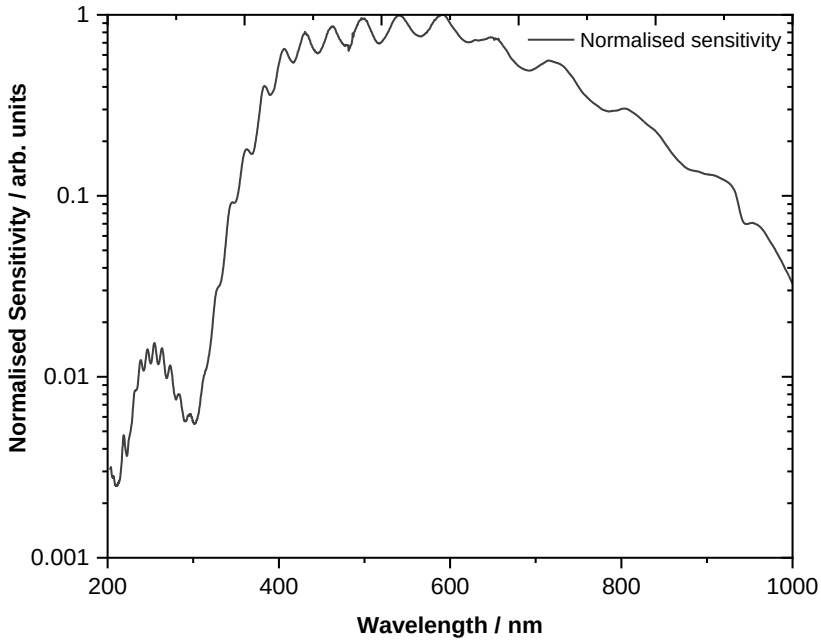

Figure A. 3 Normalised sensitivity of the CCS200/M spectrometer employed in this project (as provided by the manufacturer).

Appendix A.4 Monochromator

The monochromator was chosen considering the compact size and cost-effectiveness of the portable device. The monochromator used is a compact manual Mini-Chrom (Model 37-597, Edmund Optics) with dimensions 139 x 59 x 49 mm and weighing only about 0.7 kg. The monochromator can be used in the wavelength range of 200 – 800 nm. The wavelength selection is achieved by using the knob dial on the Mini-Chrom that rotates the diffraction grating, positioning the chosen wavelength at the exit slit. The slit set chosen has a width of 600 μm which results in a spectral resolution of ~4.4 nm (as per manufacturer specifications). The monochromator encloses an in-line Fastie-Ebert optical layout (as shown in Figure A. 4) with resolution, throughput, stray light and power handling characteristics comparable to many conventional, bulkier, more expensive models. The grating contained within the system is a

2 cm^2 square shaped, $AlMgF_2$ coated holographic, with a grating density of 1800 grooves/mm. The grating efficiency provided by the manufacturer is shown in Figure A. 5 [146].

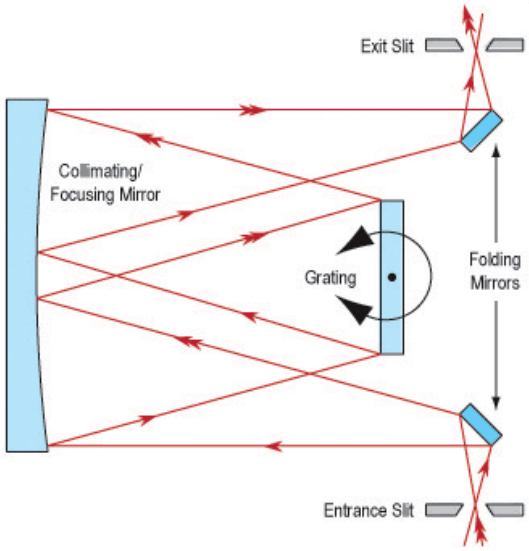

Figure A. 4 In-line Fastie-Ebert optical layout of the manual Mini-Chrom monochromator employed in this project (provided by the manufacturer) [146].

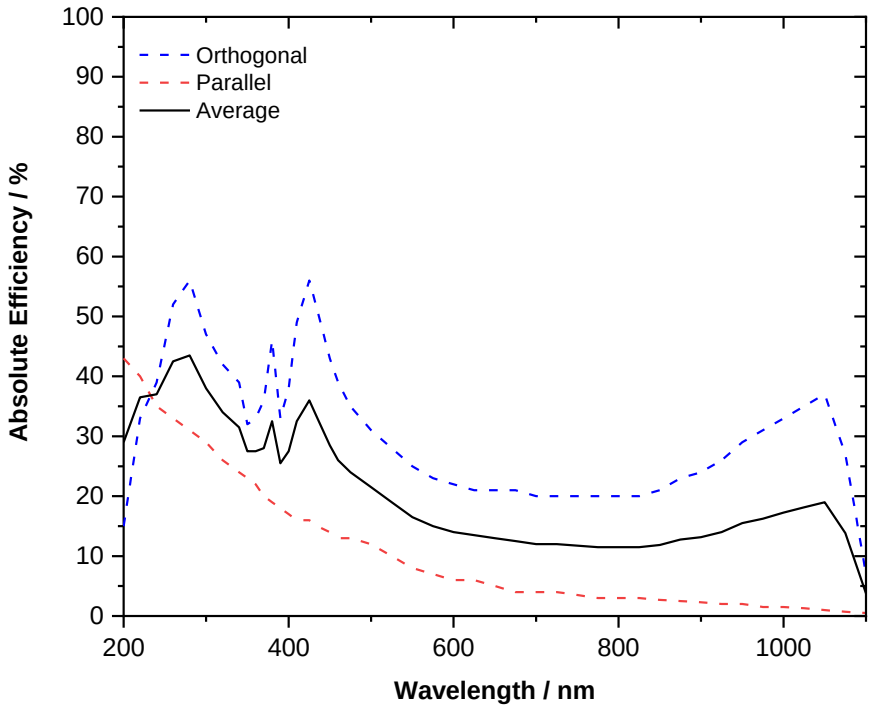

Figure A. 5 Grating efficiency curve of the manual Mini-Chrom monochromator for different polarisations. The incoherent light source in this project would correspond to the black curve with an efficiency of 38 % at 300 nm.

Appendix A.5 Cavity Mirrors

The cavity mirrors forming the optical cavity were plano-concave (Ø25 mm) mirrors with high reflectivity between 273 – 323 nm. The mirrors are made of excimer-grade UV fused silica with dielectric reflective coating. Figure A. 6 (a) and (b) display the reflectivity and transmission curves of the cavity mirrors as provided by the manufacturer (Layertec). The average reflectivity (%R/100) and transmission (%T/100) for wavelength range 292 – 302 nm used in this project are 0.99947 and 2.4 x 10^{-4} respectively.

(a)

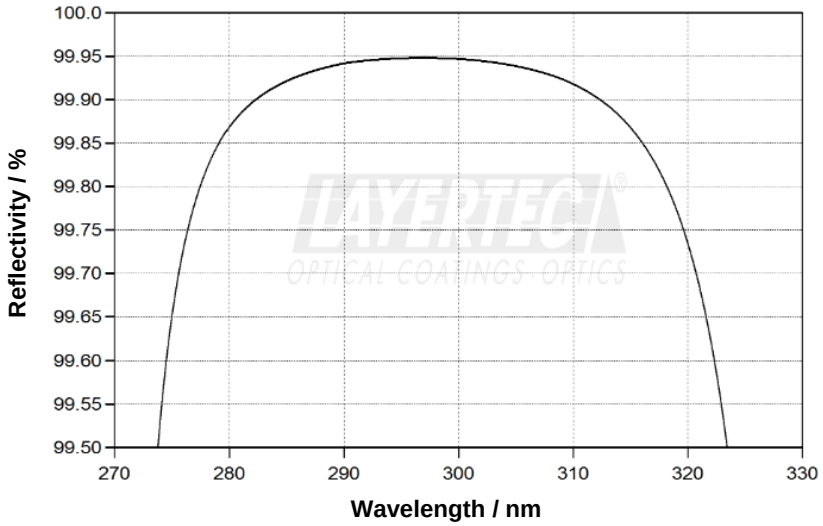

(b)

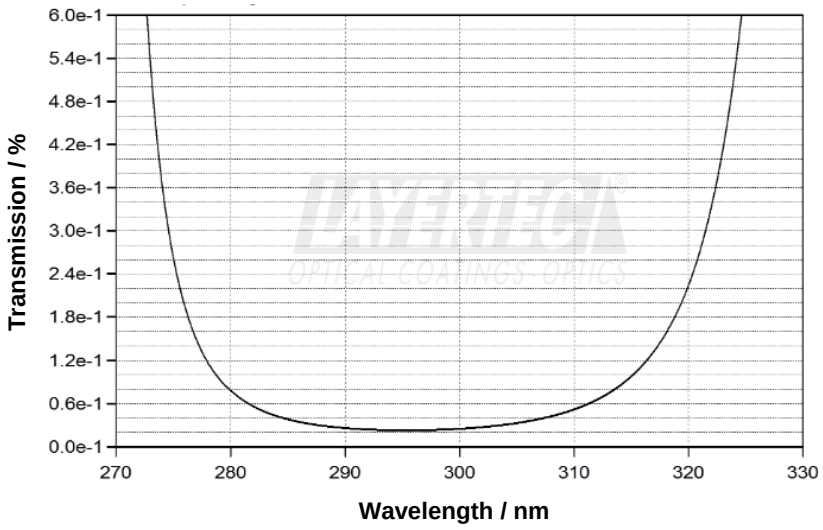

Figure A. 6 (a) Reflectivity curve and (b) Transmission curve of the cavity mirrors employed in the CEAS experimental set-up in this project (provided by the manufacturer).

Appendix A.6 Optical Filter

The optical filter FF01-302/10-25, Semrock chosen for spectral filtering of the LED output was a single- band bandpass filter in the 297 – 307 nm region. The transmission curve obtained from the manufacturer is shown in Figure A. 7.

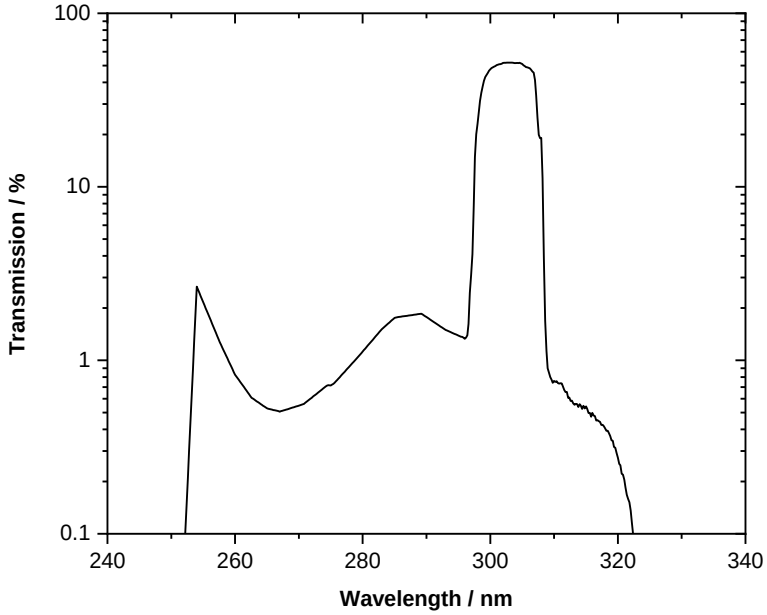

Figure A. 7 Transmission curve of the optical filter (FF01-302/10-25, Semrock) used in the simulations (provided by the manufacturer).

Appendix B LED output intensity

The output of 300 nm LED at its maximum current (350 mA) is monitored over time. Stray light from the optical set-up that is reflected off the entrance cavity mirror is picked by the photodiode to monitor the intensity of light entering the cavity. The background levels of light on the PMT and the photodiode were measured by blocking the light after the monochromator exit. The LED output intensities for the 100 sets of measurements carried out over a duration of about 2 hours are shown in the Figure B. 1. The intensities of the LED light and the light transmitted through the empty cavity were measured simultaneously over the duration of these measurements.

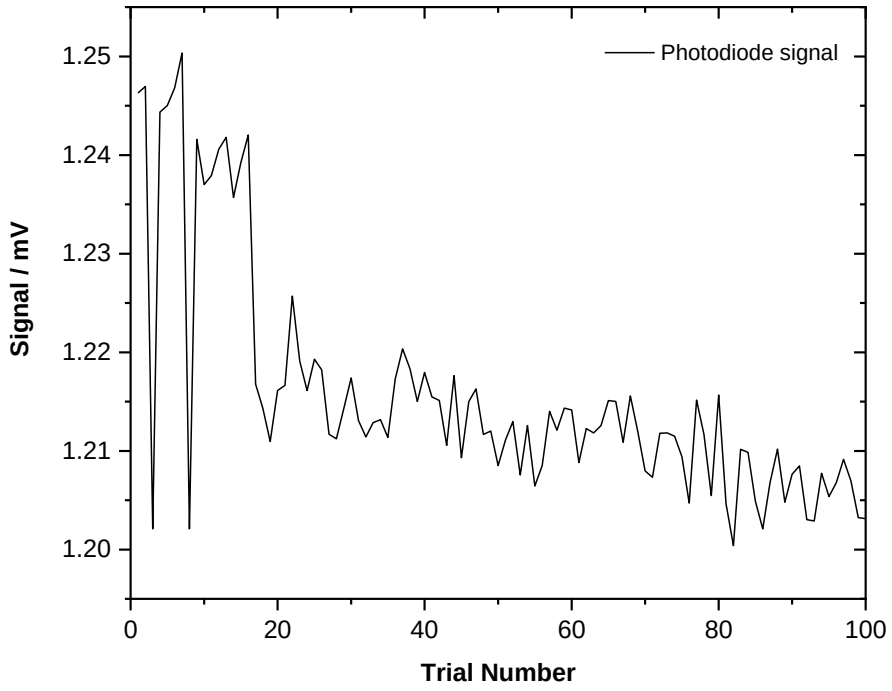

Figure B. 1 LED output intensity varying over time as measured with a photodiode (that captures the stray light that is reflected off the entrance cavity mirror).

The intensity of light transmitted through the empty cavity measured (with the PMT) over the same duration of the measurements is shown in Figure B. 2.

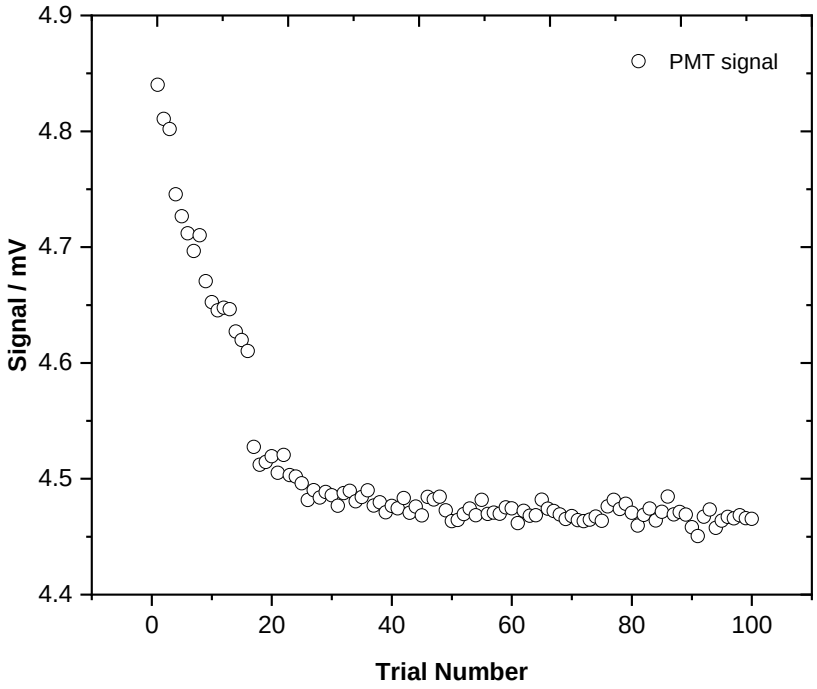

Figure B. 2 The intensity of light transmitted through the optical cavity varying over time as measured with the PMT.

From Figures B.1 and B.2, it is seen that the LED output becomes stable around the 40th measurement which is ~ 45 minutes into the experiment. Hence, in order to get stable light output it would be best to keep the LED on for at least an hour before carrying out any measurements. This also shows that the LED intensity should be monitored over the period of measurements and be used to normalise the cavity output intensity (measured with the PMT).

Appendix C Preliminary tests for N_2/He Rayleigh Scattering

Appendix C.1 N_2/He Test Measurement

The introduction of the gases into the chamber was done as explained in section 5.1.2.1. Rayleigh scattering measurements were carried out for 1000 mbar of N_2 and 1000 mbar of He in the chamber. Using Equation 12, $(1 - R)$ was calculated from the normalised intensities for N_2 and He. This was repeated three times and the resulting $(1 - R)$ values obtained were 2.53 x 10^{-3}, 3.22 x 10^{-3} and 3.07 x 10^{-3}. These values indicated that $(1 - R)$ values had an overall uncertainty of ~12 %. The uncertainty on temperature and pressure were 1.4 % and 0.27 % respectively. Whereas, the intensity ratio I_{N_2}/I_{He} had an uncertainty of ~0.5 % and the intensity difference $I_{He} - I_{N_2}$ had an uncertainty of ~13 % and is the major contributor to the total error on $(1 - R)$. This error is quite large and hence to minimise the error further investigations were carried out. First, the PMT and photodiode (PD) operating at low bias (290 V and 26 V respectively) were investigated to check if they contributed towards the error in intensity measurements. To do this, PMT and PD were operated at slightly higher bias voltage than before and intensities were measured (for an empty cavity).

		Relative standard deviations x 10^{-2}	
		Intensity at cavity exit (PMT)	Ingoing intensity (PD)
A	PMT 555 V PD 29 V	5.87	13.8
B	PMT 310 V PD 26 V	5.45	5.92
C	PMT 310 V PD 26.6 V	1.39	3.05

Table C. 1 Relative standard deviations for PMT and PD signals obtained for different bias voltage settings.

From Table C. 1 it can be seen that although the relative standard deviations for case A and B of the PMT are almost the same, it should not matter much if the PMT is operated at 555 V or 310 V. But operating the PMT at 555 V will need the use of a neutral density (ND) filter to attenuate the signal and this filter being reflective in nature will result in interference/cavity effects. This effect was observed even though the PMT was placed at a slightly angled position

(to reduce this effect) and therefore this set-up makes it more challenging to capture most of the light exiting the cavity. In the case of the PD, lower relative standard deviation was observed in case C while operating at 26.6 V than at other bias voltages. Hence, in order to minimise the errors on intensity measurements the PMT and PD will be operated at 310 V and 26.6 V respectively for the Rayleigh scattering and absorption measurements in this project.

Appendix C.2 Stability of N_2 Background

In order to check the stability of the N_2 background ~1000 mbar of N_2 was filled into the chamber. After letting the gas to equilibrate for ~2 mins intensity measurements were carried out at an interval of 5 minutes. The intensities of the LED light (stray light reflected off the entrance cavity mirror, I_{in}) and the light transmitted through the optical cavity (I) were measured with the photodiode and the PMT respectively. In total, 16 trials (each trial with 32 traces) were conducted with background measurement of light levels in the absence of the light source carried out at intervals of 15 minutes.

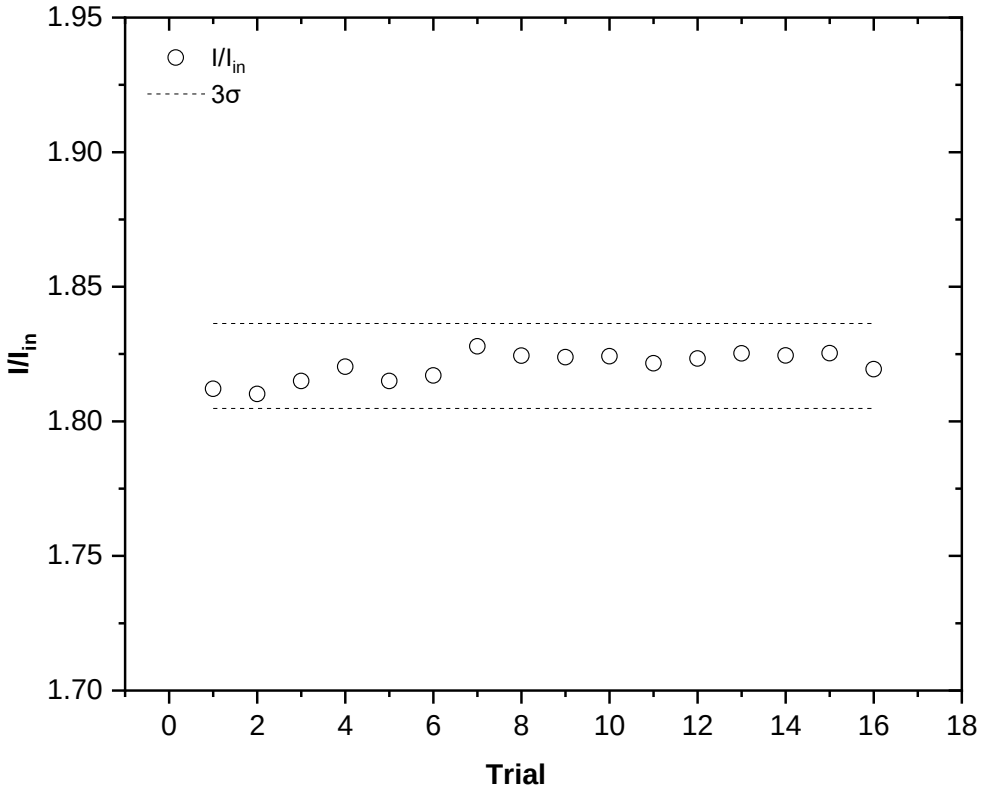

Figure C. 1 Normalised intensity I/I_{in} measured at an interval of 5 minutes for chamber filled with ~1000 mbar N_2.

Here, although the normalised intensities (I/I_{in}) are within the 3σ of the sample mean, the measurements have an overall uncertainty of ~0.3 %. The pressure readings decreased by only ~0.03 % over this time period of measurements which ruled out any capacitance manometer fluctuations and gas diffusion. In Figure C. 1 it is seen that there are some variations in the intensity values around the 7th trial. In order to investigate the error in intensities, tests were carried out with the PMT being used to measure the cavity output.

Appendix C.3 PMT Test

In this project, a PMT was used to measure a continuous optical cavity output as opposed to conventional pulsed methods. The following test was carried out to investigate the behaviour of the PMT towards measuring a continuous output signal. From Appendix B it was concluded that the LED needs to be kept on for ~1 hour in order to obtain a stable output. In this test, the PMT was also kept on at a set bias voltage with cavity output being incident on it continuously for ~1 hour. The chamber was filled with 1000 mbar N_2. The background levels of light on the PMT and the photodiode (PD) in the absence of the light source were measured simultaneously as before. After the wait time, 32 sets (each set with 32 traces i.e., 320128 data points) of data were captured. The plot of the PMT signal against time is as shown in Figure C. 2. From Figure C. 2 it is seen that the PMT shows a drift with time (slope = 1.08 ± 0.4 x 10^{-4} mVs^{-1}) and the PMT signals have an uncertainty of ~0.3 %. Therefore, the normalised intensity (I/I_{in}) with respect to input light (I_{in} – measured with the PD) had an uncertainty of ~0.8 %.

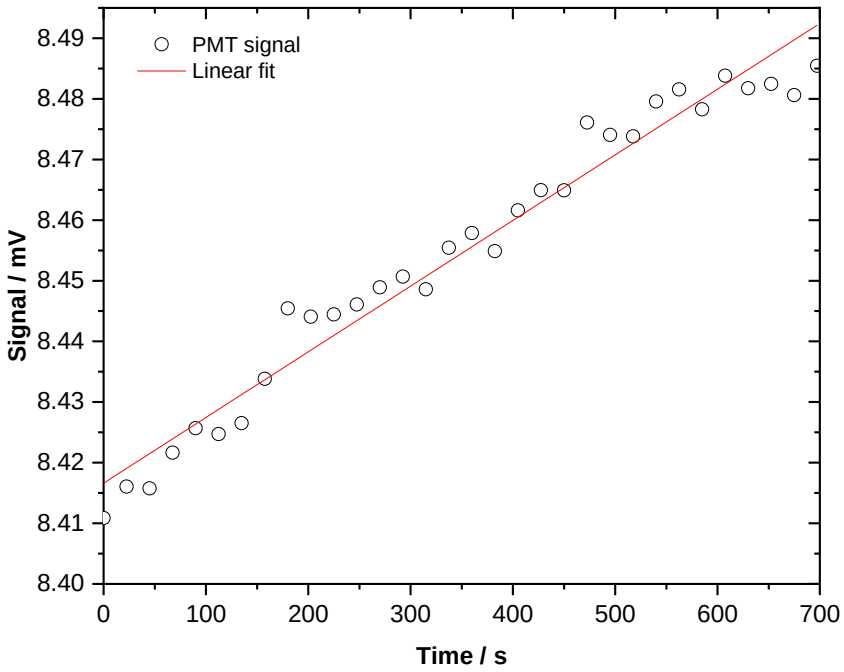

Figure C. 2 The PMT signal (I) against time over which the PMT signal was monitored to check for any drift in the PMT signal being measured. A drift with time is observed in the measured signal which is indicated by its slope $1.08 \pm 0.4 \times 10^{-4}$ mVs^{-1}.

Next, the incident light was blocked from reaching the PMT (laboratory lights were also switched off) and after ~ 30 mins wait time another set of measurement was carried out. The background levels of light on the PMT in the absence of the light source were measured before starting the output intensity measurements.

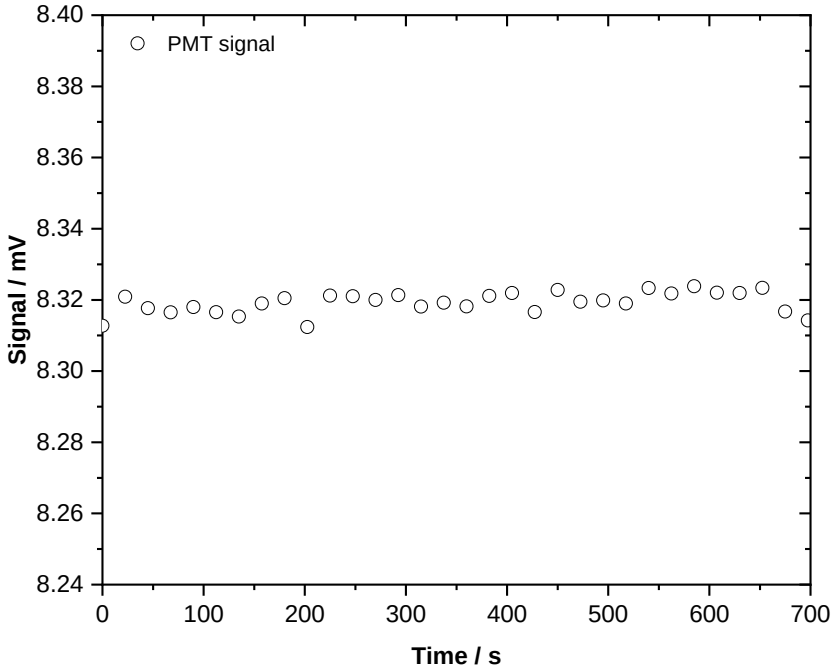

Figure C. 3 The PMT signal (I) against time over which the PMT signal was monitored again after the LED light was blocked from reaching the PMT for ~30 mins. Compared to Figure C. 2, there is effectively no trend observed in the output signal.

From Figure C. 3 it is observed that the PMT signal does not show any trend in comparison to earlier measurement seen in Figure C. 2. The signals measured here have an uncertainty of ~0.04 % which is an order of magnitude lower than seen in the case of Figure C. 2. And the resulting normalised intensities (I/I_{in}) have an uncertainty of ~0.1 %. This set of measurement also indicated that the drift did not continue to occur even after the PMT was blocked from incident light.

Next, the PMT was not blocked from incident light after the last measurement for ~45 mins. The background levels on light on the PMT was measured as before and another set of intensity measurement was carried out to check if any drift occurred again.

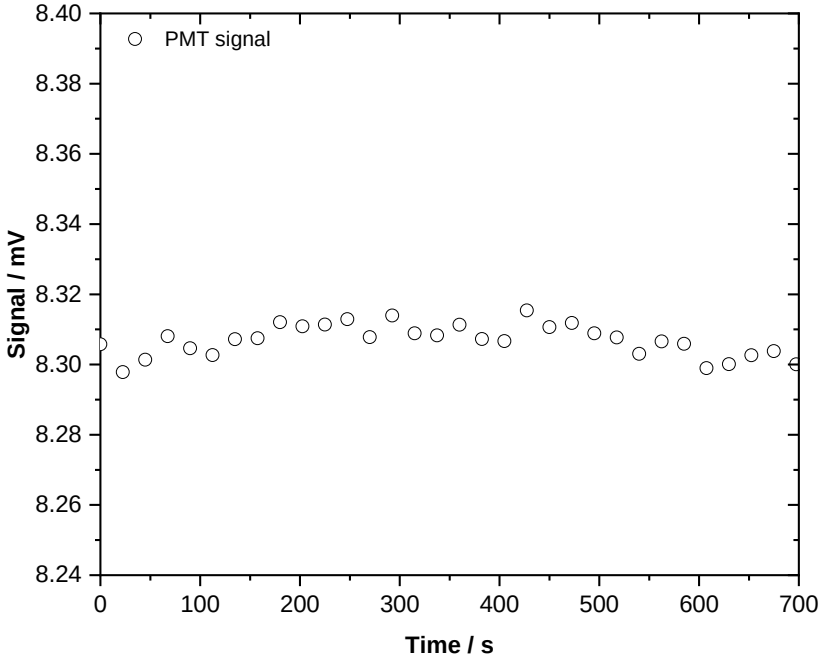

Figure C. 4 PMT signal (I) against time. The PMT signal was monitored to check for any drift after the PMT was not blocked from incident light for ~45 mins after the last measurement seen in Figure C. 3. It can be seen that there is no definite trend in the output signal.

In Figure C. 4 it is seen that the PMT does not show a drift as observed previously in the case of Figure C. 2 and that it does not have a definite trend. Here, the PMT signals have an uncertainty of ~0.05 % which is an order of magnitude lower than in the case of Figure C. 2. The resulting normalised intensities (I/I_{in}) have an uncertainty of ~0.07 % which is also an order of magnitude lower to that observed in Figure C. 2. Therefore, from the timeline of the experiment the PMT shows to have reached a stable state after ~2 hours. Hence, in order to avoid any drifts in intensity measurements it would be ideal to switch on the LED and PMT with light continuously being incident on the PMT (cavity output) and wait ~2 hours before carrying out any measurements to allow enough time for the PMT to equilibrate. The experimental protocol for N_2/He measurements would require carrying them out in the order N_2, He and N_2 (capturing 32 sets of data for each gas) so that any long-term drift if present is compensated by the averaged I_{N_2}.

Appendix D Error Propagation

Temperature:

The thermocouples used in this project have an error of 1 % on the reading as per manufacturer specification ($\sigma_{reading}$) The temperatures were recorded using two thermocouples, each attached to the cavity arms. The two readings T_1 and T_2 were averaged (T_{avrg}) and the standard deviation (σ_{avrg}) on the average temperature was determined. The error on the reading was applied twice to account for the two thermocouple readings.

$$T = T_{avrg} \pm \sqrt{\sigma_{avrg}^2 + 2(\sigma_{reading})^2} \quad (32)$$

Pressure:

The pressures were read by eye from the capacitance manometer that has 0.25 % error on the reading as per manufacturer specification ($\sigma_{reading}$). Considering the ± 1 mbar error with reading pressure and the error on the reading, the total error on the pressures were

$$\sigma_{pressure} = \sqrt{1 + (\sigma_{reading})^2} \quad (33)$$

Error propagation:

The error propagation was carried out using the formula:

$$\sigma_Q^2 = \sum_i \left(\frac{\partial Q(x_i)}{\partial x_i}\right)^2 \sigma_{x_i}^2 \quad (34)$$

where Q is the quantity and x_i is a variable Q depends on and $\sigma_{x_i}$is the error associated with the variable x_i.

The uncertainty in a variable is determined as $\left(\frac{\sigma_{x_i}}{x_i}\right)$ x 100 % .

References

[1] P. Atkins and J. de Paula, *Physical Chemistry*, 8th ed. New York: W. H. Freeman and Company, 2006.

[2] N. J. Turro, *Modern molecular photochemistry*. University Science Books, 1991.

[3] A. Nano, "Towards optical memories : switchable optical systems for electron and energy," University of Strasbourg, 2015.

[4] C. W. Porter, C. Iddings, and V. 48, "The absorption spectrum and the photochemical decomposition of acetone," *J. Am. Chem. Soc.*, vol. 48, no. 1, pp. 40–44, 1926.

[5] G. H. Damon and F. Daniels, "The photolysis of gaseous acetone and the influence of water," *J. Am. Chem. Soc.*, vol. 55, no. 6, pp. 2363–2375, 1933.

[6] P. F. Bernath, *Spectra of atoms and molecules*, 3rd ed. Oxford University Press, 2016.

[7] W. H. Reusch, *An introduction to organic chemistry*. Holden Day, 1977.

[8] C. Schulz and V. Sick, "Tracer-LIF diagnostics: quantitative measurement of fuel concentration, temperature and fuel/air ratio in practical combustion systems," *Prog. Energy Combust. Sci.*, vol. 31, no. 1, pp. 75–121, Jan. 2005.

[9] H. Keller-Rudek, G. K. Moortgat, R. Sander, and R. Sörensen, "The MPI-Mainz UV/VIS spectral atlas of gaseous molecules of atmospheric interest," *Earth Syst. Sci. Data*, vol. 5, no. 2, pp. 365–373, Dec. 2013.

[10] H. H. Jaffe and A. L. Miller, "The fates of electronic excitation energy," *J. Chem. Educ.*, vol. 43, no. 9, p. 469, 1966.

[11] T. Gierczak, J. B. Burkholder, S. Bauerle, and A. R. Ravishankara, "Photochemistry of acetone under tropospheric conditions," *Chem. Phys.*, vol. 231, pp. 229–244, 1998.

[12] M. A. Blitz, D. E. Heard, and M. J. Pilling, "Study of acetone photodissociation over the wavelength range 248-330 nm: Evidence of a mechanism involving both the singlet and triplet excited states," *J. Phys. Chem. A*, vol. 110, pp. 6742–6756, 2006.

[13] A. Horowitz, "Wavelength dependence of the primary photodissociation processes in acetone photolysis," *J. Phys. Chem.*, vol. 95, no. 26, pp. 10816–10823, 1991.

[14] J. W. Strutt, “XV.On the light from the sky, its polarization and colour,” *London, Edinburgh, Dublin Philos. Mag. J. Sci.*, vol. 41, no. 271, pp. 107–120, 1871.

[15] Lord Rayleigh, “XXXIV. On the transmission of light through an atmosphere containing small particles in suspension, and on the origin of the blue of the sky,” *London, Edinburgh, Dublin Philos. Mag. J. Sci.*, vol. 47, no. 287, pp. 375–384, 1899.

[16] L. V. King, “The complex anisotropic molecule in relation to the theory of dispersion and scattering of light in gases and liquids,” *Nature*, vol. 111, no. 2794, pp. 667–667, May 1923.

[17] D. R. Bates, “Rayleigh scattering by air,” *Planet. Space Sci.*, vol. 32, no. 6, pp. 785–790, 1984.

[18] A. Bucholtz, “Rayleigh-scattering calculations for the terrestrial atmosphere,” *Appl. Opt.*, vol. 34, no. 15, pp. 2765–2773, 1995.

[19] P. M. Teillet, “Rayleigh optical depth comparisons from various sources,” *Appl. Opt.*, vol. 29, no. 13, pp. 1897–1900, 1990.

[20] D. Ityaksov, H. Linnartz, and W. Ubachs, “Deep-UV Rayleigh scattering of N_2, CH_4 and SF_6,” *Mol. Phys.*, vol. 106, pp. 2471–2479, 2008.

[21] D. J. Jacob *et al.*, “Atmospheric budget of acetone,” *J. Geophys. Res. Atmos.*, vol. 107, pp. D9–D10, 2002.

[22] F. Arnold, V. Bürger, F. Grimm, A. Krieger, J. Schneider, and T. Stilp, “Acetone in the upper troposphere and lower stratosphere: Impact on trace gases and aerosols,” *Geophys. Res. Lett.*, vol. 24, no. 23, pp. 3017–3020, 1997.

[23] D. Sprung and A. Zahn, “Acetone in the upper troposphere/lowermost stratosphere measured by the CARIBIC passenger aircraft: Distribution, seasonal cycle, and variability,” *J. Geophys. Res. Atmos.*, vol. 115, no. 16, pp. 1–12, 2010.

[24] I. Folkins, R. Chatfield, H. Singh, Y. Chen, and B. Heikes, “Ozone production efficiencies of acetone and peroxides in the upper troposphere,” *Geophys. Res. Lett.*, vol. 25, no. 9, pp. 1305–1308, 1998.

[25] P. O. Wennberg *et al.*, “Hydrogen radicals, nitrogen radicals, and the production of O_3 in the upper troposphere,” *Science (80-.).*, vol. 279, no. 5347, pp. 49–53, 1998.

[26] H. B. Singh, M. Kanakidou, P. J. Crutzen, and D. J. Jacob, “High concentrations and photochemical fate of oxygenated hydrocarbons in the global troposphere,” *Nature*, vol. 378, no. 6552, pp. 50–54, 1995.

[27] R. A. Gelfand and R. S. Sherwin, “Glucagon and Starvation,” in *Glucagon II. Handbook of experimental pharmacology (Continuation of Handbuch der experimentellen Pharmakologie)*, Springer, Berlin, Heidelberg,, pp. 223–237, 1983.

[28] R. A. DeFronzo, F. E. Paul, and G. Alberti, *International textbook of diabetes mellitus*, 4th ed. John Wiley & Sons.

[29] L. Laffel, “Ketone bodies: a review of physiology, pathophysiology and application of monitoring to diabetes,” *Diabetes. Metab. Res. Rev.*, vol. 15, no. 6, pp. 412–26, 1999.

[30] P. Arner, “Human fat cell lipolysis: Biochemistry, regulation and clinical role,” *Best Pract. Res. Clin. Endocrinol. Metab.*, vol. 19, no. 4, pp. 471–482, 2005.

[31] N. J. Grey, I. Karl, and D. M. Kipnis, “Physiologic mechanisms in the development of starvation ketosis in man,” *Diabetes*, vol. 24, no. 1, pp. 10–16, Jan. 1975.

[32] M. P. Kalapos, “On the mammalian acetone metabolism: from chemistry to clinical implications,” *Biochim. Biophys. Acta*, vol. 1621, no. 2, pp. 122–39, May 2003.

[33] J. C. Anderson, “Measuring breath acetone for monitoring fat loss: Review.,” *Obesity (Silver Spring).*, vol. 23, no. 12, pp. 2327–34, Dec. 2015.

[34] D. R. Whiting, L. Guariguata, C. Weil, and J. Shaw, “IDF Diabetes Atlas: Global estimates of the prevalence of diabetes for 2011 and 2030,” *Diabetes Res. Clin. Pract.*, vol. 94, no. 3, pp. 311–321, Dec. 2011.

[35] M. P. Kalapos, “Possible physiological roles of acetone metabolism in humans,” *Med. Hypotheses*, vol. 53, no. 3, pp. 236–242, Sep. 1999.

[36] World Health Organization, “Definition, diagnosis and classification of diabetes mellitus and its complications. Part 1: Diagnosis and classification of diabetes mellitus. WHO/NCD/NCS/99.2.” World Health Organization, Geneva, 1999.

[37] M. F. Delaney, A. Zisman, and W. M. Kettyle, “Diabetic ketoacidosis and hyperglycemic hyperosmolar nonketotic syndrome,” *Endocrinol. Metab. Clin. North Am.*, vol. 29, no. 4, pp. 683–705, Dec. 2000.

[38] M. W. Savage *et al.*, “Joint British Diabetes Societies guideline for the management of diabetic ketoacidosis,” *Diabet. Med.*, vol. 28, no. 5, pp. 508–515, 2011.

[39] L. Pauling, A. B. Robinson, R. Teranishi, and P. Cary, “Quantitative analysis of urine vapor and breath by gas-liquid partition chromatography,” *Proc. Natl. Acad. Sci.*, vol. 68, no. 10, pp. 2374–2376, Oct. 1971.

[40] G. Berden and R. Engeln, *Cavity ring-down spectroscopy : techniques and applications*. Wiley, 2009.

[41] J. K. Schubert, W. P. Müller, A. Benzing, and K. Geiger, “Application of a new method for analysis of exhaled gas in critically ill patients.,” *Intensive Care Med.*, vol. 24, no. 5, pp. 415–21, May 1998.

[42] T. H. Risby and S. F. Solga, “Current status of clinical breath analysis,” *Appl. Phys. B*, vol. 85, no. 2–3, pp. 421–426, Nov. 2006.

[43] J. Rollo, *Cases of the diabetes mellitus, with the results of the trials of certain acids and other substances in the cure of the lues venerea*, 2nd ed. London: T. Gillet, 1798.

[44] V. Ruzsányi and M. P. Kalapos, “Breath acetone as a potential marker in clinical practice,” *J. Breath Res*, vol. 11, p. 024002 (18pp), 2017.

[45] M. D. Trotter, M. J. Sulway, and E. Trotter, “The rapid determination of acetone in breath and plasma.,” *Clin. Chim. Acta.*, vol. 35, no. 1, pp. 137–43, Nov. 1971.

[46] J. D. Pleil and A. B. Lindstrom, “Measurement of volatile organic compounds in exhaled breath as collected in evacuated electropolished canisters,” *J. Chromatogr. B Biomed. Sci. Appl.*, vol. 665, no. 2, pp. 271–279, Mar. 1995.

[47] J. King *et al.*, “Physiological modeling of isoprene dynamics in exhaled breath,” *J. Theor. Biol.*, vol. 267, no. 4, pp. 626–637, 2010.

[48] J. F. Dummer *et al.*, “Accurate, reproducible measurement of acetone concentration in breath using selected ion flow tube-mass spectrometry,” *J. Breath Res.*, vol. 4, no. 4, p. 8, 2010.

[49] V. Ruzsanyi, J. I. Baumbach, S. Sielemann, P. Litterst, M. Westhoff, and L. Freitag, “Detection of human metabolites using multi-capillary columns coupled to ion mobility spectrometers,” *J. Chromatogr. A*, vol. 1084, no. 1, pp. 145–151, 2005.

[50] R. Centeno *et al.*, “Influence of ethanol on breath acetone measurements using an external cavity quantum cascade laser,” *Photonics*, vol. 3, no. 2, p. 22, Apr. 2016.

[51] C. Jiang *et al.*, “A portable real-time ringdown breath acetone analyzer: Toward potential diabetic screening and management,” *Sensors*, vol. 16, no. 8, p. 1199, 2016.

[52] T. P. J. Blaikie *et al.*, “Portable device for measuring breath acetone based on sample preconcentration and cavity enhanced spectroscopy,” *Anal. Chem.*, vol. 88, no. 22, pp. 11016–11021, 2016.

[53] M. Righettoni, A. Tricoli, S. Gass, A. Schmid, A. Amann, and S. E. Pratsinis, “Breath acetone monitoring by portable Si:WO_3 gas sensors,” *Anal. Chim. Acta*, vol. 738, pp. 69–75, Aug. 2012.

[54] J. Li, T. M. Smeeton, M. Zanola, J. Barrett, and V. Berryman-Bousquet, “A compact breath acetone analyser based on an ultraviolet light emitting diode,” *Sensors Actuators B Chem.*, vol. 273, pp. 76–82, 2018.

[55] B. J. Finlayson-Pitts and J. N. Pitts, *Chemistry of the upper and lower atmosphere : theory, experiments, and applications*. San Diago: Academic Press, 2000.

[56] U. Platt and J. Stutz, *Differential Optical Absorption Spectroscopy: Principles and Applications*. Springer, Berlin, Heidelberg, 2008.

[57] D. R. Herriott and H. J. Schulte, “Folded optical delay lines,” *Appl. Opt.*, vol. 4, no. 8, pp. 883–889, 1965.

[58] J. U. White, “Long optical paths of large aperture,” *J. Opt. Soc. Am.*, vol. 32, no. 5, pp. 285–288, May 1942.

[59] U. Platt, “Modern methods of the measurement of atmospheric trace gases,” *Phys. Chem. Chem. Phys.*, vol. 1, no. 24, pp. 5409–5415, 1999.

[60] F. J. M. Harren, F. G. C. Bijnen, J. Reuss, L. A. C. J. Voesenek, and C. W. P. M. Blom, “Sensitive intracavity photoacoustic measurements with a CO_2 waveguide laser,” *Appl. Phys. B Photophysics Laser Chem.*, vol. 50, no. 2, pp. 137–144, Feb. 1990.

[61] W. J. Tango, J. K. LinK, and R. N. Zare, “Spectroscopy of K_2 using Laser-Induced Fluorescence,” *J. Chem. Phys.*, vol. 49, no. 10, pp. 4264–4268, 1968.

[62] R. N. Zare, “My Life with LIF: A personal account of developing laser-induced fluorescence,” *Annu. Rev. Anal. Chem*, vol. 5, pp. 1–14, 2012.

[63] W. Demtröder, *Laser spectroscopy : basic concepts and instrumentation*. Springer, Berlin, 2003.

[64] A. O’Keefe and D. A. G. Deacon, “Cavity ring-down optical spectrometer for absorption measurements using pulsed laser sources,” *Rev. Sci. Instrum.*, vol. 59, no. 12, pp. 2544–2551, 1988.

[65] G. Berden, R. Peeters, and G. Meijer, “Cavity ring-down spectroscopy: Experimental schemes and applications,” *Int. Rev. Phys. Chem.*, vol. 19, no. 4, pp. 565–607, 2000.

[66] R. T. Jongma, M. G. H. Boogaarts, I. Holleman, and G. Meijer, “Trace gas detection with cavity ring down spectroscopy,” *Rev. Sci. Instrum.*, vol. 66, no. 4, pp. 2821–2828, 1995.

[67] C. Vallance, “Innovations in cavity ringdown spectroscopy,” *New J. Chem.*, vol. 29, no. 7, pp. 867–874, 2005.

[68] D. Romanini, A. A. Kachanov, N. Sadeghi, and E. Stoeckel, “CW cavity ring down spectroscopy,” *Chem. Phys. Lett.*, vol. 264, pp. 316–322, 1997.

[69] D. Romanini, A. A. Kachanov, and F. Stoeckel, “Diode laser cavity ring down spectroscopy,” *Chem. Phys. Lett.*, vol. 270, pp. 538–545, 1997.

[70] B. A. Paldus, J. S. Harris, J. Martin, J. Xie, and R. N. Zare, “Laser diode cavity ring-down spectroscopy using acousto-optic modulator stabilization,” *J. Appl. Phys.*, vol. 82, no. 7, pp. 3199–3204, 1997.

[71] S. S. Brown, “Absorption spectroscopy in high-finesse cavities for atmospheric studies,” *Chem. Rev.*, vol. 103, no. 12, pp. 5219–5238, 2003.

[72] A. Czyzewski *et al.*, “Cavity ring-down spectrography,” *Opt. Commun.*, vol. 191, pp. 271–275, 2001.

[73] S. M. Ball and R. L. Jones, “Broad-band cavity ring-down spectroscopy,” *Chem. Rev.*, vol. 103, no. 12, pp. 5239–5262, 2003.

[74] S. M. Ball, I. M. Povey, E. G. Norton, and R. L. Jones, “Broadband cavity ringdown

spectroscopy of the NO_3 radical," *Chem. Phys. Lett.*, vol. 342, pp. 113–120, 2001.

[75] M. Bitter, S. M. Ball, I. M. Povey, and R. L. Jones, "A broadband cavity ringdown spectrometer for in-situ measurements of atmospheric trace gases," *Atmos. Chem. Phys*, vol. 5, pp. 2547–2560, 2005.

[76] S. E. Fiedler, A. Hese, and A. A. Ruth, "Incoherent broad-band cavity-enhanced absorption spectroscopy," *Chem. Phys. Lett.*, vol. 371, no. 3, pp. 284–294, 2003.

[77] S. E. Fiedler, A. Hese, and U. Heitmann, "Influence of the cavity parameters on the output intensity in incoherent broadband cavity-enhanced absorption spectroscopy," *Rev. Sci. Instrum.*, vol. 78, no. 133, p. 073104, 2007.

[78] D. S. Venables, T. Gherman, J. Orphal, J. C. Wenger, and A. A. Ruth, "High sensitivity in situ monitoring of NO_3 in an atmospheric simulation chamber using incoherent broadband cavity-enhanced absorption spectroscopy," *Environ. Sci. Technol.*, vol. 40, no. 21, pp. 6758–6763, 2006.

[79] S. M. Ball, J. M. Langridge, and R. L. Jones, "Broadband cavity enhanced absorption spectroscopy using light emitting diodes," *Chem. Phys. Lett.*, vol. 398, no. 1–3, pp. 68–74, 2004.

[80] T. Gherman, D. S. Venables, S. Vaughan, J. Orphal, and A. A. Ruth, "Incoherent broadband cavity-enhanced absorption spectroscopy in the near-ultraviolet: Application to HONO and NO_2," *Environ. Sci. Technol.*, vol. 42, no. 3, pp. 890–895, 2008.

[81] L. Biennier, F. Salama, M. Gupta, and A. O'Keefe, "Multiplex integrated cavity output spectroscopy of cold PAH cations," *Chem. Phys. Lett.*, vol. 387, pp. 287–294, 2004.

[82] T. Gherman, S. Kassi, A. Campargue, and D. Romanini, "Overtone spectroscopy in the blue region by cavity-enhanced absorption spectroscopy with a mode-locked femtosecond laser: application to acetylene," *Chem. Phys. Lett.*, vol. 383, pp. 353–358, 2004.

[83] A. A. Ruth, J. Orphal, and S. E. Fiedler, "Fourier-transform cavity-enhanced absorption spectroscopy using an incoherent broadband light source," *Appl. Opt.*, vol. 46, no. 17, pp. 3611–3616, 2007.

[84] E. R. Crosson *et al.*, "Pulse-stacked cavity ring-down spectroscopy," *Rev. Sci. Instrum.*,

vol. 70, no. 1, pp. 4–10, 1999.

[85] G. A. Marcus and H. A. Schwettman, “Cavity ringdown spectroscopy of thin films in the mid-infrared,” *Appl. Opt.*, vol. 41, no. 24, p. 5167, Aug. 2002.

[86] R. Engeln and G. Meijer, “A Fourier transform cavity ring down spectrometer,” *Rev. Sci. Instrum.*, vol. 67, no. 8, pp. 2708–2713, Aug. 1996.

[87] E. Hamers, D. Schram, and R. Engeln, “Fourier transform phase shift cavity ring down spectroscopy,” *Chem. Phys. Lett.* , vol. 365, pp. 237–243, 2002.

[88] P. L. Kebabian, S. C. Herndon, and A. Freedman, “Detection of nitrogen dioxide by cavity attenuated phase shift spectroscopy,” *Anal. Chem.*, vol. 77, no. 2, pp. 724–728, 2005.

[89] P. L. Kebabian, W. A. Robinson, and A. Freedman, “Optical extinction monitor using cw cavity enhanced detection,” *Cit. Rev. Sci. Instrum*, vol. 78, 2007.

[90] J. J. Scherer, “Ringdown spectral photography,” *Chem. Phys. Lett.*, vol. 292, pp. 143–153, 1998.

[91] J. J. Scherer, J. B. Paul, H. Jiao, and A. O ’Keefe, “Broadband ringdown spectral photography,” *Appl. Opt.*, vol. 40, no. 36, p. 6725, 2001.

[92] M. J. Thorpe, K. D. Moll, R. J. Jones, B. Safdi, and J. Ye, “Broadband cavity ring-down spectroscopy for sensitive and rapid molecular detection,” *Science (80-.).*, vol. 311, no. 5767, pp. 1595–1599, 2006.

[93] G. Gagliardi and H.-P. Loock, Eds., *Cavity-Enhanced Spectroscopy and Sensing*, vol. 179. Springer, Berlin Heidelberg, 2014.

[94] R. Engeln, G. Berden, R. Peeters, and G. Meijer, “Cavity enhanced absorption and cavity enhanced magnetic rotation spectroscopy,” *Rev. Sci. Instrum.*, vol. 69, no. 11, pp. 3763–3769, 1998.

[95] A. O’Keefe, “Integrated cavity output analysis of ultra-weak absorption,” *Chem. Phys. Lett.*, 1998.

[96] T. Gherman, E. Eslumi, N. Sadeghi, and D. Romanini, “Mode-locked cavity-enhanced absorption spectroscopy,” in *Quantum Electronics Conference, 2003. EQEC ’03*, 2003,

p. 248.

[97] J. Chen and D. S. Venables, “A broadband optical cavity spectrometer for measuring weak near-ultraviolet absorption spectra of gases,” *Atmos. Meas. Tech.*, vol. 4, no. 3, pp. 425–436, 2011.

[98] M. Bass *et al.*, Eds., *Handbook of optics*, Third., vol. 2. McGraw-Hill, 2010.

[99] S. Nakamura, T. Mukai, and S. Masayuki, “High-Power GaN P-N Junction Blue-Light-Emitting Diodes,” *Jpn. J. Appl. Phys.*, vol. 30, no. 12A, pp. L1998–L2001, 1991.

[100] J. Chen, S. Loeb, and J. H. Kim, “LED revolution: fundamentals and prospects for UV disinfection applications,” *Environ. Sci. Water Res. Technol.*, vol. 3, no. 2, pp. 188–202, 2017.

[101] K. Oguma, R. Kita, H. Sakai, M. Murakami, and S. Takizawa, “Application of UV light emitting diodes to batch and flow-through water disinfection systems,” *Desalination*, vol. 328, pp. 24–30, 2013.

[102] W. S. Won *et al.*, “UV-LEDs for the disinfection and bio-sensing applications,” *Int. J. Precis. Eng. Manuf.*, vol. 19, no. 12, pp. 1901–1915, 2018.

[103] V. Landry, P. Blanchet, G. Boivin, J. F. Bouffard, and M. Vlad, “UV-LED curing efficiency of wood coatings,” *Coatings*, vol. 5, no. 4, pp. 1019–1033, 2015.

[104] A. Suthaparan *et al.*, “Suppression of powdery mildew (Podosphaera pannosa) in greenhouse roses by brief exposure to supplemental UV-B radiation,” *Plant Dis.*, vol. 96, no. 11, pp. 1653–1660, 2012.

[105] S. M. Ball, J. M. Langridge, and R. L. Jones, “Broadband cavity enhanced absorption spectroscopy using light emitting diodes,” *Chem. Phys. Lett.*, vol. 398, no. 1, pp. 68–74, 2004.

[106] J. M. Langridge, S. M. Ball, and R. L. Jones, “A compact broadband cavity enhanced absorption spectrometer for detection of atmospheric NO_2 using light emitting diodes,” *Analyst*, vol. 131, no. 8, pp. 916–922, 2006.

[107] M. Triki, P. Cermak, G. Méjean, and D. Romanini, “Cavity-enhanced absorption spectroscopy with a red LED source for NO_x trace analysis,” *Appl. Phys. B Lasers Opt.*, vol. 91, no. 1, pp. 195–201, 2008.

[108] I. Ventrillard-Courtillot, E. Sciamma O'Brien, S. Kassi, G. Méjean, and D. Romanini, "Incoherent broad-band cavity-enhanced absorption spectroscopy for simultaneous trace measurements of NO_2 and NO_3 with a LED source," *Appl. Phys. B Lasers Opt.*, vol. 101, no. 3, pp. 661–669, 2010.

[109] T. Wu, W. Zhao, W. Chen, W. Zhang, and X. Gao, "Incoherent broadband cavity enhanced absorption spectroscopy for in situ measurements of NO_2 with a blue light emitting diode," *Appl. Phys. B*, vol. 94, no. 1, pp. 85–94, Jan. 2009.

[110] T. Wu, Q. Zha, W. Chen, Z. Xu, T. Wang, and X. He, "Development and deployment of a cavity enhanced UV-LED spectrometer for measurements of atmospheric HONO and NO_2 in Hong Kong," *Atmos. Environ.*, vol. 95, pp. 544–551, 2014.

[111] M. A. Donaldson, A. E. Berke, and J. D. Raff, "Uptake of gas phase nitrous acid onto boundary layer soil surfaces," *Environ. Sci. Technol.*, vol. 48, pp. 375–383, 2014.

[112] N. K. Scharko, A. E. Berke, and J. D. Raff, "Release of nitrous acid and nitrogen dioxide from nitrate photolysis in acidic aqueous solutions," *Environ. Sci. Technol*, vol. 48, pp. 11991–12001, 2014.

[113] K.-E. Min *et al.*, "A broadband cavity enhanced absorption spectrometer for aircraft measurements of glyoxal, methylglyoxal, nitrous acid, nitrogen dioxide, and water vapor," *Atmos. Meas. Tech.*, vol. 9, pp. 423–440, 2016.

[114] Y. Nakashima and Y. Sadanaga, "Validation of in situ measurements of atmospheric nitrous acid using incoherent broadband cavity-enhanced absorption spectroscopy," *Anal. Sci.*, vol. 33, no. 4, pp. 519–524, 2017.

[115] J. Duan *et al.*, "Development of an incoherent broadband cavity-enhanced absorption spectrometer for in situ measurements of HONO and NO_2," *Atmos. Meas. Tech*, vol. 11, pp. 4531–4543, 2018.

[116] N. Jordan and H. D. Osthoff, "Quantification of nitrous acid (HONO) and nitrogen dioxide (NO_2) in ambient air by broadband cavity-enhanced absorption spectroscopy (IBBCEAS) between 361-388 nm," *Atmos. Meas. Tech. Discuss.*, pp. 1–27, 2019.

[117] A. T. M. Wilbers, G. M. W. Kroesen, C. J. Timmermans, and D. C. Schram, "The continuum emission of an arc plasma," *J. Quant. Spectrosc. Radiat. Transf.*, vol. 45, no.

1, pp. 1–10, 1991.

[118] S. Fiedler, A. Hese, and A. A. Ruth, “Incoherent broad-band cavity-enhanced absorption spectroscopy of liquids,” *Rev. Sci. Instrum.*, vol. 76, p. 023107, 2005.

[119] S. E. Fiedler, G. Hoheisel, A. A. Ruth, and A. Hese, “Incoherent broad-band cavity-enhanced absorption spectroscopy of azulene in a supersonic jet,” *Chem. Phys. Lett.*, vol. 382, no. 3–4, pp. 447–453, 2003.

[120] J. Orphal and A. A. Ruth, “High-resolution Fourier-transform cavity-enhanced absorption spectroscopy in the near-infrared using an incoherent broad-band light source,” *Opt. Express*, vol. 16, no. 23, pp. 19232–19243, 2008.

[121] S. Vaughan, T. Gherman, A. A. Ruth, and J. Orphal, “Incoherent broad-band cavity-enhanced absorption spectroscopy of the marine boundary layer species I_2, IO and OIO,” *Phys. Chem. Chem. Phys.*, vol. 10, no. 30, pp. 4471–4477, 2008.

[122] R. A. Washenfelder, A. O. Langford, H. Fuchs, and S. S. Brown, “Measurement of glyoxal using an incoherent broadband cavity enhanced absorption spectrometer,” *Atmos. Chem. Phys. Discuss.*, vol. 8, no. 24, pp. 7779–7793, 2008.

[123] S. Dixneuf, A. A. Ruth, S. Vaughan, R. M. Varma, and J. Orphal, “The time dependence of molecular iodine emission from Laminaria digitata,” *Atmos. Chem. Phys.*, vol. 9, no. 3, pp. 823–829, 2009.

[124] U. Nitschke, A. A. Ruth, S. Dixneuf, and D. B. Stengel, “Molecular iodine emission rates and photosynthetic performance of different thallus parts of Laminaria digitata (Phaeophyceae) during emersion,” *Planta*, vol. 233, no. 4, pp. 737–748, 2011.

[125] J. Chen, J. C. Wenger, and D. S. Venables, “Near-ultraviolet absorption cross sections of nitrophenols and their potential influence on tropospheric oxidation capacity,” *J. Phys. Chem. A*, vol. 115, no. 44, pp. 12235–12242, 2011.

[126] R. Thalman and R. Volkamer, “Inherent calibration of a blue LED-CE-DOAS instrument to measure iodine oxide, glyoxal, methyl glyoxal, nitrogen dioxide, water vapour and aerosol extinction in open cavity mode,” *Atmos. Meas. Tech.*, vol. 3, no. 6, pp. 1797–1814, 2010.

[127] A. L. Gomez, R. F. Renzi, J. A. Fruetel, and R. P. Bambha, “Integrated fiber optic

incoherent broadband cavity enhanced absorption spectroscopy detector for near-IR absorption measurements of nanoliter samples," *Appl. Opt.*, vol. 51, no. 14, pp. 2532–2540, 2012.

[128] W. Denzer *et al.*, "Near-infrared broad-band cavity enhanced absorption spectroscopy using a superluminescent light emitting diode," *Analyst*, vol. 134, no. 11, pp. 2220–2223, 2009.

[129] J. M. Dudley, G. Genty, and S. Coen, "Supercontinuum generation in photonic crystal fiber," *Rev. Mod. Phys.*, vol. 78, pp. 1135–1184, 2006.

[130] J. M. Langridge, T. Laurila, R. S. Watt, R. L. Jones, C. F. Kaminski, and J. Hult, "Cavity enhanced absorption spectroscopy of multiple trace gas species using a supercontinuum radiation source.," *Opt. Express*, vol. 16, no. 14, pp. 10178–10188, 2008.

[131] R. J. Wild *et al.*, "A measurement of total reactive nitrogen, NOy, together with NO_2, NO, and O_3 via cavity ring-down spectroscopy," *Environ. Sci. Technol.*, vol. 48, no. 16, pp. 9609–9615, 2014.

[132] S. E. Sanders, O. R. Willis, N. H. Nahler, and E. Wrede, "Absolute fluorescence and absorption measurements over a dynamic range of 10^6 with cavity-enhanced laser-induced fluorescence," *J. Chem. Phys.*, vol. 149, no. 1, p. 014201, 2018.

[133] J. M. Langridge, S. M. Ball, A. J. L. Shillings, and R. L. Jones, "A broadband absorption spectrometer using light emitting diodes for ultrasensitive, in situ trace gas detection," *Rev. Sci. Instrum.*, vol. 79, no. 12, p. 123110, 2008.

[134] S. Shardanand and A. D. P. Rao, "Absolute Rayleigh scattering cross sections of gases and freons of stratospheric interest in the visible and ultraviolet regions," *NASA Tech. Note*, 1977.

[135] C. Wang and A. Mbi, "A new acetone detection device using cavity ringdown spectroscopy at 266 nm," *Meas. Sci. Technol*, vol. 18, pp. 2731–2741, 2007.

[136] L. Ciaffoni *et al.*, "Demonstration of a mid-infrared cavity enhanced absorption spectrometer for breath acetone detection," *Anal. Chem.*, vol. 85, no. 2, pp. 846–850, 2013.

[137] C. Deng, J. Zhang, X. Yu, W. Zhang, and X. Zhang, "Determination of acetone in

human breath by gas chromatography-mass spectrometry and solid-phase microextraction with on-fiber derivatization," *J. Chromatogr. B*, vol. 810, pp. 269–275, 2004.

[138] W. Denzer *et al.*, "Trace species detection in the near infrared using Fourier transform broadband cavity enhanced absorption spectroscopy: initial studies on potential breath analytes," *Analyst*, vol. 136, no. 4, pp. 801–806, 2011.

[139] M. Sun *et al.*, "A fully integrated standalone portable cavity ringdown breath acetone analyzer," *Rev. Sci. Instrum.*, vol. 86, no. 9, p. 95003, 2015.

[140] Z. Wang and C. Wang, "Is breath acetone a biomarker of diabetes ? A historical review on breath acetone measurements," *J. Breath Res.*, vol. 7, p. 037109, 2013.

[141] T. Araki and H. Misawa, "Light emitting diode-based nanosecond ultraviolet light source for fluorescence lifetime measurements," *Rev. Sci. Instrum.*, vol. 66, p. 5469, 1995.

[142] T. Araki, Y. Fujisawa, and M. Hashimoto, "An ultraviolet nanosecond light pulse generator using a light emitting diode for test of photodetectors," *Rev. Sci. Instrum.*, vol. 68, p. 1365, 1997.

[143] J. M. Herbelin *et al.*, "Sensitive measurement of photon lifetime and true reflectances in an optical cavity by a phase-shift method," *Appl. Opt.*, vol. 19, no. 1, pp. 144–147, 1980.

[144] R. Engeln, G. Von Helden, G. Berden, and G. Meijer, "Phase shift cavity ring down absorption spectroscopy," *Chem. Phys. Lett.*, vol. 262, no. 1, pp. 105–109, 1996.

[145] A. J. Huisman *et al.*, "Laser-induced phosphorescence for the in situ detection of glyoxal at part per trillion mixing ratios," *Anal. Chem.*, vol. 80, pp. 5884–5891, 2008.

[146] "200 - 800nm, Manual Mini-Chrom Monochromator, Edmund Optics." [Online]. Available: https://www.edmundoptics.eu/p/200---800nm-manual-mini-chrom-monochromator/4232/. [Accessed: 05-Jan-2018].